MINERALOGICAL AND GEOCHEMICAL INVESTIGATION OF LAYERED CHROMITITES FROM THE BRACCO-GABBRO COMPLEX, LIGURIAN OPHIOLITE, ITALY

MASTERS THESIS

University of Leoben

Department of Applied Geosciences and Geophysics

Chair of Resource Mineralogy

Raphael J. Baumgartner, BSc

Supervisor: Ao. Univ. Prof. Dr. Oskar A.R. Thalhammer

Leoben, May 2012

AFFIDAVIT

I declare in lieu of oath, that I wrote this thesis and performed the associated research myself, using only literature cited in this volume.

EIDESSTAATLICHE ERKLÄRUNG

Ich erkläre an Eides statt, dass ich diese Arbeit selbstständig verfasst, andere als die angegebenen Quellen und Hilfsmittel nicht benutzt und mich auch sonst keiner unerlaubten Hilfsmittel bedient habe.

Datum	Unterschrift

ACKNOWLEDGEMENTS

First of all, I would like to thank my supervisor, **Prof. Oskar Thalhammer**, for the great scientific support as well as the guidance throughout my master thesis. Furthermore, I would like to express my sincerest gratitude to **Dr. Federica Zaccarini** and **Prof. Giorgio Garuti** for the initiation of this project, their brilliant scientific support and their encouragement with the technical equipment. It was a great pleasure for me to work with them in the highly interesting field of magmatic petrology. I attribute the level of this master thesis to their remarkably efforts in the last year. Thank you!

Many thanks also go to **Helmut Mühlhans** for sample preparation.

Last but not least, I want to thank my **parents** and my **siblings** for their love and great support throughout this part of my life!

One of the main difficulties in communicating with geologists is their belief that a million years is a short amount of time and their heads are harder than rocks. Consequently, such abstract concepts as "Tuesday Morning" and "Lunchtime" are completely beyond their comprehension!

(http://uncyclopedia.wikia.com/wiki/Geologist)

ABSTRACT

The gabbros of the Bracco-Gabbro Complex (Internal Liguride ophiolite), that intruded subcontinental mantle peridotite, contain layers of chromitite associated to ultramafic differentiates, i.e. melatroctolites. The chromitites and the disseminated chromites in the ultramafics have Al contents similar to Al-rich podiform chromitites [0.40 <Cr# = Cr/(Cr+Al) <0.55]. TiO_2 contents of the chromitites range up to 0.8 wt%, as typical for stratiform chromitites. Geothermobarometrical calculations on few preserved silicate inclusions in chromite indicate that they crystallized at temperatures ranging between 970 and 820 °C, as well as under relatively high oxygen fugacities ($\Delta \log fO_2$ at +2.0-2.4). The calculated Al_2O_3 and TiO_2 content of the parental melt suggests that the melt was of MORB type. Chromitites were altered during the post-magmatic tectonometamorphic uplift and the final exposure at the seafloor, as evidenced by the formation of ferrian chromite. The PGE contents of the chromitites and melatroctolites are unusually low (PGE_{max} 83 ppb). The chondrite-normalized PGE spidergrams show positive PGE patterns and to some extent similarities with the typical trend of stratiform chromitites. No specific PGM have been found but low concentrations of PPGE (Rh, Pt, and Pd) have been detected in the sulphides that occur interstitially to, or enclosed in chromite. Recently, it has been shown that the Internal Liguride gabbroic intrusions have formed by relatively low degrees of partial melting of the asthenospheric mantle. It is concluded that the low degree of partial melting might was the main factor to control the unusual low PGE contents and the rather unique PGE distribution in the Bracco chromitites.

ZUSAMMENFASSUNG

Die exhumierten subkontinentalen Mantelgesteine (Peridotite) der Ligurischen Ophiolit-Serie repräsentieren Relikte des Piedmont-Ligurischen Ozeans (Ligurische Tethys). Der Bracco-Gabbro Komplex, aufgeschlossen zwischen Kilometer 452 und 461 der Via Aurelia, repräsentiert eine Gabbro-Intrusion innerhalb subkontinentaler Mantelgesteine. Ultramafische Differenziate (bspw. Dunit, Melatroktolit) der Gabbro-Intrusion beinhalten lagenförmig angereicherte (stratiforme) Chromititthorizonte. Deren chemische Zusammensetzung ist ähnlich den aluminiumreichen podiformen Chromititen [0.40 <Cr# = Cr/(Cr+Al) <0.55]. Die hohen TiO_2-Gehalte (bis zu 0,8 Gew%) sind typischen für den stratiformen Chromerz-Lagerstättentyp. Die Bildungsbedingungen wurden anhand geothermobarmetrischer Kalkulationen an silikatischen Einschlüssen in Chromit bestimmt. Die Chromite bildeten sich unter einer Temperatur von 970-820°C, sowie unter relativ hohen Sauerstofffugazitäten ($\Delta \log fO_2$ = 2,0-2,4). Die berechneten Al_2O_3 und TiO_2 Gehalte der Mutterschmelze weisen auf eine MORB-Typ Intrusion hin. Die PGE-Gesamtgesteinsgehalte der analysierten Chromitite, Melatroktolite und Dunite sind außergewöhnlich niedrig (PGE_{max} 83 ppb). Die Chondrit-normalisierten PGE-Verteilungsmuster zeigen eine positive Steigung, ähnlich dem Trend stratiformer Chromitite. Die Bracco-Chromitite führen teilweise hohe Gehalte an Sulfidmineralen, die leicht erhöhte Gehalte an PPGE (Rh, Pt, Pd) aufweisen. Die Schmelzen der Bracco Gabbro-Intrusion sind durch niedriggradiges partielles Aufschmelzen des asthenospherischen Mantels entstanden. Die geringen PGE-Gehalte und außergewöhnlichen PGE-Verteilungsmuster der untersuchten Gesteine sind vermutlich auf den niedrigen Aufschmelzungsgrad des asthenospherischen Mantels zurückzuführen.

TABLE OF CONTENTS

1. INTRODUCTION **1**

2. MID OCEAN RIDGES AND OCEANIC LITHOSPHERE **3**

3. OPHIOLITES **5**

4. SPINEL GROUP MINERALS **6**

4.1. Chromite alteration 7

5. CHROMITITES **8**

5.1. Formation of stratiform chromitites 8

6. PLATINUM-GROUP ELEMENTS **10**

6.1. PGE extraction from the mantle 10

6.2. Ore forming processes 10

7. GEOTHERMOBAROMETRY **13**

7.1. Selected geothermobarometers 13

8. LIGURIAN OPHIOLITES **15**

9. GEOLOGICAL OVERVIEW **17**

10. ANALYTICAL TECHNIQUES **19**

10.1. Microscopy 19

10.2. Raman spectroscopy 19

10.3. Electron probe microanalyses 19

10.4. Instrumental neutron activation analysis 21

11. FIELD RELATIONSHIPS **22**

12. PETROGRAPHY AND MINERALOGY **24**

12.1. Chromitites 24

12.2. Melatroctolites 26

12.3. Serpentinized dunites 27

12.4. Silicate and oxide inclusions 28

12.5. Sulphides 29

13. ANALYTICAL RESULTS 30

13.1. Raman spectroscopy 30

13.1.1. Chromite 30

13.1.2. Phyllosilicates 31

13.1.3. Prehnite 32

13.1.4. Silicate inclusions in chromites 33

13.2. Electron probe microanalyses 37

13.2.1. Chromites 37

13.2.2. Sulphides 41

13.2.3. Silicates 42

13.3. Platinum group element geochemistry/mineralogy 44

14. GEOTHERMOBAROMETRICAL CALCULATIONS 47

15. PARENTAL MELT COMPOSITIONS 50

16. DISCUSSION AND CONCLUSIONS 52

16.1. Constraints to the origin of the Bracco chromitites 52

16.2. Significance of the PGE distribution 53

16.3. Nature of the parental magma of the Bracco-Gabbro Complex 54

16.4. Chromite alteration 55

17. REFERENCES 56

18. APPENDIX 64

18.1. Electron probe microanalyses (EPMA) 64

18.1.1. Chromites 64

18.1.2. Sulphides 76

18.1.3. Silicates 83

1. INTRODUCTION

Refractory chromite is one of the early stable phases to crystallize from mafic- to ultramafic melts and is therefore a common accessory mineral in mafic-ultramafic magmatic rocks. Rocks containing more than 45% modal chromite are classified as chromitites. Chromitites are associated with layered igneous intrusions in tectonically stable continental crust as well as with ultramafic-mafic complexes in orogenic belts, for example ophiolites, orogenic lherzolites and concentrically zoned complexes of the Ural-Alaskan type (Thayer 1970; Stowe 1994; Garuti et al. 2012). According to the morphology of the ore body, chromitites are classified into two descriptive types: i) the stratiform chromitites consist of extended layers of massive chromite associated with ultramafic cumulates in the lower part of continental layered intrusions and supra-Moho cumulate sequences of ophiolites, ii) the podiform chromitites consist of lenticular and irregular orebodies (lenses, pods, schlieren) within the mantle section of ophiolites, orogenic lherzolites and the dunite core of Ural-Alaskan complexes. All the chromitites contain sub-economic to economic concentrations of platinum-group elements (PGE) that form discrete minerals, i.e. platinum-group minerals (PGM). The extraction of PGE-rich basaltic melts from the mantle is believed to be largely controlled by its degree of partial melting (e.g. Barnes et al. 1985; MacLean 1969; Keays 1995; among others).

Experiments and the study of natural occurrences have demonstrated that the mineral chemistry of accessory chromite in igneous rocks depends on the parental melt composition and can be used as an indicator of the degree of melting of their mantle source (Irvine 1965 1967; Hill and Roeder 1974; Dick and Bullen 1984; Arai 1992; Roeder 1994; Zhou and Robinson 1994; Kamenetsky et al. 2001; Barnes and Roeder 2001). For example, Maurel and Maurel (1982), Maurel (1984; cited in Augé 1987) and Rollinson (2008) developed calculation methods to determine the FeO/MgO ratio and Al_2O_3 as well as TiO_2 contents of parental melts, based on the chemical composition of chromite. Moreover, compositional relations between chromite and coexisting mafic silicates (olivine, orthopyroxene) have been used to formulate geothermobarometrical methods to evaluate precipitation conditions (p, T, $\Delta \log f0_2$) of chromites in ultramafic sequences (e.g. Fabries 1979; O'Neill and Wall 1987; Ballhaus et al. 1991; Jianping et al. 1995; Liermann and Ganguly 2003, 2007). Finally, the distribution and mineralogy of PGE vary significantly according to the type of chromitite, providing invaluable information on the fertility of the mantle source from which the chromitite parental melt was extracted (e.g. Barnes et al. 1985; MacLean 1969; Keays 1995; among others). In mafic- to ultramafic complexes undergoing hydrothermal alteration and weathering, chromitites may represent the only ultramafic rocks having preserved, at least in part, their original magmatic features. This is because of the higher chemical resistance of chromite compared with the associated silicates and the relative immobility of the PGE under low temperature alteration.

The first potentially economic chromite deposit in Italy was discovered in the Bracco-Gabbro Complex (Ligurian ophiolites), close to the village of Ziona (Stella 1924). The deposit was almost completely

worked out and only a small dump is presently accessible (Brigo and Ferrario 1974). Successive exploration of the complex led to the discovery of several chromitite occurrences. They have been proven to be subeconomic. The Bracco chromitites are unusual compared with chromitites in ophiolite complexes of the Eastern Mediterranean Tethys, which formed in mature oceanic settings (Leblanc and Nicolas 1992). In contrast, the Bracco chromitites were emplaced in an extensional regime, during the pre-oceanic stage of the Ligurian Tethys (Lemoine et al. 1987; Piccardo et al. 2002; Piccardo and Guarneri 2011). Formation of chromitite at spreading centres before ocean opening is uncommon (Roberts 1988; Zhou et al. 1994; Arai 1997). Therefore, knowledge of the compositional and mineralogical characteristics of the Bracco chromitites may be relevant to improve our understanding of chromitite formation in unconventional geological settings, such as that of the Ligurian ophiolites.

This study represents a detailed mineralogical and geochemical investigation of chromitites from the same occurrences described by Bezzi and Piccardo (1970): Ziona, Mattarana, Canegreca, Cima Stronzi and Pian della Madonna. The data presented in this work include: i) composition of fresh and altered chromite, ii) mineralogy and composition of associated accessory minerals (sulphides and silicates), and iii) complete set of PGE analyses on chromitites and host rocks. On the basis of the data acquired, the possible composition of the melt in equilibrium with crystallizing chromite has been determined. Furthermore, the conditions under which the Bracco chromitites might have formed were evaluated.

2. MID-OCEAN RIDGE AND OCEANIC LITHOSPHERE

A mid ocean ridge is a boundary between two or more tectonic plates at which new oceanic lithosphere forms from gabbroic magma. The production of the magma is linked to the partial melting of asthenospheric mantle lherzolite, due to adiabatic upwelling and decompression of the mantle. The evolved gabbroic magma crystallizes in a magma chamber at the spreading centre, but also provides subsurface (sheeted dykes) as well as surface volcanism (pillow lavas, sheet lava flows). The structural composition of the oceanic lithosphere is strongly controlled by the spreading velocity of the ridges. Spreading rates may vary from a few mm/yr up to more than 100 mm/yr. Fast spreading ridges are controlled by a high magma production rate. Thereby, the magma supplies a permanent magma chamber below the ridge, leading to the formation of a continuous gabbroic layer (Fig. 1a), that forms in the crustal section. Slow-spreading ridges (≤40 mm/yr) have no stable magma chamber due to minor magma supply. Upwelling magma accumulates in small magma pockets (Fig. 1b) within the mantle section (Wilson 1989).

The layered structure of the oceanic crust can be described from top to bottom as follows (Wilson 1989):

- **Oceanic crust**
    - Marine sedimentary cover (radiolarian cherts, ophicalcites, etc.)
    - Basaltic pillow lavas and sheet lava flows
    - Subvolcanic (doleritic) sheeted dykes
    - Isotropic gabbros
    - Layered gabbros
- **Seismic mantle-crust boundary (seismic MOHO)**
    - Layered cumulate peridotites (early differentiation products due to fractional crystallization and gravitational settling at the floor of the magma chamber)
- **Petrological mantle-crust boundary (petrological MOHO)**
- **Mantle**
    - Depleted harzburgites or dunites close to the mantle-crust boundary
    - Less depleted lherzolites in the zone of partial melting

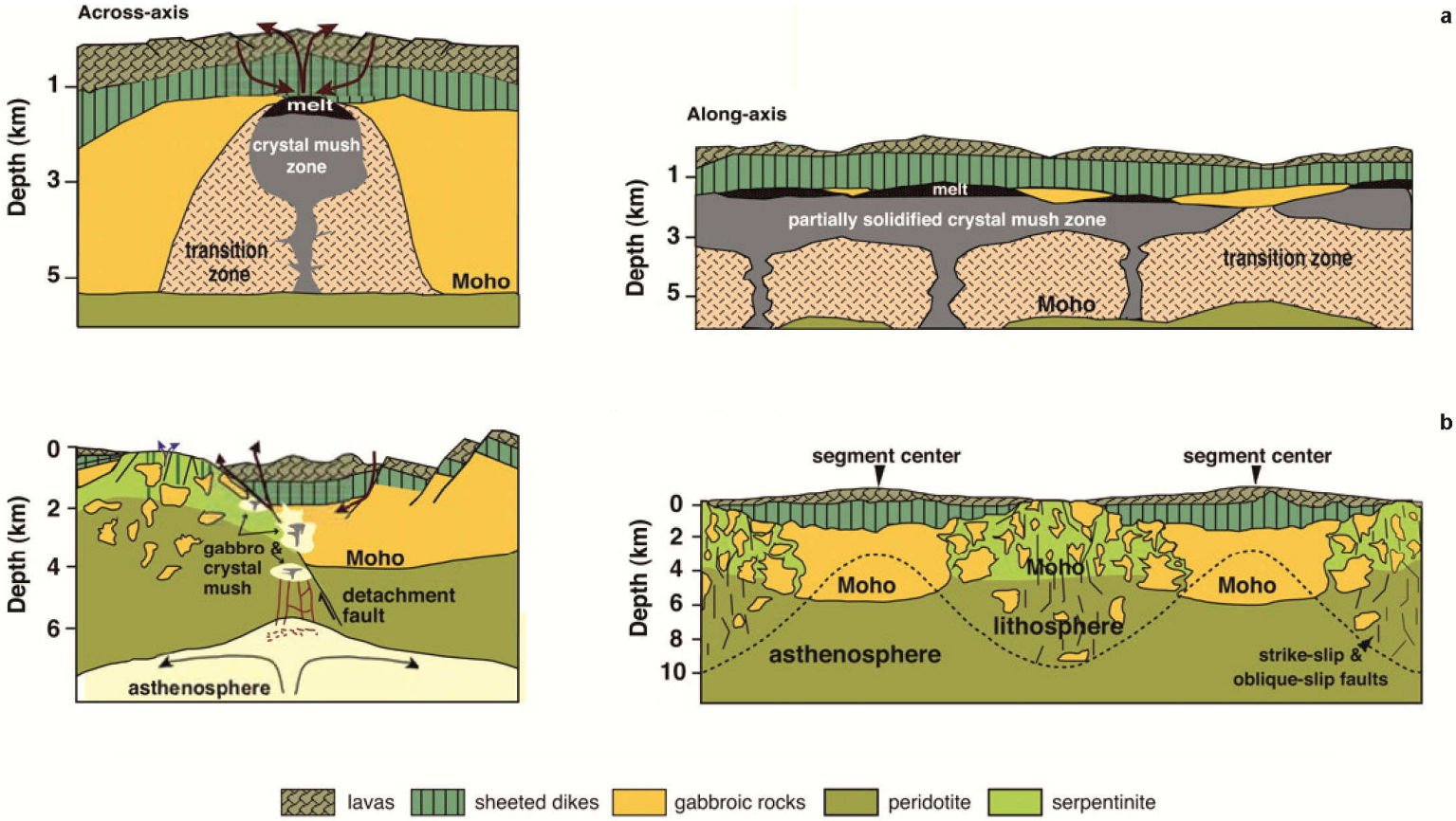

Fig. 1 a,b Cross section through a fast spreading (a) and a slow spreading (b) mid ocean ridge (Bach and Früh-Green 2010).

3. OPHIOLITES

Ophiolites are allochthonous fragments of ancient oceanic lithosphere and asthenospheric mantle that were tectonically emplaced and affiliated (i.e. obducted) to continental margins due to plate convergences (e.g. continent-continent collision, arc-continent collision, ridge trench interaction and/or subduction-accretion event). Ophiolites are therefore commonly related to accretionary- or collision-type orogenic belts between amalgamated plates or accreted terrenes (Dilek and Furnes 2011, and references therein). The geodynamic setting at which ophiolites formed is still controversial. Until the early 80s it has been thought that ophiolites generally form at the initial stage of the Wilson cycle (seafloor spreading) or at supra subduction zones (SSZ) close to convergent plates. However, based on the structural architecture, geochemical fingerprints and evolutionary paths it has been recognized, that further tectonic environments, even within the same orogenic belt, have to be considered. Tectonic environments may include relics of intracontinental rift basins, embryonic normal oceanic crust with MORB affinity (Ligurian ophiolites) or protoarc-forearc-backarc assemblages with SSZ affinity (Mediterranean ophiolites). Furthermore, ophiolites may also represent tectonically emplaced fragments of oceanic crust with an affinity to large igneous provinces (LIP), such as the Caribbean ophiolites, or show a more complex igneous history which may involves the evolution of ensimatic arc terrenes with multiple episodes of magmatism, rifting or tectonic accretion (Pacific rim ophiolites). Ophiolites that are arranged to accretionary complexes of ancient active margins are commonly associated with mélanges and high-pressure metamorphic rocks. They may represent relics of abyssal peridotites, ocean island basalts (OIB), seamounts, island arcs or crust at mid ocean ridges, abraded from a subducting plate (Dilek 2003, and references therein).

4. SPINEL-GROUP MINERALS

Chromite is a member of the spinel group minerals and has a general formula of $A^{2+}B^{3+}{}_2O_4$. The unit cell is characterized by a structure of cubic close-packed oxygen atoms and consists of 32 oxygen atoms and 24 cations. The structure of spinel has a total of 96 interstitial gaps, 64 with tetrahedral and 32 with octahedral coordination. Only eight of the tetrahedral and 16 of the octahedral positions are filled with cations. Spinels with "normal" spinel structure have tetrahedral positions usually occupied by divalent cations (e.g. Mg, Fe^{2+}, Zn, Mn, Ni, Co, Cu, etc.), whereas octahedral positions usually contain trivalent cations (e.g. Al, Fe^{3+}, Cr, V, etc.). However, spinels with "inverse" spinel structure have trivalent cations at the tetrahedral sites and divalent, as well as trivalent cations at the octahedral sites (Bowles et al. 2011). Fig. 2 shows the main (end-) members of the spinel-group minerals in a simple diagram.

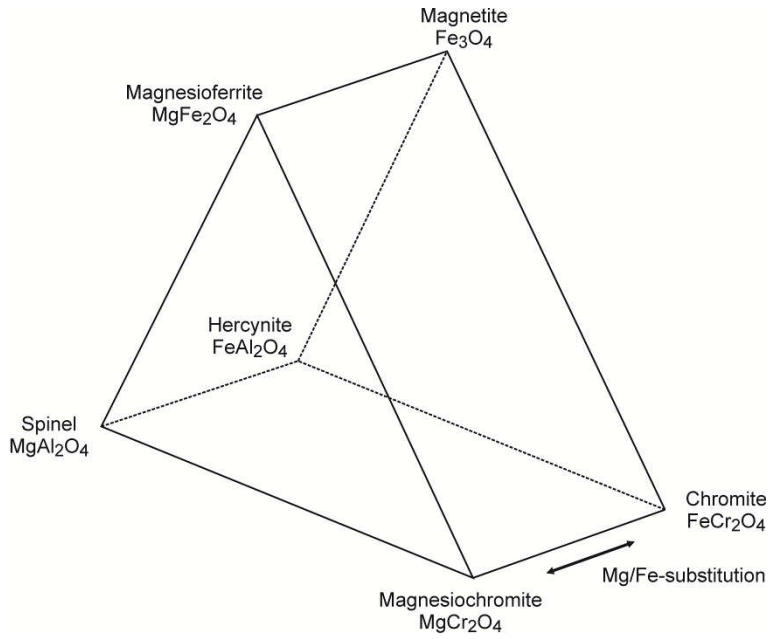

Fig. 2 Classification scheme for the main (end-) members of the spinel group minerals, based on the substitution of Fe^{3+}-Cr-Al at the octahedral sites and Mg-Fe^{2+} at the tetrahedral sites (redrawn after Bowles et al. 2011).

The ideal chromite composition is those of a magnesiochromite ($MgCr_2O_4$). Natural samples show a broad substitution of Fe^{2+} for Mg at the tetrahedral sites, as well as Fe^{3+} and Al for Cr at the octahedral sites. The tetrahedral sites may also contain minor amounts of Mn and Zn, whereas octahedral sites may be occupied by V, Ni or Co (Bowles et al. 2011). Chromite is a common mineral in ultramafic and mafic rocks and occurs as disseminated single grains or chromitites (> 45 % modal chromite).

4.1. Chromite alteration

Horninger (1941) and Spangeberg (1942) were one of the first authors to recognize typical alteration characteristics of chromite. Altered chromites have highly reflective Fe-rich borders, called “grey magnetite”, “ferritchromite” or “ferrian chromite”. Progressively altered chromites are partially or totally transformed into ferrian chromite. Partially altered crystals usually show a fresh core that is rimmed by ferrian chromite. It has been assumed that several stages of low-grade (e.g. hydrothermal serpentinization) and medium to high grade metamorphism (greenschist to amphibolite facies conditions) cause chromite alteration. According to Barnes (2000), unaltered chromites are termed as “Type 1 chromite”. Original chromite faces are visible and no secondary minerals have been formed at the expense of chromite. They may have a coating of magnetite that is derived from the serpentinization of the host rock. “Type 2 chromite” has a ferrian chromite rim that forms continuously by replacing the chromite. The hydrothermal alteration of chromite is characterized by a significant release of Ti, Al and Mg, whereas Fe and sometimes Cr increase (e.g. Beeson and Jackson 1969; Barnes 2000), as illustrated in Fig. 3. Chromites, affected by greenschist facies temperatures, have Mg# between 0.4 and 0.7. In contrast, chromites modified by amphibolite facies temperatures have Mg# always lower than 0.35 Barnes (2000).

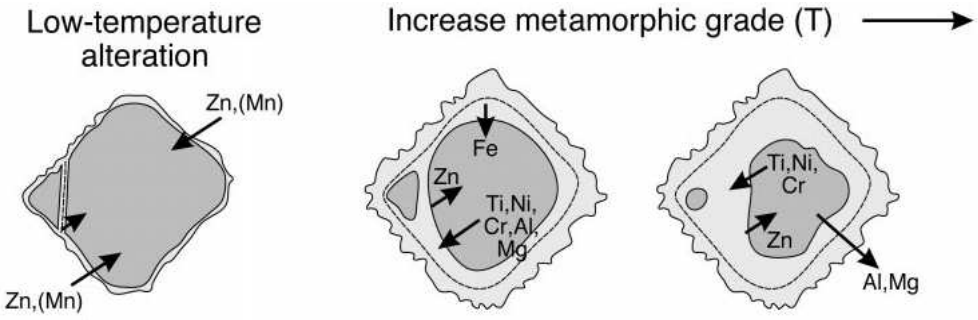

Fig. 3 Alteration characteristics and chemical change in chromites and their magnetite/ferrian chromite rims at low temperature alteration and at elevated metamorphic grades (Barnes 2000).

5. CHROMITITES

Rocks containing more than 45% modal chromite are classified as chromitites. Chromitites are associated with layered igneous intrusions in tectonically stable continental crust as well as with ultramafic-mafic complexes in orogenic belts, for example ophiolites, orogenic lherzolites and concentrically zoned complexes of the Ural-Alaskan type (Thayer 1970; Stowe 1994; Garuti et al. 2012). According to the morphology of the ore body, chromitites are classified into two descriptive types: i) the stratiform chromitites consist of extended layers of massive chromite associated with ultramafic cumulates in the lower part of continental layered intrusions and supra-Moho cumulate sequences of ophiolites, ii) the podiform chromitites consist of lenticular and irregular orebodies (lenses, pods, schlieren) within the mantle section of ophiolites, orogenic lherzolites and the dunite core of Ural-Alaskan complexes.

5.1. Formation of stratiform chromitites

Stratiform chromitites have a cyclic nature with laterally contiguous seams throughout the entire intrusion. The thickness of the chromitite layers may range from several millimetres up to a few meters. A number of possible formation models to explain the crystallization of stratiform chromite have been proposed until now, but mechanisms are still controversial. It has been assumed that chromite seams are the product of fractional crystallization in a magma chamber with a melt composition close to the orthopyroxene-chromite liquidus, but the change of pressure or oxygen fugacity, country rock assimilation, magma mixing at the roof of the magma chamber, or downward infiltration of a picritic melt may be also a trigger of chromite precipitation (Bowles et al. 2011). Irvine (1977) suggested that chromitite precipitation is linked to the contamination of evolved primary melts by a more primitive one, i.e. magma mixing (Fig. 4).

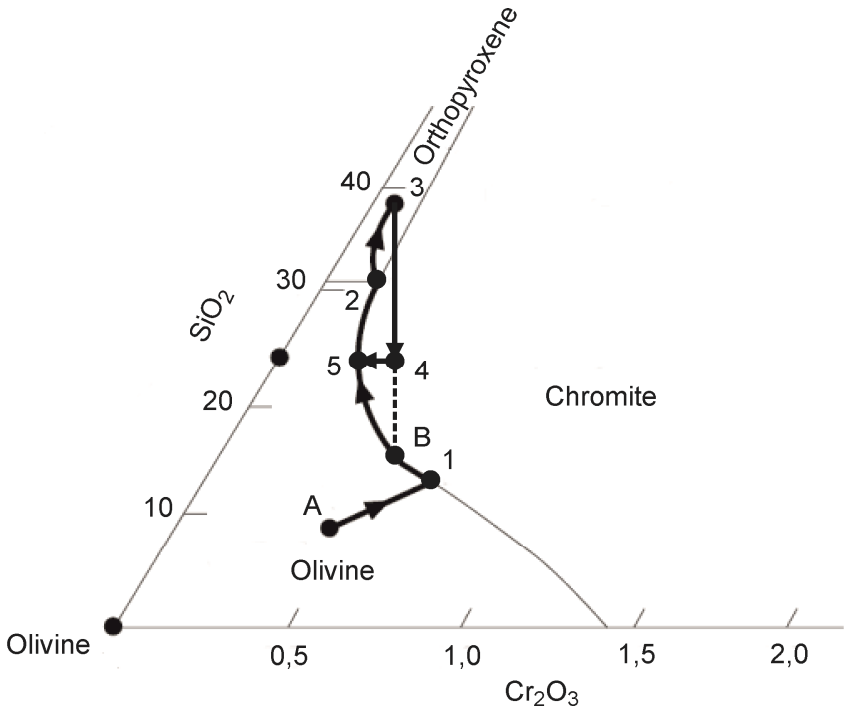

Fig. 4 Formation of stratiform chromitites based on the magma mixing model (redrawn after Robb 2005, and references therein). A melt with the initial composition in the olivine field (A) produces olivine to form a dunite until the melt reaches the cotectic phase boundary olivine-chromite (1). Consequently, olivine and minor amounts of chromite (~1%) precipitate from the melt. The melt evolves along the cotectic line until it reaches the triple point olivine-orthopyroxene-chromite (2). Orthopyroxene starts to crystallize until the magma reaches the final point (3). At this stage, a pulse of more primitive magma than the evolved magma (B) is necessary to shift the bulk composition to a point in the chromite field (4) to initiate crystallization of abundant chromite. This process continues until the bulk composition of the melt reaches the cotectic olivine-chromite phase boundary (5) again.

6. PLATINUM-GROUP ELEMENTS

The term platinum-group elements (PGE) summarizes a group of siderophile to chalcophile elements (Os, Ir, Ru, Rh, Pt, Pd) with high melting points (up to 1770°C), high densities, good resistance to chemical attack, high catalytic activity, mechanical strength and malleability. Concentrations in the earths crust vary from sub-ppm level in intermediate or felsic rocks to 1-100 ppm in mafic or ultramafic rocks (e.g. Misra 1999). Because of their distribution and partitioning behaviour, the PGE can be subdivided into two groups. Ru, Os, and Ir (IPGE = iridium subgroup) are usually concentrated in melts early crystalline phases due to their compatible nature. In contrast, Pt, Pd and to some extent Rh (PPGE = palladium subgroup) are progressively enriched in differentiated melts (e.g. sulphide melts), because of their incompatible as well as chalcophile nature.

6.1. PGE extraction from the mantle

At partial melting of the asthenospheric mantle, sulphides tend to melt earlier than silicates due to their lower melting points. At low degrees of partial melting, most sulphides are dissolved, but only few silicates will be melted and move into the generated small melt portion at the time. During continuous crystal fractionation, the evolved melt reaches early sulphur saturation and separates into a silicate and a sulphide melt. In this case, the PGE preferentially concentrate in the sulphide melt that remains in the mantle, whereas basaltic melts, poor in PGE, rise up (Pohl 2011). It has been recognized that relatively high degrees of partial melting (20-30%) are necessary that evolved melts remain sulphur undersaturated for a long period of time, and may reach sulphur saturation at a very late stage of magma evolution (e.g. MacLean 1969; Barnes et al. 1985; Keays 1995; among others).

6.2. Ore forming processes

Podiform and stratiform chromitites are usually enriched in PGE compared to their host rocks. In particular, the podiform chromitite, with few exceptions, are enriched in IPGE. Therefore, their chondrite normalized PGE spidergrams show a negative slope (e.g. Economou Eliopoulos 1996; Melcher et al. 1999; Ahmed and Arai 2002). However, few examples of podiform chromitites hosted in the ophiolitic mantle (e.g. Çina et al. 2002; Escayola et al. 2011) and a number of stratiform chromitites, including the Upper Group of the Bushveld Complex (e.g. Von Gruenewaldt and Merkle 1995), display PGE positive patterns due to the predominance of PPGE over IPGE. Consistently with these two different PGE patterns, the dominant PGM in the podiform chromitite are IPGE phases. In the chromitites, characterized by the positive PGE patterns, two different groups of PGM have been described. The first group consists of IPGE minerals that mostly occur included in chromite. The second group is composed of PPGE minerals that generally are related to the presence of abundant sulphides, indicating the importance of sulphur as a collector for PPGE (Peck and Keays 1990).

During fractional crystallization in a magma chamber, the sulphur concentration in the residual melt increases. As the melt reaches sulphur saturation, a sulphide liquid separates from the silicate melt. Chalcophile elements (e.g. Ni, Cu, part of PGE) preferentially concentrate in the segregated sulphide liquid. Mavrogenes and O'Neill (1999) have demonstrated that the sulphur solubility in basaltic melts increases as the pressure decreases and that at least 60% of fractional crystallization is necessary to reach sulphur saturation. Therefore, it has been considered that the fractional crystallization in intrusion related shallow magma chambers may not be the sole trigger for the formation of economic sulphide (PGE) deposits. The solubility of sulphur in a silicate melt may be also controlled by the temperature and oxygen or sulphur fugacity (Holwell 2010 and references therein). Furthermore, it has been proposed that the assimilation of oxygen- or sulphur-bearing, as well as felsic country rocks may be necessary to achieve sulphur saturation (e.g. Buchanan and Nolan 1979; Li and Naldrett 1993). The introduction of a new, primitive magma pulse into a highly evolved resident magma and mixing of these two liquids is a further explanation to drive sulphur saturation and has also been considered as one of the reason for the formation of PGE-rich massive sulphide horizons (i.e. reef type mineralizations) in layered intrusions (e.g. Naldrett 1989; Maier 2005). This mechanism seems to be the most compatible one to explain the presence of abundant PGE-rich sulphides associated with layered chromitites (see chapter 5.1; magma mixing model), as reported by several authors (e.g. Ferreira Filho et al. 1995; Naldrett et al. 2009).

The crystallization of natural sulphur-rich melts can be best described in the system Fe-Ni-Cu-S. At temperatures in the range of 1200 °C, the sulphide melt still contains dissolved base (e.g. Fe, Ni, Cu, Co) and trace metals (e.g. PGE, Au, Bi, Te). As the melt cools down to a temperature of about 1000 °C, a monosulphide solid solution (mss) precipitates from the melt. Elements like Ni and the IPGE preferentially concentrate in the mss. In contrast, elements like Pt and Pd remain in the residual Cu-rich sulphide liquid. As the temperature drops down to about 900°C, an intermediate solid solution (iss) precipitates, but Pt, Pd and even Au remain in an immiscible semimetal rich melt due to their incompatible nature. The residual semimetal rich melt remains liquid until iss crystallizes. At temperatures between 200 and 650 °C, the mss finally recrystallizes to pentlandite and pyrrhotite, whereas IPGE enter the structure of both minerals. However, Rh and Pd are only compatible in pentlandite. Semimetal rich melts finally crystallize to discrete PGM (Fig. 5; Holwell 2010, and references therein).

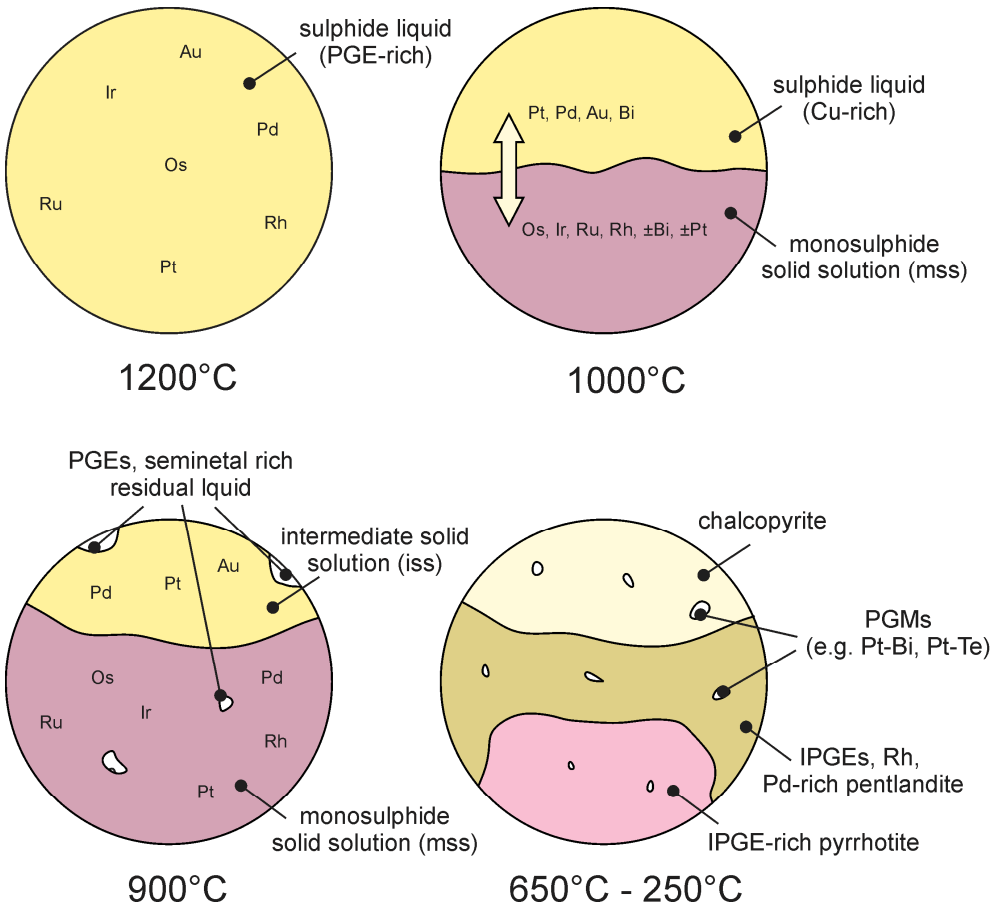

Fig. 5 Schematic illustration showing the fractionation of a PGE-rich sulphide droplet during cooling (redrawn after Holwell 2010).

7. GEOTHERMOBAROMETRY

The geothermobarometry is a fundamental technique to determine conditions at which magmatic or metamorphic processes take place. Geothermobarometrical methods are usually based on the p-T dependency of eqilibrium constants (K_D) and equilibrium curves of mineral reactions. According to the equation of the "Gibbs free energy" in (1), reactions that have a strong temperature dependency (high ΔS) are used as geothermometers, whereas those with a strong pressure dependency (high ΔV) are usually used as geobarometers (Bucher and Grapes 2011).

$$\Delta G_{p,T} = \Delta H_{p,T} - T \cdot \Delta S_{p,T} + R \cdot T \cdot \ln(K) = 0 \quad (1)$$

Exchange reactions (e.g.; Gt-Cpx, Gt-Bt) are characterized by the interchange of atoms, having equal charge numbers or similar cation radii (cation pairs), between the lattice sites of one or between two different minerals. Exchange reactions are used as geothermometers because of low volume changes (ΔV) and relatively high entropy changes (ΔS). The cation pair Mg/Fe^{2+} is the most important one, but their application to chromite-olivine assemblages is problematical because subsolidus re-equilibration effects down to a temperature of about 500 °C influence their distribution coefficient (K_D). Untruly low temperatures have to be expected (Lehmann 1983). The solubility of minerals with a similar structure (e.g. Cpx-Opx, Kfsp-Pl, Ca-Do) usually increases with the temperature. There is a distinct miscibility gap between these minerals at specific temperatures, providing their importance in geothermometry. Net transfer reactions (e.g. Gt-Als-Qtz-An, Cpx-Qtz-Ab) are characterized by distinct volume changes (ΔV) and are therefore used as geobarometers (Bucher and Grapes 2011).

7.1. Selected geothermobarometers

Olivine-spinel-thermometry

The thermometer proposed by Jianping et al. (1995) in (2) is an adaptation of the thermometer proposed by Fabries (1979), which is based on experiments that were performed at temperatures between 880 and 1280 °C as well as pressures between 0,06 and 0,2 GPa. The thermometer proposed by Ballhaus et al. (1991) in (3) is a revised version of the thermometer proposed by O'Neill and Wall (1987) in (4), which is calibrated on experiments that were performed at temperatures between 1040 and 1300 °C as well as pressures between 0.3 and 2.7 GPa.

(2) $$T\,(K) = \frac{4299 \cdot X_{Cr}^{Sp} + 1283}{K_D + 1{,}469 \cdot X_{Cr}^{Sp} + 0{,}363}$$

$$X_{Cr}^{Sp} = \frac{Cr}{Cr + Al + Fe^{3+}} \qquad K_D = \frac{(Fe^{2+}/Mg)_{Sp}}{(Fe^{2+}/Mg)_{Ol}}$$

(3)

$$T\,(K) = \frac{6530 + 28 \cdot p + (7000 \cdot 10{,}8 \cdot p\,) \cdot (1 - 2 \cdot (1 - X_{Mg}^{Ol})) - 1960 \cdot (Mg^{Sp} - Fe^{2+,\,Sp}) - 16150 \cdot \frac{Cr^{Sp}}{2} + 25150 \cdot (\frac{Fe^{3+,\,Sp}}{2} + Ti^{Sp})}{R \cdot \ln K_D + 4{,}705}$$

$$X_{Mg}^{Ol} = \frac{Mg}{Mg + Fe^{2+}} \qquad K_D = \frac{(Fe^{2+}/Mg)_{Sp}}{(Fe^{2+}/Mg)_{Ol}}$$

(4)

$$T\,(K) = \frac{6530 + 28 \cdot p + (5000 \cdot 10{,}8 \cdot p\,) \cdot (1 - 2 \cdot (1 - X_{Mg}^{Ol})) - 1960 \cdot (Mg^{Sp} - Fe^{2+,\,Sp}) - 16150 \cdot \frac{Cr^{Sp}}{2} + 18620 \cdot (\frac{Fe^{3+,\,Sp}}{2} + Ti^{Sp})}{R \cdot \ln K_D + 4{,}705}$$

$$X_{Mg}^{Ol} = \frac{Mg}{Mg + Fe^{2+}} \qquad K_D = \frac{(Fe^{2+}/Mg)_{Sp}}{(Fe^{2+}/Mg)_{Ol}}$$

Orthopyroxene-spinel-thermometry

The orthopyroxene-spinel thermometer, proposed by Liermann and Ganguly (2003 2007) in (5), was calibrated on experiments performed at temperatures between 850 and 1250 °C as well as pressures between 0.9 and 1.4 GPa. The thermometer is based on the thermodynamic properties of Fe^{3+} and Ti^{4+} bearing spinels, determined by O'Neill and Wall (1987).

(5) $$T\,(K) = \frac{1174 + 76{,}76 \cdot p - 1863 \cdot X_{Al}^{Opx} + 2309 \cdot X_{Cr}^{Sp}}{\ln(K_D) + 0{,}296}$$

$$X_{Al}^{Opx} = \frac{Al_2O_3}{Al_2O_3 + MgSiO_3 + FeSiO_3} \qquad X_{Cr}^{Sp} = \frac{Cr}{Cr + Al + Fe^{3+}} \qquad K_D = \frac{(Fe^{2+}/Mg)_{Sp}}{(Fe^{2+}/Mg)_{Ol}}$$

8. LIGURIAN OPHIOLITES

The Ligurian ophiolites and several other ophiolites in the Central and Western Alps, the Northern Apennines and Corsica represent fragments of the oceanic crust that floored the Ligurian Tethys (Fig. 6). The Ligurian Tethys opened at Jurassic times because of the passive extension of the European continental lithosphere, which was in turn kinematically related to the opening of the Central Atlantic Ocean (Dewey et al. 1973; Lemoine et al. 1987). Decandia and Elter (1972) proposed that the opening of the Ligurian Tethys was driven by symmetric extension, whereas others concluded that the Ligurian Tethys opened due to asymmetric extension, as evidenced by the presence of subcontinental peridotites and relictic stretched continental mantle (Lemoine et al. 1987). However, the Ligurian Tethys is recognized as a magma-poor slow spreading oceanic system (Lagabrielle and Lemoine 1997; Piccardo et al. 2002; Piccardo 2007; Piccardo 2008). Palaeographic reconstructions revealed that the ocean basin had a maximum width of 400-500 km (Stampfli 1993). Ophiolites have been ascribed to different paleogeographic positions in the ocean basin (Piccardo and Guarnieri 2010). Some of the ophiolites have been considered to pertain to marginal or pericontinental settings along the margin of the Adriatic Plate (e.g. Northern Lanzo massif, External Ligurides, part of Erro Tobbio massif), whereas others were suggested to have formed at distal settings (e.g. Southern Lanzo massif, Internal Ligurides, part of Erro Tobbio massif, Monte Maggiore). Fig. 7 shows a palaeographic reconstruction at the Late Jurassic.

The Ligurian ophiolites have an anomalous stratigraphy compared with ideal reconstructions of the oceanic crust, since they lack a true sheeted dyke complex or a well developed cumulus transition zone. Instead, several hundred metres wide layered bodies, predominantly composed of gabbro-norite or gabbro, intruded a lherzolitic mantle characterized by a clear sub-continental petrologic signature. Pillow lavas or pelagic sediments may lie directly on the peridotite-gabbro basement. Most sections include thick horizons of ophiolitic breccia derived from seafloor erosion of plutonic and volcanic rocks (Barret and Spooner 1977; Cortesogno et al. 1987; Lemoine et al. 1987; Piccardo et al. 2002, and references). These characteristics distinguish the Ligurian ophiolites from those in the eastern Mediterranean Tethys, which mainly formed in subduction-influenced geodynamic settings (Robertson 2002).

The mantle peridotites show widespread mineralogical and geochemical modifications due to the interaction with depleted, MORB-type asthenospheric melts that percolated through the mantle by porous flow (Piccardo and Guarnieri 2010). At some stage, diffuse porous flow percolation evolved into an intrusive, channel-driven percolation mechanism giving rise to the formation of ephemeral magma chambers within the upper lithospheric mantle. The asthenospheric mantle melting happened between Early and Late Jurassic times with ages of 179±9 to 164±14 Ma (Rampone et al. 1998; Tribuzio et al. 2004). The peridotite-gabbro association of the Internal Ligurides underwent a polyphase tectono-metamorphic evolution from near-solidus plastic flow to low-temperature serpentinization, rodingitization and brittle fracturing during the progressive uplift from subcontinental levels to exposure at the seafloor, in Late-Jurassic (Cortesogno et al. 1975 1987).

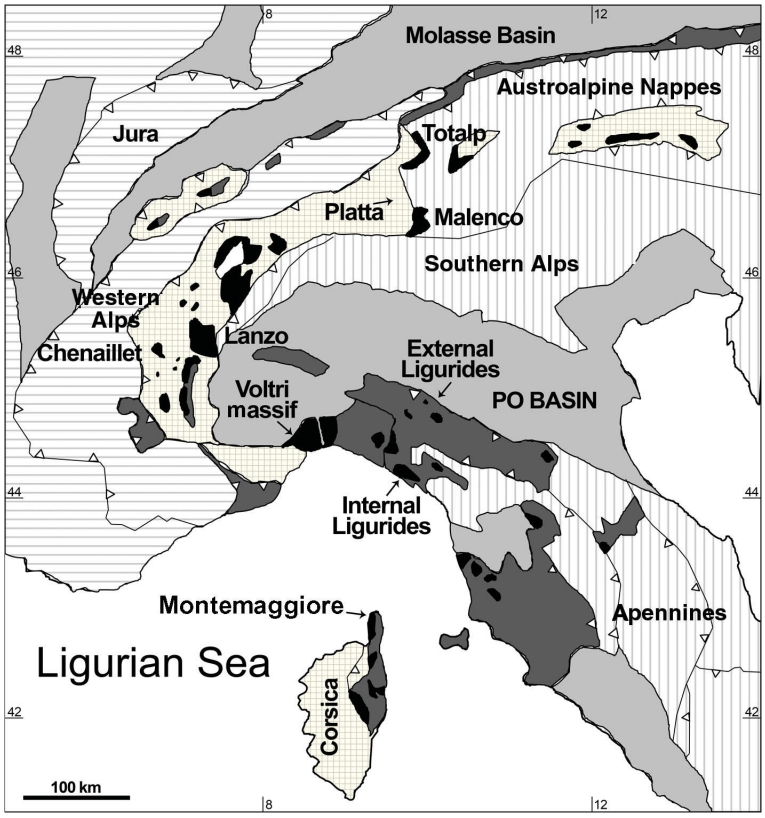

Fig. 6 Major ophiolites in the Central (Totalp, Malenco, Platta) and Western Alps (Lanzo massif, Chenaillet), Ligurian Alps (Voltri massif), Northern Apennines (External Ligurides, Internal Ligurides) and Alpine Corsica (Montemaggiore; Piccardo and Guarnieri 2010).

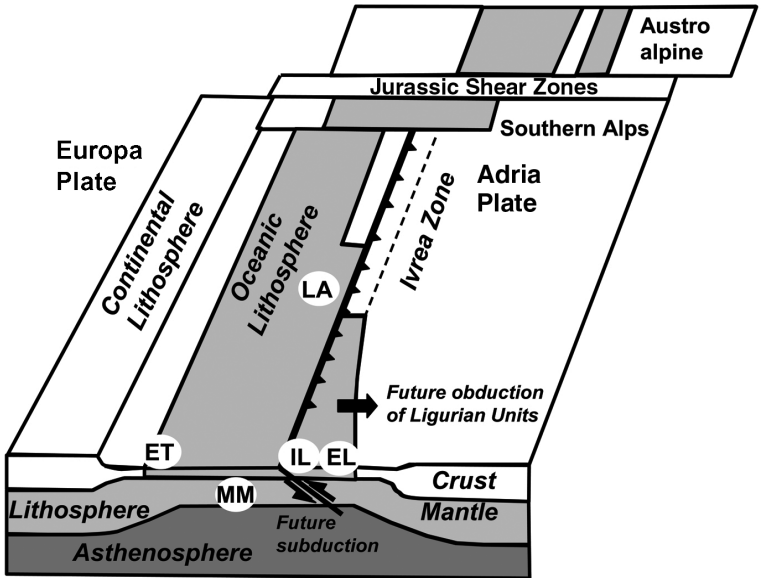

Fig. 7 Palaeographic reconstruction of the Ligurian Tethys (Piccardo and Guarnieri 2010): Abbreviations: LA = Northern Lanzo massif, EL = External Ligurides, ET = Erro–Tobbio massif, IL = Internal Ligurides, MM = Monte Maggiore.

9. GEOLOGICAL OVERVIEW

The Bracco-Gabbro Complex is located about 25 km north-westwards the city of La Spezia (Fig. 8a), between km 452 and km 461 of the ancient Roman Consular Road Aurelia, with a total exposure of about 5 x 6 km. The complex pertains to the Internal Ligurides of the Northern Apennine ophiolites and appears as a layered body intruded into partially to totally serpentinized mantle lherzolite with associated minor harzburgite and dunite. Ophiolitic breccias, pillow lavas and pelagic sediments overly the peridotites and gabbros. All rocks have been partly to completely transformed into low-temperature metamorphic assemblages dominated by serpentine, chlorite, prehnite, ferrian chromite and magnetite (Cortesogno et al. 1981 1987).

Gabbroic rocks predominate in the western and northern parts of the complex, consisting of coarse-grained clinopyroxene gabbro (pl = 60-75 vol%), olivine gabbro with or without clinopyroxene (pl > 60 vol%, ol > 25 vol%, cpx <15 vol%), troctolite (pl = 30-40 vol%, ol > 25 vol%, cpx <5 vol%), as well as subordinate anorthosite (pl > 80 vol%) with disseminated olivine and minor clinopyroxene (< 10 vol%). The clinopyroxene gabbros appear in isotropic masses or in thick layers up to more than 1 m in thickness. The olivine gabbros and troctolites are medium to fine grained and show a conspicuous layering. The layering is frequently disturbed by slump folding and cross bedding, or may be truncated against masses of the coarse grained gabbro. These structures may reflect differential movements of a partially consolidated crystal mush or magmatic turbulence in a tectonically dynamic environment (Cortesogno et al. 1987). Layers, lenses and less regular bodies of ultramafic rocks (melatroctolite, wehrlite, dunite, chromitite) occur in the gabbroic mass. They are mainly concentrated along the S-E margin of the complex (Fig. 8b), possibly corresponding to the base of the magma chamber (Cortesogno et al. 1987). All rocks display an irregular tectonically disrupted layering, broadly oriented SW-NE, and defined by modal and grain-size graded bedding (Bezzi and Piccardo 1970 1971; Cortesogno et al. 1987). Cyclic units of gabbro-anorthosite and troctolite-gabbro-anorthosite occur in gabbroic rocks, whereas dunite-wehrlite-troctolite, dunite-melatroctolite-troctolite and chromitite-melatroctolite-troctolite-anorthosite sequences characterize the internal layering of ultramafic lenses. The ultramafics are defined by modal variation in olivine (65-90 vol%), clinopyroxene (0-10 vol%), frequently poikilitic with rounded olivine inclusions, plagioclase (5-30 vol%) and minor chromitite. The gabbroic and ultramafic rocks of the Bracco complex have been interpreted as the result of fractional crystallization and cumulus of a high-Mg basaltic melt, in which olivine and chrome spinel were primary liquidus phases, along with plagioclase varying from an intercumulus phase in troctolite to a cumulus phase in anorthosite (Bezzi and Piccardo 1970; Cortesogno et al 1987). The layering is frequently disturbed by slumping, cross bedding and plastic flow folding or may be truncated against irregular masses of coarse grained gabbro. These textures have been reported from a number of layered intrusions all over the world and possibly reflect differential movements of a partially consolidated crystal mush or magmatic turbulence in a tectonically dynamic environment (see references in Bezzi and Piccardo 1970 and Cortesogno et al. 1987).

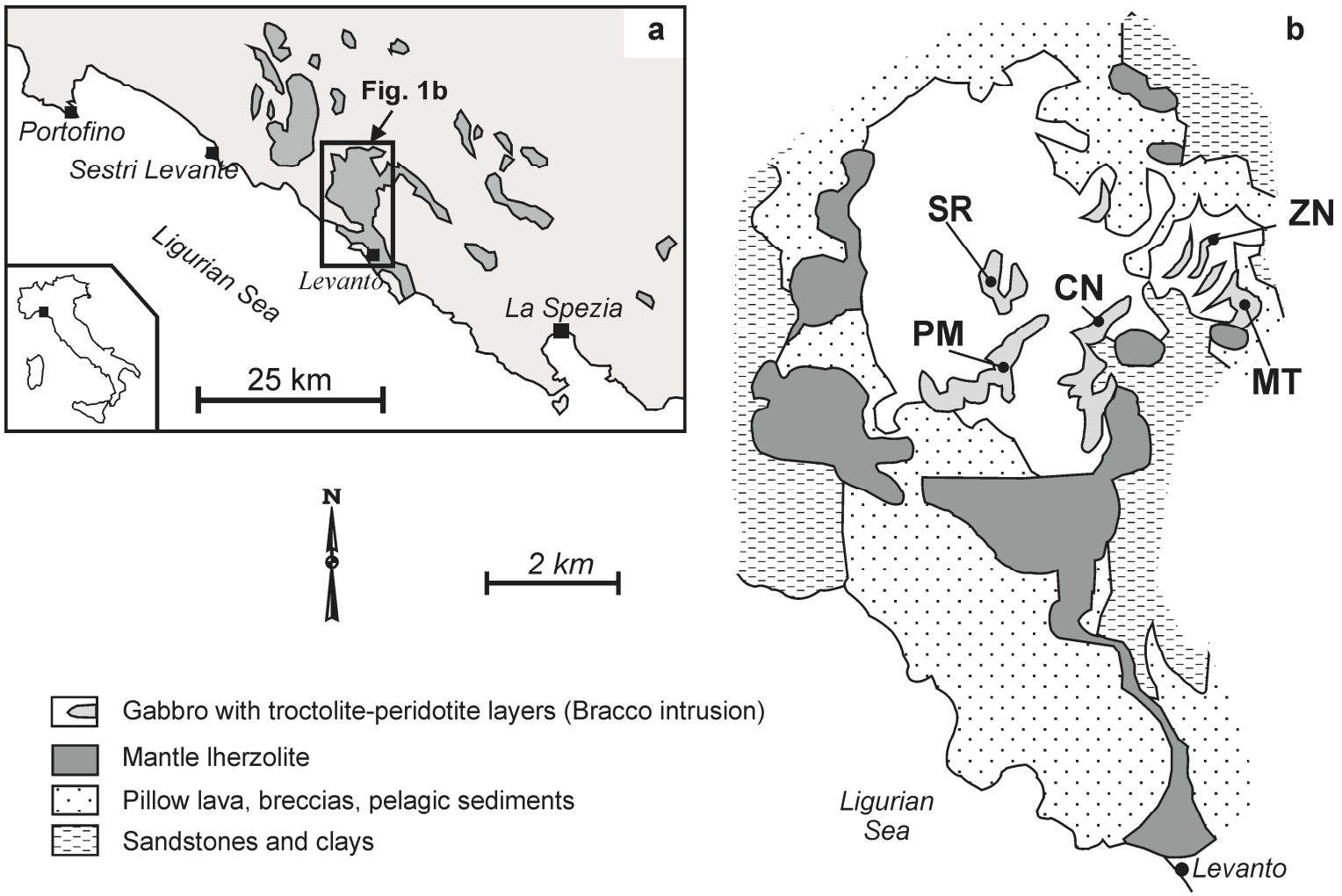

Fig. 8 a Sketch map with the main Internal Liguride ophiolitic bodies between Portofino and La Spezia. **b** Simplified geological map of the Bracco-Gabbro Complex (redrawn after Cabella et al. 2002) with the location of the studied areas. Abbreviations: SR= Cima Stronzi, ZN = Ziona, MT = Mattarana, PM = Pian della Madonna, CN = Canegreca.

10. ANALYTICAL TECHNIQUES

10.1. Microscopy

Petrological and mineralogical investigations were performed at the Chair of Resource Mineralogy, University of Leoben, on following microscopes: Olympus BX40, Zeiss Axio Scope.A1 and Zeiss Photomicroscope III. Pictures were recorded on the Zeiss Axio Scope.A1, using the camera Zeiss AxioCam ERc 5s.

10.2. Raman spectroscopy

Qualitative investigations of rock forming minerals and silicate inclusions within the chromites were performed on a LABRAM (ISA Jobin Yvon) Raman Spectrometer at the Chair of Resource Mineralogy, University of Leoben, using a frequency-doubled 120 mW Nd-YAG laser with an excitation wavelength (λ) of 532,6 nm. The instrument was calibrated using silicon and polyethylene. Raman spectra were collected between 180 and 2000 cm^{-1}. The spectral resolution of the instrument is in the order of ± 2cm^{-1}.

10.3. Electron probe microanalyses

Quantitative mineral analyses (WDS), as well as backscattered electron (BSE-) images, were carried out at the Eugen F. Stumpfl Electron-Microprobe-Laboratory, University of Leoben, using a JEOL JXA-8200 superprobe. Measurements were performed on sulphides, silicates and chromites. For calibrations of silicate analyses the following synthetic and natural mineral standards were used: Olivine (Si, Mg), Ilmenite (Ti), Chromite (Cr), Labradorite (Al), native Vanadium (V), Kaersutite (Fe), Rhodonite (Mn), Wollastonite (Ca), Pentlandite (Ni), Albite (Na), and Phlogopite (K). Chromite analyses were normalized on following standards: Ilmenite (Ti), Chromite (Cr, Al, Mg, and Fe), native Vanadium (V), Rhodonite (Mn) and Pentlandite (Ni). For quantitative analyses of chromites and silicates Kα X-ray lines were used. Analysing conditions were 15 kV acceleration voltage, 10 nA beam current and peak counting times of 15-20 s per element. Elemental distribution maps were carried out under the same analyzing conditions. For Fe^{2+}/Fe^{3+} distribution the calculation method by Droop et al. (1987) was used. Analyses on sulphides were executed at specific analytical conditions to lower the detection limits to values of <100 ppm, which are necessary to detect trace elements. For calibrations the following standards were used: Millerite (Ni, S), Chalcopyrite (Cu), Pyrite (Fe), native Platinum (Pt), native Palladium (Pd), native Rhodium (Rh), and native Rhenium (Re). These analyses were performed with an acceleration voltage of 25 kV, a beam current of 30 nA and peak counting times of 30-60 s for trace elements (Pt, Pd, Rh, Re) and 5-15 s for base metals (Fe, Cu, Ni, S). Kα, Lα and Mα X-ray lines were used for quantitative analyses on sulphides. Numerous chromitite samples were investigated in detail for platinum group minerals (PGM), using electron microscopy.

Tab. 1 Measurement conditions of electron probe microanalyses on chromites.

Element	Spectral line	Standard	Analysing crystal	Detection limit (wt%)
Ti	Kα	Ilmenite	LIFH	0.03
Al	Kα	Chromite	TAP	0.02
Cr	Kα	Chromite	LIFH	0.03
V_2	Kα	Vanadium (metallic)	LIFH	0.02
Mg	Kα	Olivine	TAP	0.02
Fe	Kα	Magnetite	LIFH	0.03
Mn	Kα	Rhodochrosite	LIFH	0.03
Ni	Kα	Pentlandite	LIFH	0.04

Tab. 2 Measurement conditions of electron probe microanalyses on silicates.

Element	Spectral line	Standard	Analysing crystal	Detection limit (wt%)
Si	Kα	Olivine	PETH	0.02
Ti	Kα	Albite	LIFH	0.02
Al	Kα	Labradorite	TAP	0.03
Cr	Kα	Chromite	LIFH	0.02
Ca	Kα	Wollastonite	PETH	0.02
Mg	Kα	Olivine	TAP	0.02
Fe	Kα	Rhodonite	LIFH	0.02
Mn	Kα	Rhodochrosite	LIFH	0.03
Ni	Kα	Millerite	PETH	0.01
K	Kα	Phlogopite	PETH	0.03
Na	Kα	Albite	TAP	0.01

Tab. 3 Measurement conditions of trace-element electron probe microanalyses on sulphides.

Element	Spectral line	Standard	Analysing crystal	Detection limit (wt%)
Cu	Kα	Chalcopyrite	LIFH	0.01
S	Kα	Millerite	PETH	0.003
Fe	Kα	Pyrite	LIFH	0.008
Pd	Lα	Pd (native)	PETH	0.003
Ni	Kα	Millerite	LIFH	0.009
Rh	Lα	Rh (metallic)	PETH	0.003
Pt	Lα	Pt (metallic)	LIFH	0.008
Re	Mα	Re (metallic)	PETH	0.01

Tab. 4 Measurement conditions of base-metal electron probe microanalyses on sulphides.

Element	Spectral line	Standard	Analysing crystal	Detection limit (wt%)
As	Lα	Skutterudite	TAP	0.03
Fe	Kα	Pentlandite	LIFH	0.02
S	Kα	Chalcopyrite	PETH	0.01
Co	Lα	Skutterudite	LIFH	0.03
Ni	Kα	Millerite	LIFH	0.03
Zn	Lα	Gahnite	LIFH	0.06
Cu	Lα	Chalcopyrite	LIFH	0.04

10.4. Instrumental neutron activation analysis

Selected rock samples were analyzed for PGE and Au by instrumental neutron activation analysis (INAA), after Ni-sulphide pre-concentration with Te-co-precipitation. The analyses were carried out at the University of Pavia, Italy, following the procedure described by Garuti et al. (2000), and at the XRAL Laboratories in Ontario, Canada. Average detection limits were in the order of 1 ppb for all analyzed metals except Ir (d.l. < 1.0 ppb) and Os (d.l. = 3.0 ppb). For chondrite normalization we used the values suggested by Naldrett and Duke (1980). Sulphur was analyzed by X-ray fluorescence (d.l. ~100 ppm). PGE-whole rock analyses from Cabella et al. (2002) were incorporated in this study.

11. FIELD RELATIONSHIPS

Samples of chromitite and associated ultramafic rocks were collected during a field trip, between the 9th and 13th of June 2012, at the localities of Ziona, Cima Stronzi, Mattarana, Pian della Madonna and Canegreca (Fig. 8b). Chromitite is exclusively associated with the internal layering of ultramafic lenses, usually in close vicinity to the transition into gabbroic cumulates. The chromitite outcrops are very small, fractured, masked by alteration and covered by vegetation. It was not possible to obtain good field images of them.

The Ziona deposit consists of swarms of centimetre- to decimetre-size pods, lenses and ribbon-like bodies, sometimes arranged in anastomosing patterns within a gangue matrix of melatroctolite. True chromitite layers are absent. However, the small ore bodies occur distributed in a tabular zone extending hundreds of metres, along the contact between the ultramafic rocks and the adjacent layered gabbros, with a maximum thickness of about 30-40 centimetres (Stella 1924; Bezzi and Piccardo 1970).

At the Cima Stronzi occurence, mafic and ultramafic rocks occur with rhythmic repetition of melatroctolite-troctolite-anorthosite cyclic units, between 0.1 and 1.0 m in thickness (Fig. 9). The base of the cyclic units is locally marked by thin (0.5 – 3.0 cm) layers of olivine and chromite (dunite) or chromitite. The most common ore type consists of a centimetres thick chromitite layer, having plagioclase as the interstitial phase in its lower part, and olivine in the upper one. The plagioclase-chromitite overlies the anorthosite of the underlying unit, frequently showing wavy sharp contacts (Bezzi and Piccardo 1970). Some textures appear as “load casts”, suggesting that chromite settled at least a short distance in a fluid milieu and deposited over a dense and partly unconsolidated material (anorthosite). The olivine-chromitite grades upwards into a dissemination of chromite grains within dunite or melatroctolite.

Chromitite samples from Mattarana were collected in the Cava della Baracca and in other outcrops located a few hundred meters north of the Aurelia Roman Road. The main rock is an olivine-chromite cumulate with plagioclase and pyroxene as intercumulus and adcumulus phases (Bezzi and Piccardo 1970). The true layering reported by Bezzi and Piccardo (1970) was not observed during this study.

Only a few samples could be collected from Pian della Madonna and Canegreca, due to the scarcity of outcrops. Chromitite layering is a common ore type at both localities. The layers have a thickness between 0.5 and 3-4 cm and developed at the base of melatroctolite-troctolite-anorthosite cyclic units. The interstitial chromitite ore of the Mattarana-type was also observed. At Canegreca, closely packed chromite aggregates form centimetre size wispy, discontinuous vermiculations and veinlets within completely serpentinized melatroctolite (Ziona-type ore?).

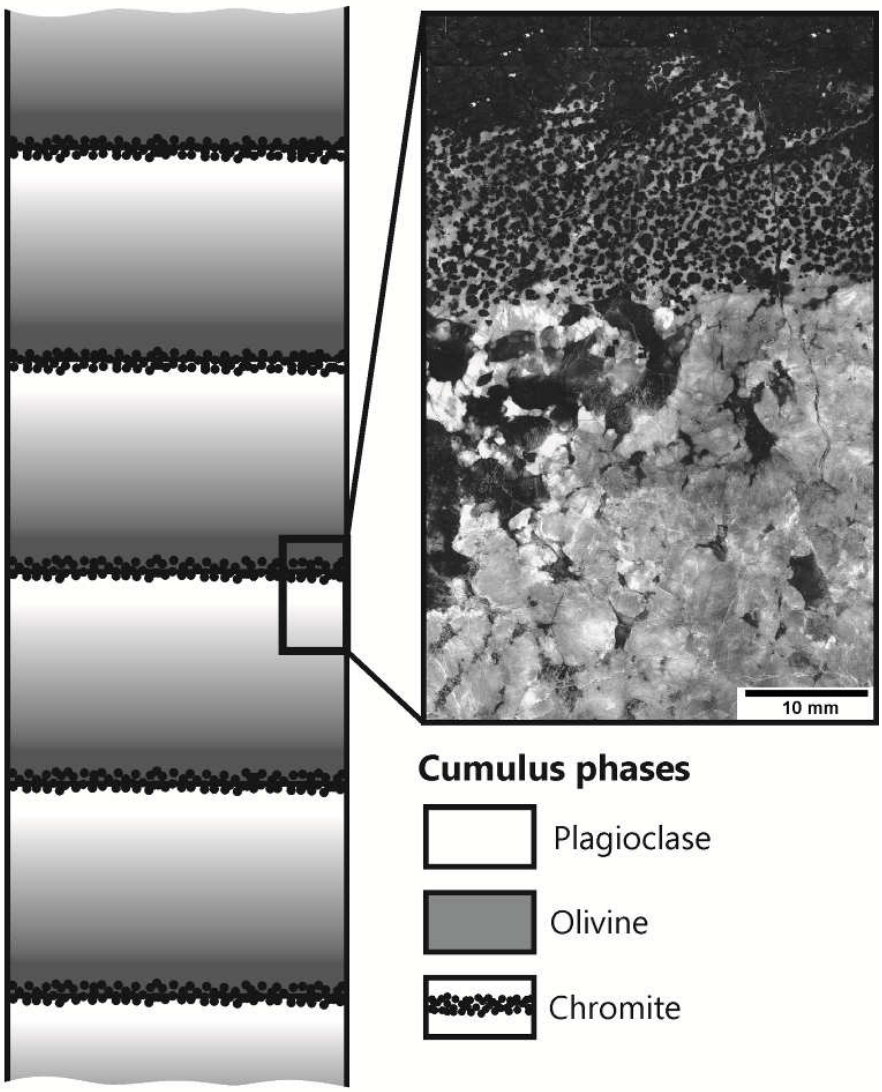

Fig. 9 Schematic illustration of the melatroctolite-troctolite-anorthosite macro-rhythmic units present at the Cima Stronzi occurrence. Chromitite layer appear at the transition between cumulus anorthosite and dunite.

12. PETROGRAPHY AND MINERALOGY

12.1. Chromitites

The chromitites are commonly composed of fine grained (<3 mm), partially fractured, euhedrally to subhedrally shaped crystals and display a cumulus texture (Fig. 10). The most common ore type consists of individual crystals closely packed in a cumulus texture, only separated one from the other by thin films of intercumulus anorthite and Cr-rich clinochlore as well as minor serpentine. Size grading (graded bedding) is rarely observed within the layers. Cumulus olivine usually shows a partially interpenetrating non-pseudomorphic ribbon texture, dominated by secondary magnetite. Rarely a relictic mesh structure with fibrous serpentine adjacent to hourglass textured cores is observable. Bastitic serpentine pseudomoprhs after pyroxene are almost absent. Chlorite is a common accessory mineral and forms patches always close to the chromitites (Fig. 11).

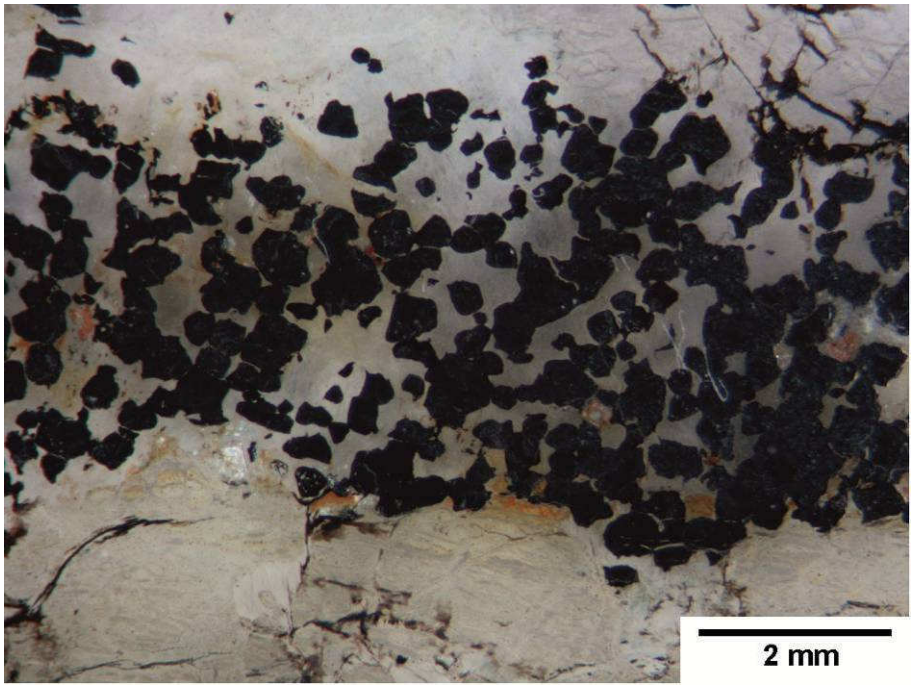

Fig. 10 Image of a chromitite layer from the Cima Stronzi occurrence.

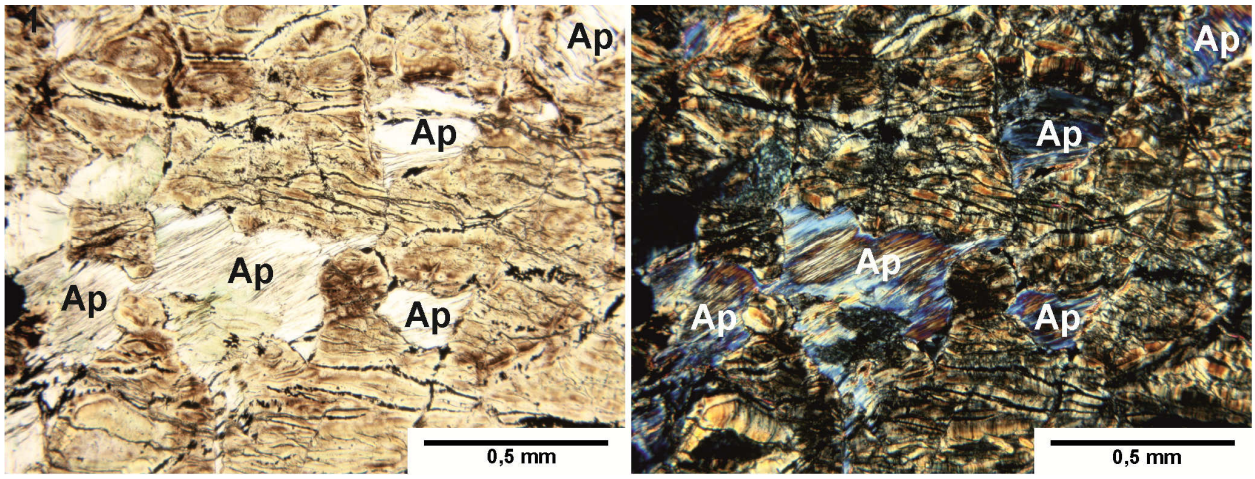

Fig. 11 Microscopic images of the serpentinized olivine cumulates under transmitted light (parallel polarizers on the left; crossed polarizers on the right). Abbreviations: Ap = apenninite (clinochlore)

The chromitites are for the most part partially to completely altered, but rarely completely fresh. The most common alteration products are ferrian chromite rims with a thickness of up to 100 µm. The ferrian chromite rims probably represent a first alteration stage (Fig. 12a). However, primary chromite is usually preserved by the cores of partially altered grains. In a second stage of alteration, the ferrian chromite rims were replaced by a porous mixture composed of Fe oxides and hydroxides as well as chlorite (Fig. 12a). Alterations are not only restricted to the outer crystal faces, they have been also developed along cracks and fissures (Fig. 12a). Within a single chromitite layer, the second alteration stage is usually visible only in the inner part of the layers. Chromites in contact with the host rock have been not affected by this alteration, as shown in Fig. 12b.

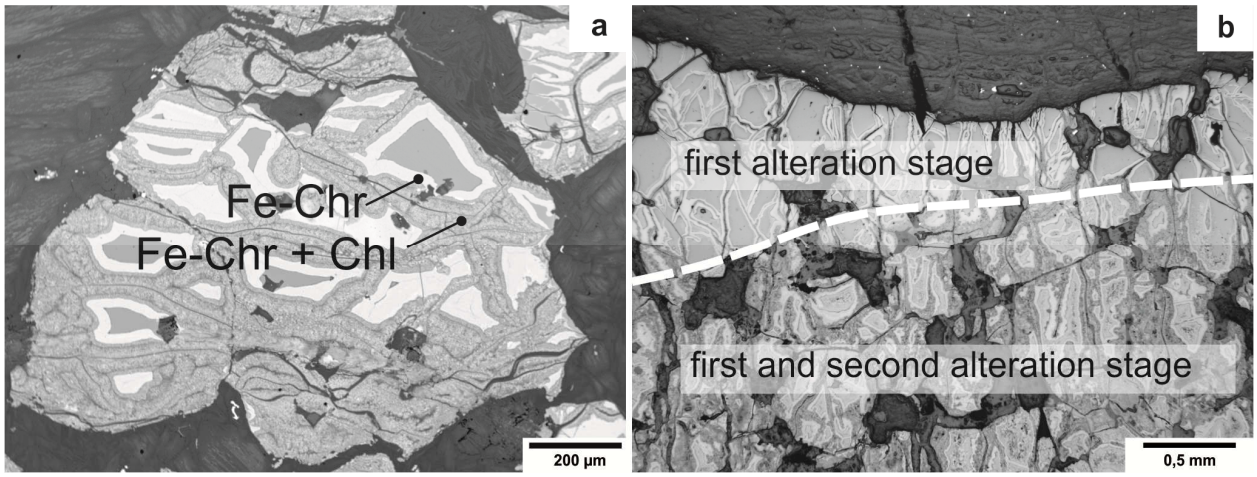

Fig. 12 a Backscattered electron (BSE-) image of an altered chromite that is partially replaced by ferrian chromite. The ferrian chromite rim, in turn, was replaced by a porous mixture of Fe oxides and chlorite. **b** Microscopic image (parallel polarizers) of an intensively altered chromitite layer. Abbreviations: Fe-Chr = ferrian chromite, Chl = chlorite

12.2. Melatroctolites

The melatroctolites are medium to coarse grained rocks that show a cumulus texture composed of partially to totally altered, subhedral olivine and poikilitic pyroxene, embedded in a mesh texture of altered plagioclase (Fig. 13). Plagioclase, now transformed to prehnite (Fig. 14), reaches contents up to 30 wt%. The olivine cumulates are extensively serpentinized, but relics of olivine are still preserved. They contain also minor amounts of fine grained (<1 mm) as well as subhedral chromite, secondary magnetite and needle shaped rutile. Coarse grained as well as euhedral chromite crystals, up to 3 mm in size, are associated with the interstitial prehnite (transformation product after plagioclase), whereas fine grained chromite (<1 mm) occurs in poikilitic pyroxene (Fig. 15), represented by diopside and minor augite.

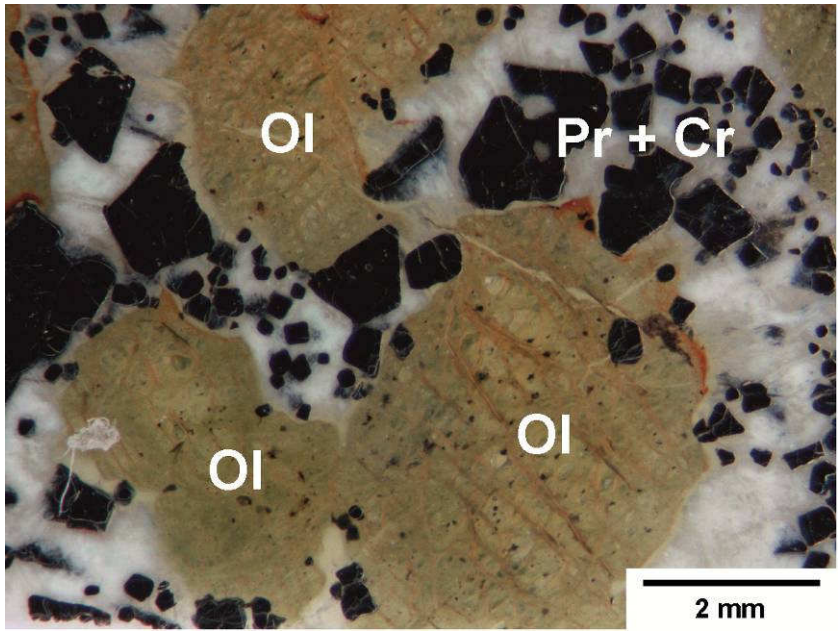

Fig. 13 Image of a troctolite sample. Rather euhedrally shaped chromites are associated to prehnite interstitially to olivine cumulates. Abbreviations: Cr = chromite, Ol = olivine, Pr = prehnite

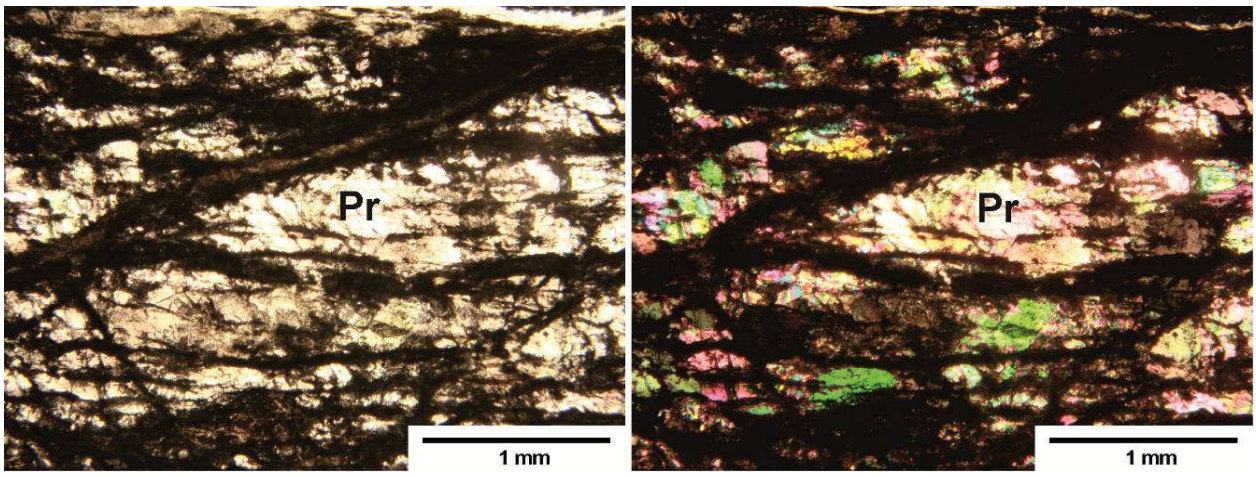

Fig. 14 Microscopic images of prehnite, still showing visible crystals (parallel polarizers on the left; crossed polarizers on the right). Prehnite has colourful interference effects at polarized light. Abbreviations: Pr = prehnite

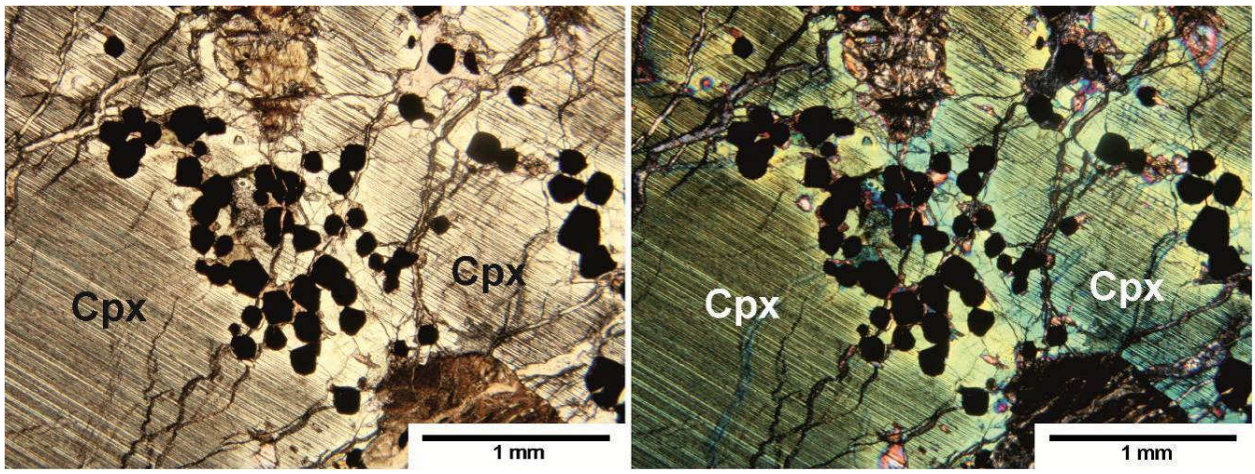

Fig. 15 Microscopic images of euhedrally shaped chromites within irregular formed patches of clinopyroxene (parallel polarizers on the left; crossed polarizers on the right). Clinopyroxenes show a good facility and interference colours from light green to blue. Abbreviations: Cpx = clinopyroxene

12.3. Serpentinized dunites

Samples of serpentinized dunite were collected at Cima Stronzi. They are massive, dark-blue to black rocks that rarely contain plagioclase rich veinlets. On microscale, the rocks have a diagnostic mosaic texture of olivine pseudomorphs surrounded by secondary magnetite. The rock contains mainly fresh disseminated chromites, up to several millimetres in size, with euhedral crystal shape (Fig. 15). The chromites are usually coated and filled (along open fractures) by secondary magnetite, as a result of serpentinization.

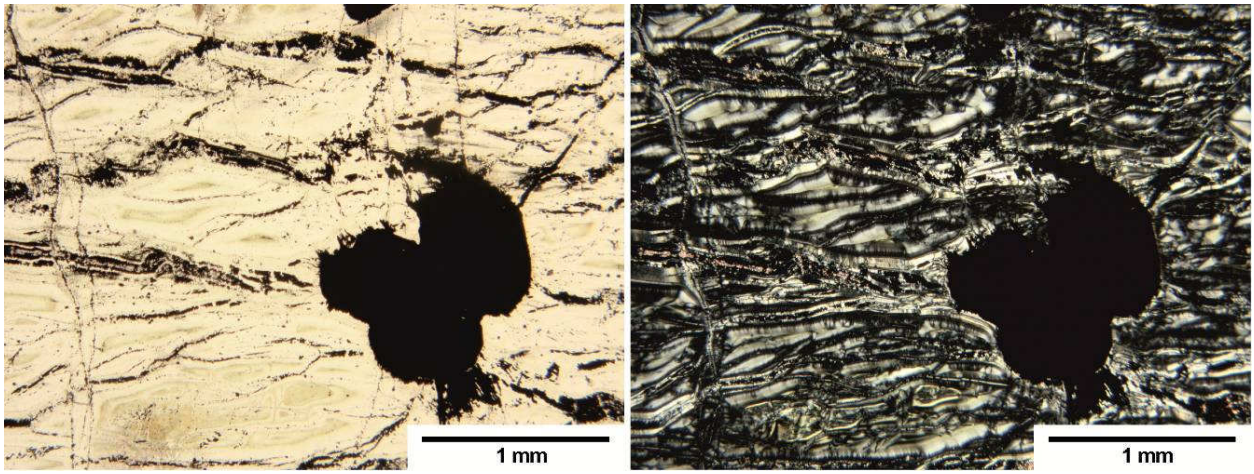

Fig. 16 Microscopic images of euhedrally shaped chromites within the intensively serpentinized dunites from Cima Stronzi (parallel polarizers on the left; crossed polarizers on the right).

12.4. Silicate and oxide inclusions

Chromites from the chromitites and the serpentinized dunites usually contain abundant silicate inclusions. The inclusions are randomly distributed, with a size ranging from a few microns up to 0.5 mm. Their shape is mainly irregular but sometimes round or even polygonal. The latter possibly represent the filling of negative crystal cavities. Inclusions in strongly altered chromites are not well preserved, showing almost complete alteration. Monomineralic silicate inclusions are rare; they are dominantly polyphase consisting of anhydrous high-T phases (olivine, clinopyroxene, and orthopyroxene), hydrous high-T phases (pargasitic amphibole, phlogopite) and less common hydrous low-T phases (analcime, chlorite). Inclusions of enstatitic orthopyroxene, pargasitic amphibole, phlogopite and chlorite are common in the chromitites (Fig. 17a). Aggregates of pargasitic amphibole, olivine, and diopside were observed in the chromite from dunites (Fig. 17b). The silicate inclusions may also be accompanied by oxides, such as Mg- as well as Mn-rich ilmenites and rutile. The occurrence of badelleyite and loveringite accompanied by titanite and apatite has been reported by Cabella et al. (1997).

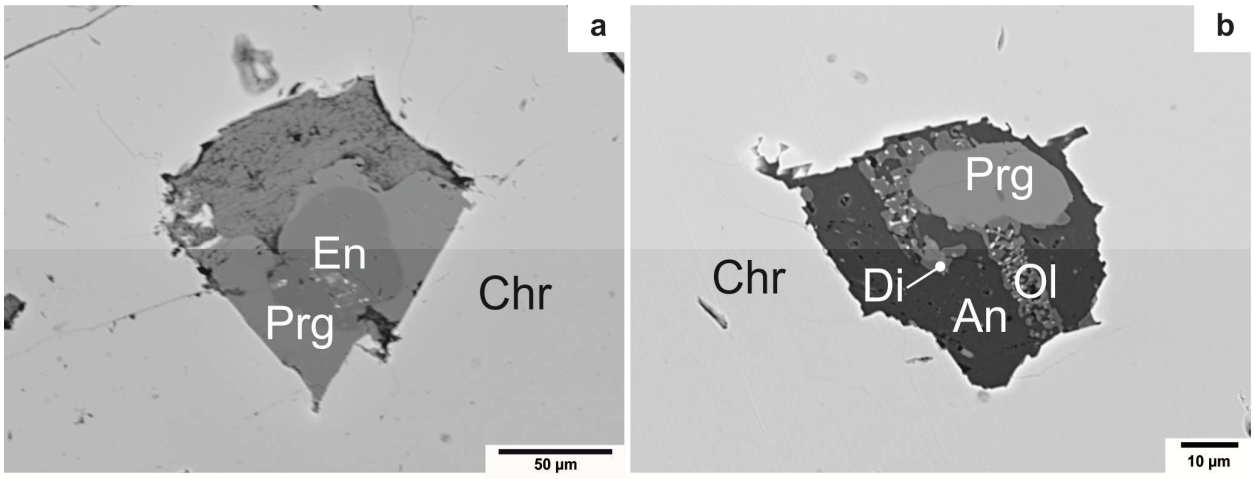

Fig. 17 a,b BSE-images of polyphase silicate inclusions in chromite from chromitite (a) and dunite (b). Abbreviations: An = analcime, Chr = chromite, Di = diopside, En = enstatite, Ol = olivine, Prg = pargasite

12.5. Sulphides

Sulphides, associated with the chromitites, occur as either irregular aggregates (up to 10 mm) within the silicate matrix or minute (< 500 μm) bleb-like grains included in fresh chromite (Fig. 18a). Pentlandite, pyrrhotite and minor chalcopyrite, locally accompanied by millerite, heazlewoodite and violarite, are the most abundant components of the interstitial sulphide aggregates. Exsolution lamellae (flame textured blebs or stringers) of pentlandite rarely occur in pyrrhotite. The bleb-like sulphide inclusions in chromite are polygonal or round shaped and display variable mineral assemblages: pentlandite-chalcopyrite-pyrrhotite (Fig. 18b), chalcopyrite-millerite-bornite, chalcopyrite-pentlandite with or without pyrrhotite and mackinawite. Several interstitial sulphide associations are characterized by progressive alterations. The most common alteration is ascribed to the breakdown of pentlandite as well as pyrrhotite to violarite ± magnetite. Notably, the secondary sulphides (violarite, heazlewoodite), derived from low-temperature alteration, occur exclusively in the interstitial aggregates and are absent in the blebby inclusions. They were preserved from alteration by the chromite.

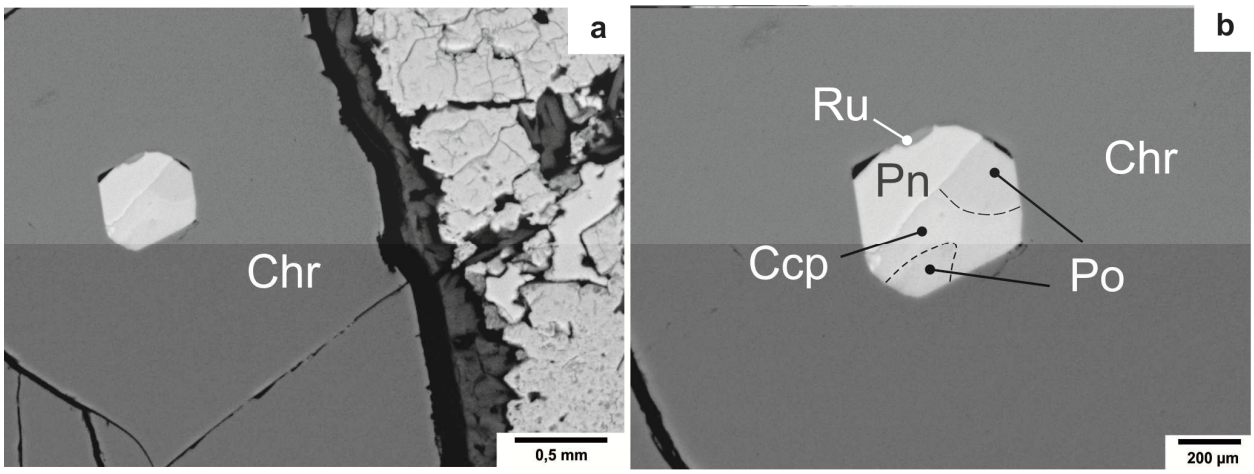

Fig. 18 a,b BSE-images of sulphides associated to the chromitites. They appear interstitially to (a), or as inclusions in the chromites (b). Abbreviations: Ccp = chalcopyrite, Pn = pentlandite, Po = pyrrhotite, Ru = rutile

13. ANALYTICAL RESULTS

13.1. Raman spectroscopy

13.1.1. Chromite

Chromite has a broad range of chemical composition due to the substitution of divalent and trivalent cations at tetrahedral and/or octahedral sites. Therefore, major peak positions in the Raman spectra shift over a respectable range. The magnesiochromite (end-) member has a major broad peak at ~685 cm^{-1} which is related to the vibrational modes at the octahedral sites [$(Cr^{3+},Fe^{3+},Al^{3+})O_6$]. A smaller peak, which is usually overlapped for the most part, appears near 650 cm^{-1}. Other minor peaks may be observed at ~610, ~520 and ~450 cm^{-1}. The spectral position of the major peak is strongly related to the substitution Cr/Al at octahedral sites and lies between ~685 and 770 cm^{-1} (Wang et al. 2004, and references therein).

Analyzed chromite crystals show characteristic peaks at ~600, ~670 and ~720 cm^{-1} (Fig. 19). The spectral position of the major peak at ~720 cm^{-1} indicates a significant Al substitution at the octahedral sites.

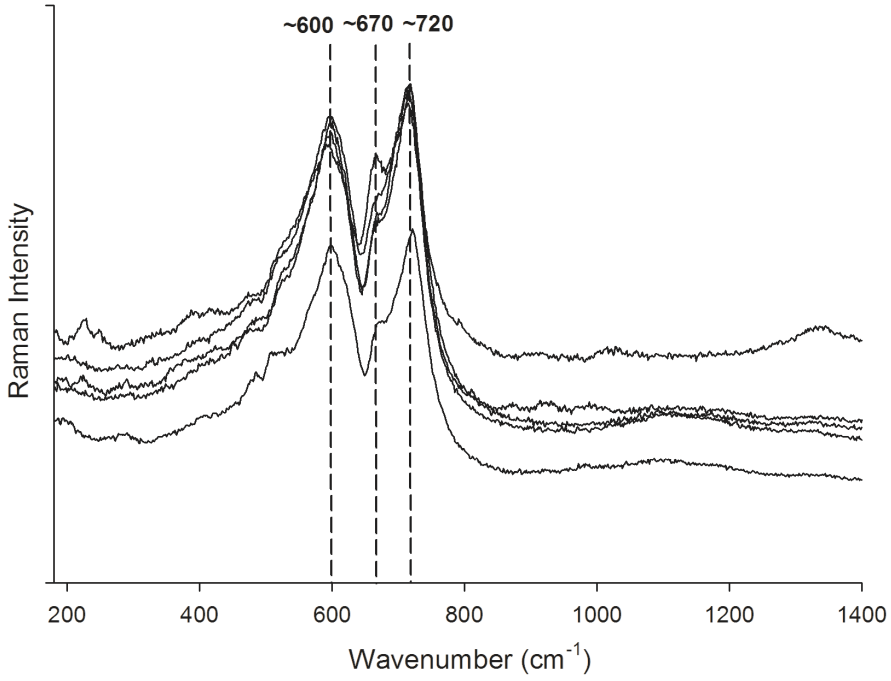

Fig. 19 Raman spectra of analyzed chromites.

13.1.2. Phyllosilicates

Phyllosilicates have characteristic peaks in the spectral region <600 cm^{-1}, due to several translation motions of octahedral and interlayer cations, oxygen atoms and OH-groups. Mg-rich members have one characteristic peak at ~350 cm^{-1}, whereas the equivalent peak is at ~420 cm^{-1} regarding Al-rich members and at ~550 cm^{-1} regarding Fe-rich members. Peaks between 600 and 800 cm^{-1} are the consequence of vibrational Si-O-Si modes. Tri-octahedral phyllosilicates usually have one characteristic peak between 670 and 700 cm^{-1}, whereas di-octahedral phyllosilicates have more dispersed peaks in the spectral region >700 cm^{-1}. Peaks between 800 and 1150 cm^{-1} are related to the stretching modes of non-bridging Si-O-Si bonds (Wang et al. 2002).

Serpentine (crysotile), that comes from the alteration of cumulus olivine, shows characteristic peaks at ~230, ~350, ~385, ~620 and ~685 cm^{-1}, as well as two moderate peaks between 1000 and 1100 cm^{-1} (Fig. 20a). The Raman spectrum of chlorite assoiated to the serpentines has major peaks at ~200, ~355, ~550 and ~680 cm^{-1}, as well as minor peaks at ~285, ~355, ~385, ~460, ~1060 and ~1090 cm^{-1} (Fig. 20b).

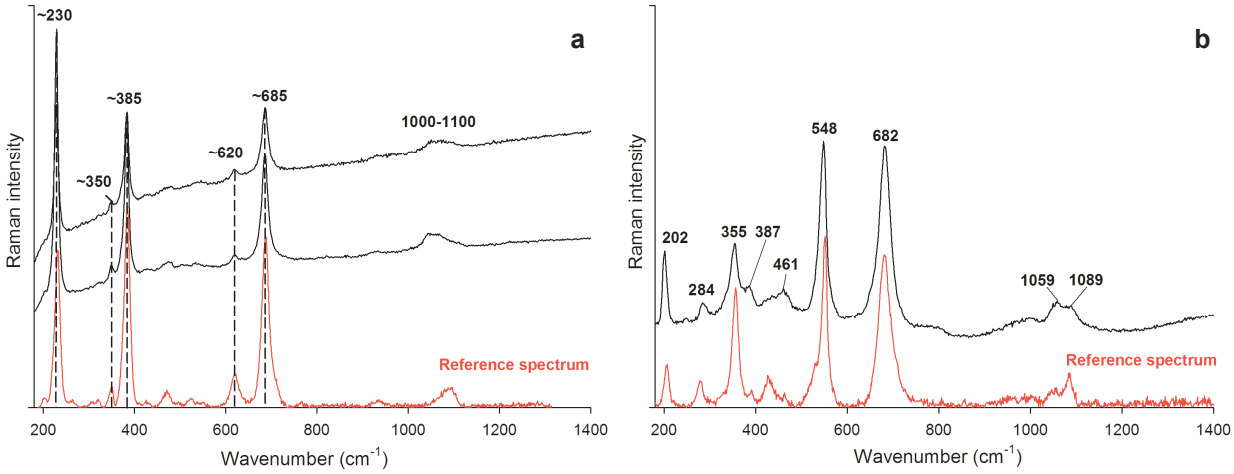

Fig. 20 a,b Raman spectra of crysotile (a) and chlorite (b). The data for the reference spectra are taken from Rruff project database (2012).

13.1.3. Prehnite

The Raman sprectrum of prehnite, taken from a melatroctolite rock sample, shows characteristic peaks at 221, 319, 389, 522, 609, 689, 783, 936, 992 and 1082 cm^{-1} (Fig. 21). The peak positions are consistent with the reference spectrum taken from Rruff project database (2012).

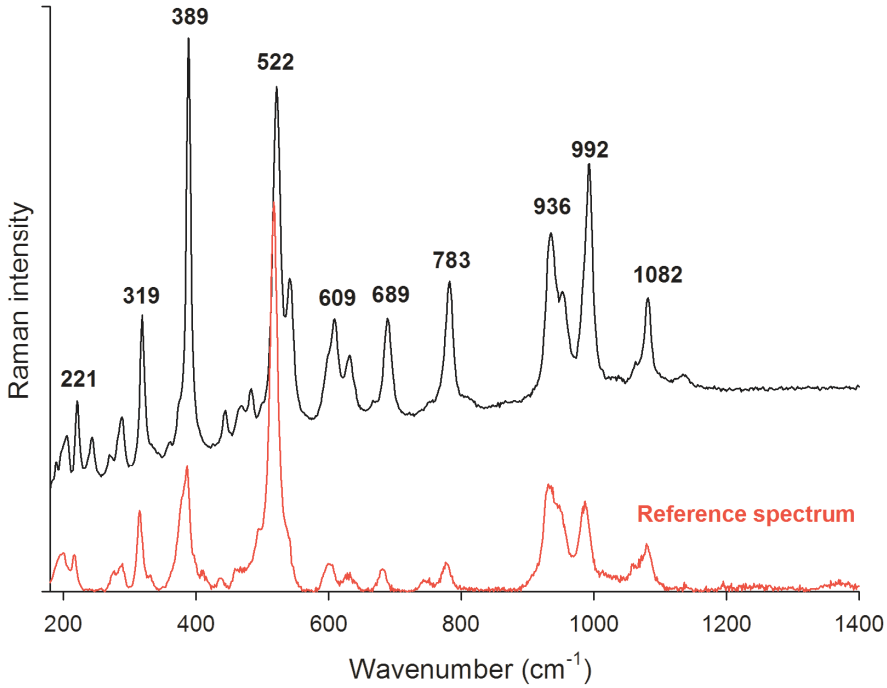

Fig. 21 Raman spectrum of prehnite from a melatroctolite rock sample. The data for the reference spectrum is taken from Rruff project database (2012).

13.1.4. Silicate inclusions in chromites

Olivine

The Raman spectrum of olivine has several characteristic peaks between 800 and 1000 cm^{-1}. For instance, forsterite has well defined peaks at 824, 856, 920 and 966 cm^{-1}, because of the symmetric and asymmetric stretching of Si-O bonds (SiO_4 tetraheda). The weak peak in the spectral region of ~880 cm^{-1} is usually overlapped by the peak present at ~856 cm^{-1} (Kakkala and Sharma 1993; Kolesov and Geiger 2003).

The olivine inclusions in chromite have characteristic peaks at ~820, ~855, ~915 and ~960 cm^{-1}, as shown in Fig. 22.

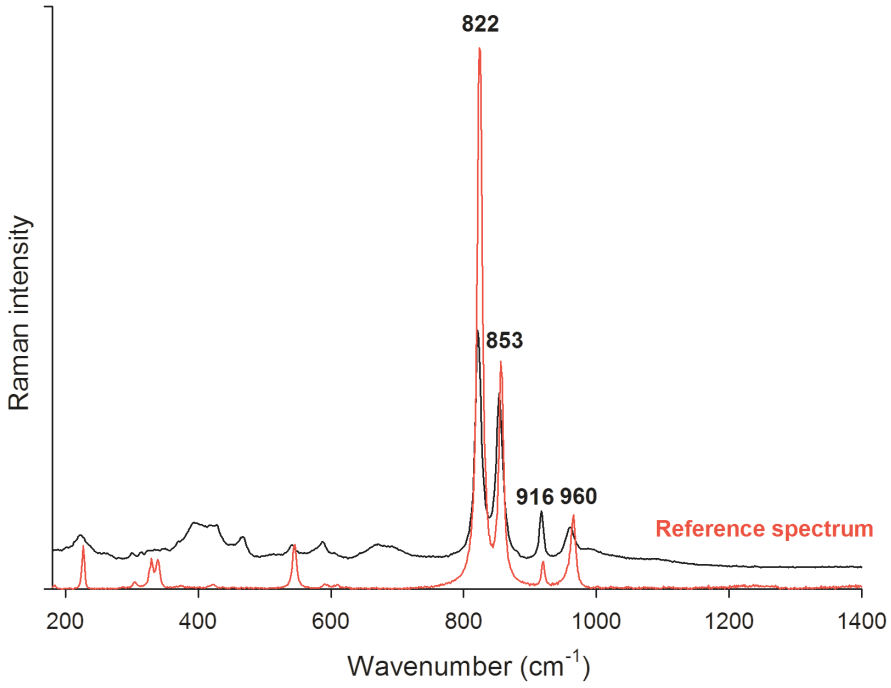

Fig. 22 Raman spectrum of olivine included in chromite. The data for the reference spectrum is taken from Rruff project database (2012).

Pyroxene

Pyroxenes of the enstatite-ferrosilite series are characterized by three weak peaks below 360 cm^{-1} (vibrational modes of the M-O bonds), two moderate peaks between 600 and 700 cm^{-1} (symmetric stretching of the bridging Si-O bonds), as well as three intense peaks between 900 and 1050 cm^{-1} (symmetric stretching of the non-bridging Si-O bonds). Members of the diopside-hedenbergite series show three weak peaks below 360 cm^{-1}, two moderate peaks between 600 and 700cm^{-1}, as well as three peaks between 900 and 1050 cm^{-1}. Orthopyroxenes from the enstatite-ferrosilite and the diopside-hedenbergite series are usually discriminable by one characteristic peak between 800 and 900 cm^{-1} (>854 cm^{-1} for orthopyroxenes and <856 cm^{-1} for clinopyroxenes; Huang et al. 2000; Buzatu and Buzgar 2010).

Diopside inclusions in chromite show main peaks at ~665, ~855 and ~1010 cm^{-1}. A season of peaks occurs between 300 and 400 cm^{-1} (~325, ~360 and ~390 cm^{-1}). Several weak peaks are at ~225, ~505, ~555, ~855 and ~1040 cm^{-1} (Fig. 23b). Estatite inclusions show main peaks at ~225, ~340, ~660, ~680, ~1005 and ~1025 cm^{-1} (Fig. 23b). Some weak peaks are at the spectral region between 380 and 410 cm^{-1}, between 500 and 600 cm^{-1}, at ~850 cm^{-1}, as well as at ~930 cm^{-1}.

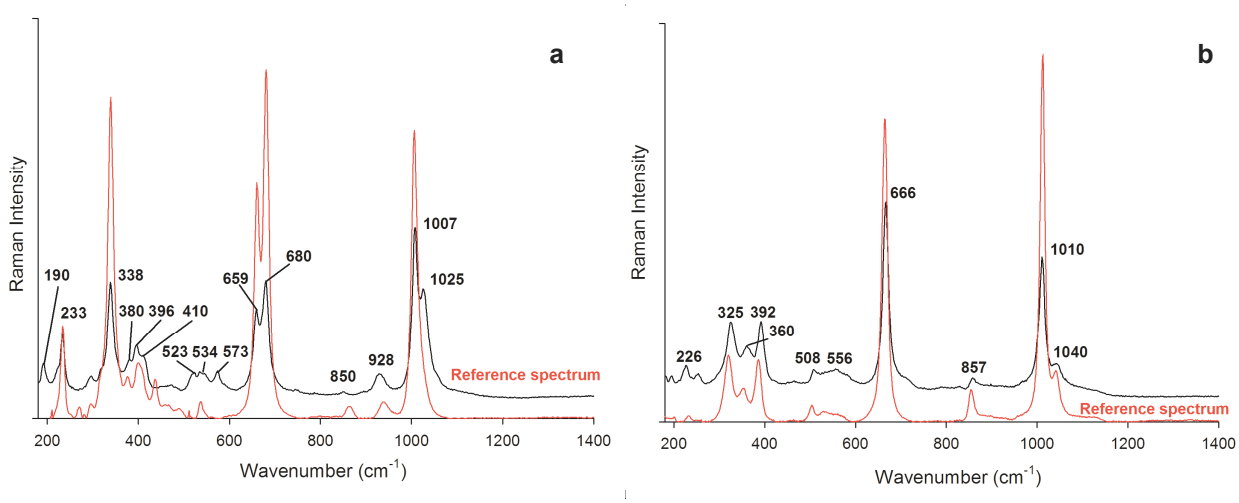

Fig. 23 a,b Raman spectra of diopside (a) and enstatite (b) inclusions in chromite. The data for the reference spectra are taken from Rruff project database (2012).

Pargasite

Amphiboles have a number of vibrational modes between 200 and 625 cm^{-1}, due to OH^- librations and translations. The peaks between 650 and 750 cm^{-1} are caused by the symmetric stretching of bridging O-Si-O bonds. Those between 750 and 950 cm^{-1} are linked to the symmetric stretching of non-bridging O-Si-O bonds. Peaks in the range of 950-1030 cm^{-1} are caused by the symmetric and/or asymmetric stretching of the bridging as well as the non-bridging O-Si-O bonds (Apopei and Buzgar 2010).

The Raman spectra of pargasite included in chromite have distinct peaks at ~225, ~240, ~330, ~380, ~420, ~560, ~670, ~ 790 and ~910 cm^{-1}, as well as between 1010 and 1050 cm^{-1} (Fig. 24). Amphiboles have a complex structure and a variable chemical composition. Therefore, peak positions vary or disappear even within specific subgroups or group members, as shown in (Fig. 24).

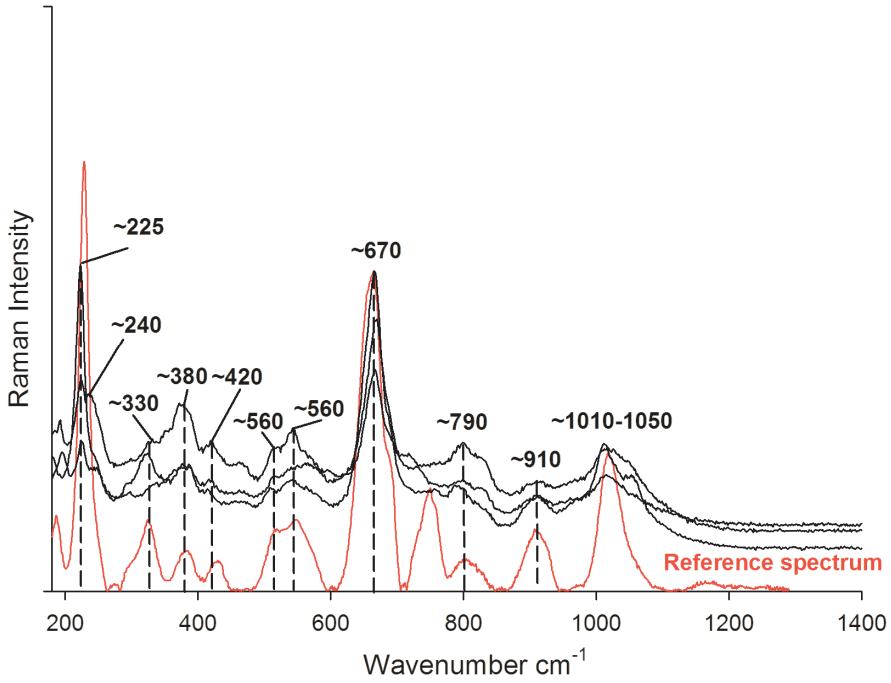

Fig. 24 Raman spectra of pargasite inclusions in chromite. The data for the reference spectrum is taken from Rruff project database (2012).

Phlogopite/Chlorite

Phlogopite inclusions are characterized by characteristic peaks at ~200, ~280, ~360, ~665 and ~1020 cm^{-1}. Unusual peaks occur at ~715 and ~790 cm^{-1}. They are may be caused by the substitution Mg/Fe, as usual for micas of the biotite group (Fig. 25a). Clinochlore inclusions have main peaks at ~200, ~355, ~550 and ~680 cm^{-1}, as well as minor peaks at ~285, ~385 and ~460 cm^{-1}. Two partially overlapped peaks usually occur between 1060 and 1090 cm^{-1} (Fig. 25b).

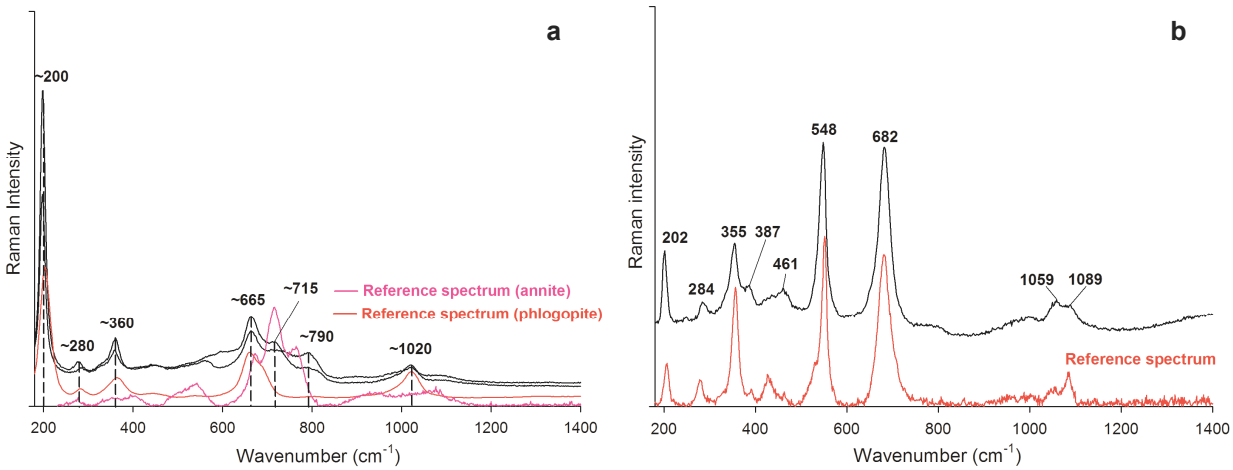

Fig. 25 a,b Raman spectra of phlogopite (a) and clinochlore (b) inclusions in chromite. Data for the reference spectra are taken from Rruff project database (2012).

13.2. Electron probe microanalyses

13.2.1. Chromites

Almost 260 microprobe analyses were performed on chromite from the massive chromitites and accessory chromite from the melatroctolites and serpentinized dunites. In chromitites, chromite composition exhibits the following variation ranges: 30.97-40.19 wt% Cr_2O_3, 22.31-31.91 wt% Al_2O_3, 17.52-24.13 wt% total iron as FeO, 11.11-15.81 wt% MgO, 0.36-0.82 wt% TiO_2, 0.12-0.38 wt% MnO, and 0.06-1.00 wt% NiO. Their Mg# [$Mg/(Mg+Fe^{2+})$] and Cr# [Cr/(Cr/Al)] vary from 0.52 to 0.73, and 0.40 to 0.55, respectively. Therefore, most of the analyses plot in the spinel field typical of Al-rich podiform chromitites and only a few compositions enter the magnesiochromite and chromite fields (Fig. 26a). Compositions of accessory chromite in dunite are within the ranges of the chromitites. However, accessory chromites from the melatroctolites are enriched in total FeO (25.5-38.4 wt%) and TiO_2 (0.75-1.53 wt%), and show relatively high Cr# (0.45-0.59), possibly due to re-equilibration with co-existing plagioclase. A selection of representative electron probe microanalyses on chromites is given in Tab 5.

The chromitites display a broad decrease of Cr# with decreasing Mg# that is the trend expected as a result of magmatic differentiation (Fig. 26a). Furthermore, the relatively high TiO_2 content (Fig. 26b) in the Bracco chromites, as a whole, are not consistent with typical values observed in podiform chromitites from the mantle unit of ophiolite complexes (< 0.30 wt% TiO_2), but resemble more closely the high TiO_2 contents typical of stratiform chromitites. Finally, the Al_2O_3-TiO_2 relationships are consistent with spinel precipitated from a MORB-type melt, with compositions from melatroctolites being at the Al_2O_3-poor and TiO_2-rich end of the MORB field (Fig. 26c). The calculated Fe_2O_3 content in chromite is relatively high, increasing from 6.2 wt% in chromitites, to 10.5 and 12.2 wt% in accessory chromite from dunite and melatroctolite.

Within one chromitite layer, chromite compositions obtained from relictic chromite cores and those from totally fresh chromites are very similar, suggesting that the alteration has not modified the primary magmatic composition of the chromites. The chromite alteration rims are characterized by a significant decrease of Al_2O_3 and MgO, whereas the FeO and Cr_2O_3 increase (Fig. 27). Their Mg# and Cr# range between 0.22 and 0.41, as well as 0.89 and 0.93, respectively. The Fe_2O_3 is extremely high (Tab. 5), with a strong increase of the Fe^{3+}/Fe^{2+} oxidation ratio, indicating chromite alteration under oxidizing conditions. High concentrations of SiO_2 (up to 4.3 wt%) were detected in altered chromite rims, due to the presence of a silicate phase (possibly chlorite) filling the pores in spongy ferrian-chromite. An unusual feature of the alteration pattern of the Bracco chromites is the extremely high concentration of Mn, with values up to 4.1 MnO wt% (Fig. 27).

Tab. 5 Analyses on selected chromites from the Bracco-Gabbro Complex.

Locality	SR	SR	SR	SR	SR	ZN	ZN	ZN	PM	PM	PM	CN	CN	CN	SR	SR	MT	MT
Rock type	Chr	Chr	Chr	Chr*	Chr*	Chr	Chr	Chr	Chr	Chr	Chr	Chr	Chr	Chr	Du	Du	Mtr	Mtr
SiO_2				3.75	3.47													
TiO_2	0.52	0.69	0.46	0.64	0.70	0.54	0.53	0.68	0.70	0.60	0.60	0.55	0.50	0.62	0.58	0.77	1.43	0.91
Al_2O_3	31.05	24.03	29.77	1.88	1.79	26.53	26.72	26.06	28.74	27.53	27.90	31.36	31.68	31.50	25.23	23.70	23.12	26.22
Cr_2O_3	31.89	39.24	34.42	33.02	33.26	38.88	38.91	38.65	35.89	35.77	36.05	32.75	32.74	32.50	35.16	37.12	34.32	32.89
V_2O_3	0.15	0.15	0.16	0.15	0.12	0.18	0.17	0.15	0.21	0.18	0.16	0.08	0.12	0.20	0.18	0.23	0.26	0.19
MgO	11.33	14.50	12.44	3.54	3.48	14.34	14.58	14.61	11.71	12.78	12.90	12.79	12.46	12.43	14.09	13.55	9.77	11.20
FeO	24.04	20.04	20.34	51.67	51.58	19.26	18.86	18.79	22.59	21.12	20.79	19.12	19.53	19.44	22.20	23.04	31.87	27.25
MnO	0.23	0.27	0.18	5.60	5.69	0.19	0.25	0.30	0.27	0.22	0.26	0.14	0.17	0.16	0.32	0.30	0.25	0.23
NiO	0.48	0.17	0.65	0.06	0.29	0.21	0.14	0.16	0.20	0.53	0.57	0.91	0.89	0.77	0.03	0.18	0.36	0.36
Total	99.69	99.09	98.42	100.31	100.38	100.13	100.16	99.40	100.31	98.73	99.23	97.70	98.09	97.62	97.79	98.89	101.38	99.25

*, ferrian chromite; Chr, chromite; CN, Canegreca; Du, dunite; MT, Mattarana; Mtr, melatroctolite; PM, Pian della Madonna; SR, Cima Stronzi; ZN, Ziona

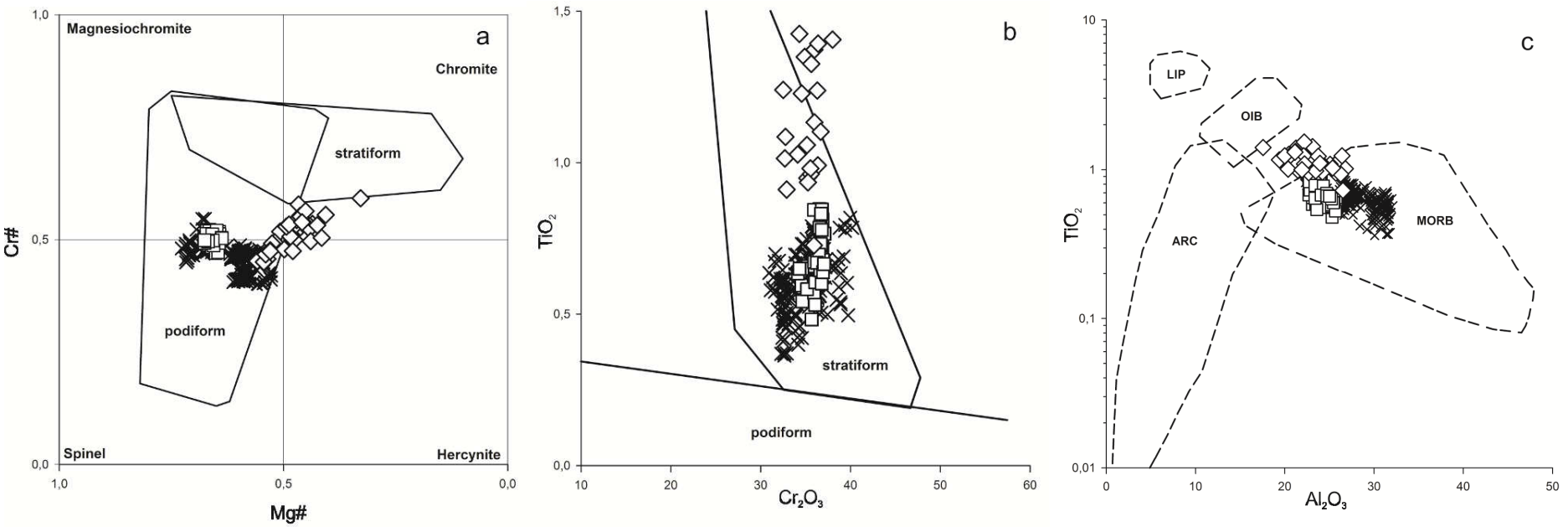

Fig. 26 a Classification diagram for chromites in terms of their Mg# vs. Cr# (discrimination fields after Irvine 1967 and Leblanc and Nicolas 1992) **b** Composition of the chromites in terms of their Cr_2O_3 vs. TiO_2 (discrimination fields after Ferrario and Garuti 1988 and Arai et al. 2004) **c** Composition of the chromites in the diagram Al_2O_3 vs. TiO_2. The discrimination fields for mid ocean ridge basalts (MORB), ocean island basalts (OIB), large igneous provinces (LIP) and island arc basalts (ARC) are derived from Kamenetsky et al. (2001). Symbols: cross = chromite in chromitite; diamond = chromite in melatroctolite; square = chromite in dunite

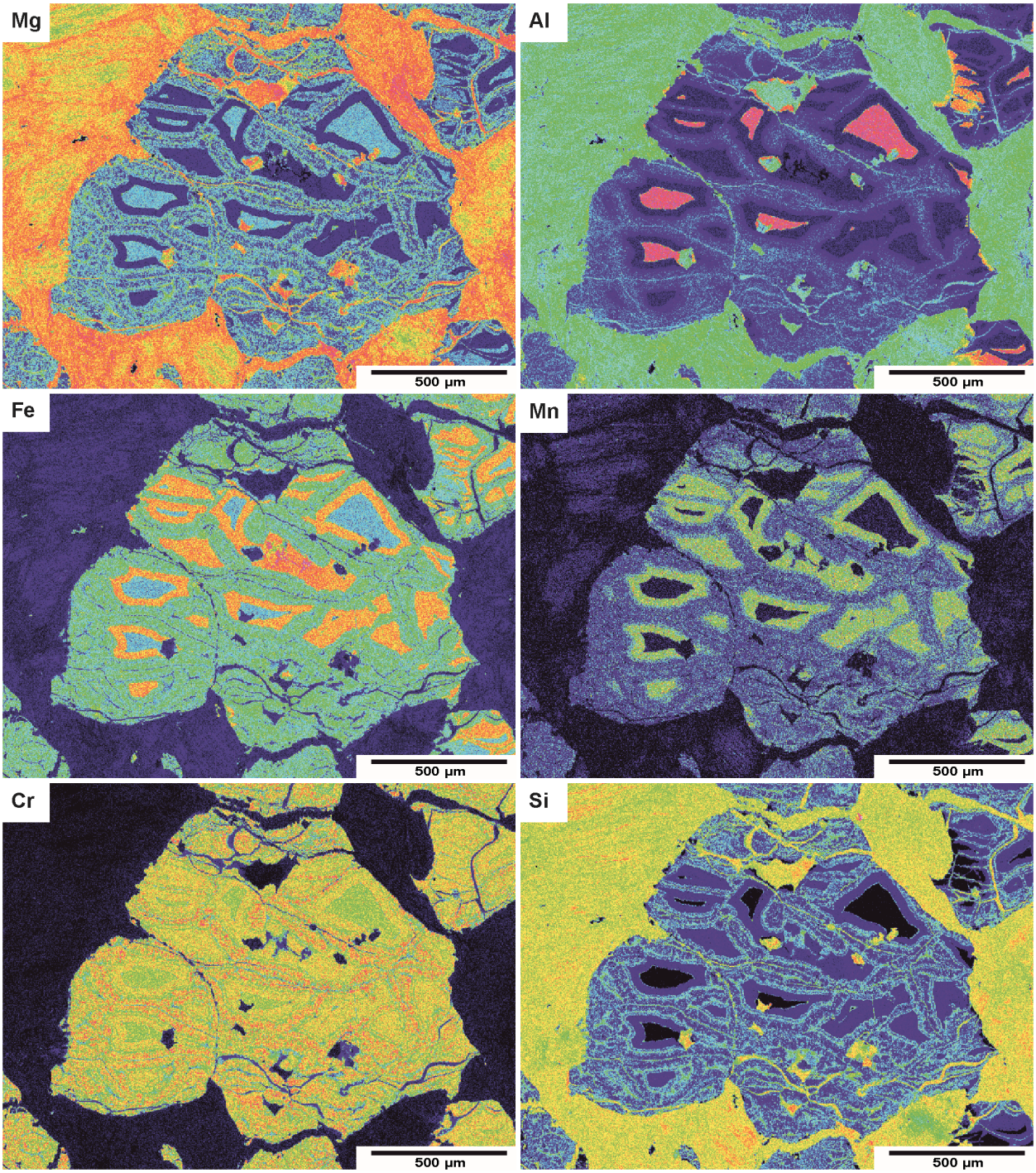

Fig. 27 X-ray element-distribution maps on an altered chromite from a chromitite layer.

13.2.2. Sulphides

Electron microprobe analyses were carried out on the interstitial sulphide aggregates and some blebby inclusions within the chromite. Pyrrhotite from both types has similar compositions roughly corresponding to intermediate hexagonal pyrrhotite between the Fe_9S_{10} and $Fe_{11}S_{12}$ stoichiometry. Pyrrhotite shows variable contents of Co and Ni up to 0.25 and 1.15 wt%, respectively. Pentlandite displays compositional variations at the scale of individual samples, involving an irregular increase of the Ni/Fe ratio in the interstitial sulphide compared with the included blebs. This is interpreted as a result of the exposition of the interstitial aggregates to oxidizing conditions during serpentinization. Millerite has almost stoichiometric composition NiS with only minor substitution of Fe up to 2.40 wt%. Violarite composition was close to stoichiometric, with similar proportion of Fe and Ni and trace amounts of Co. Chalcopyrite analyses revealed almost stoichiometric composition. A selection of representative electron probe microanalyses on sulphides is given in Tab. 6.

Tab. 6 Representative electron probe microanalyses on sulphides (wt%).

Mineral	Pn	Pn	Pn	Po	Po	Po	Ccp	Ccp	Ccp	Ml	Ml	Vio	Vio
	incl	Int	int	incl	int	int	incl	int	int	int	int	int	int
Fe	29.78	27.77	29.89	58.86	60.69	61.00	29.69	31.45	31.97	1.87	0.87	27.42	24.98
Ni	35.50	37.72	37.81	0.48	0.48	0.41	0.29	0.01	0.11	62.55	63.76	27.32	28.33
Co	0.39	0.68	0.90	0.00	0.17	0.10	<d.l.	0.08	0.07	0.38	0.46	0.70	0.31
Cu	<d.l.	0.13	0.03	0.29	0.05	0.03	34.06	34.87	35.41	<d.l.	<d.l.	0.69	3.06
Zn	<d.l.	<d.l.	<d.l.	0.01	0.13	0.07	<d.l.	0.03	0.17	<d.l.	<d.l.	<d.l.	<d.l.
As	0.06	0.05	<d.l.	<d.l.	0.05	<d.l.	0.09	<d.l.	<d.l.	<d.l.	<d.l.	0.05	0.02
S	33.32	34.66	33.22	39.60	38.89	39.38	35.13	34.67	35.12	34.65	34.17	40.19	40.39
Total	99.05	101.02	101.86	99.24	100.46	101.00	99.26	101.10	102.85	99.45	99.25	96.36	97.08

<d.l., below detection limit; incl, inclusion; int, interstitial; Ccp, chalcopyrite; Ml, millerite; Pn, pentlandite; Po, pyrrhotite; Vio, violarite

13.2.3. Silicates

Amphiboles are the most abundant inclusions in the massive chromitite and the accessory chromite disseminated in the serpentinized dunite. They pertain to the Ca-amphibole group, with Mg# that range between 0.88 and 0.91. The Na contents are relatively high between 2.81 and 5.17 wt% NaO (Tab. 7). The olivine inclusions have a rather constant composition (Fo_{89-90}) and are characterised by Ni and Ca contents between 0.27 and 0.3 wt% NiO, and 0.04 and 0.07 wt% CaO, respectively. The olivine inclusions do not differ substantially from olivine relics in melatroctolites, having Fo_{87-88} composition and similar contents in NiO and CaO (Tab. 7). Both, diopside (En_{41-43}) and enstatite (En_{85-89}) inclusions (Fig. 28) contain significant Cr and Al (Tab. 7). The poikilitic clinopyroxenes in the melatroctolites are characterized by En_{46-49} (diopside) and En_{62-66} (augite), as shown in Fig. 29.

Tab. 7 Representative electron probe microanalyses on silicates (wt%).

Mineral	Ol	Ol	Ol	Ol	Di	Di	Di	Aug	Aug	En	En	Prg	Prg	Prg
Rock type	Du	Du	Mtr	Mtr	Du	Mtr	Mtr	Mtr	Mtr	Chr	Chr	Chr	Chr	Du
	incl	incl	int	int	incl	int	int	int	int	incl	incl	incl	incl	incl
SiO_2	41.34	41.08	40.82	41.29	53.06	53.77	51.89	58.36	43.95	57.81	56,00	44.19	43.85	43.56
TiO_2	0.02	0.04	0.04	<d.l.	0.59	0.45	0.64	<d.l.	3.15	0.24	0.18	3.30	2.70	3.32
Al_2O_3	0.04	<d.l.	<d.l.	<d.l.	3.12	2.3	4.09	0.19	12.31	1.46	2.11	12.39	12.36	12.44
Cr_2O_3	0.54	0.51	<d.l.	<d.l.	1.42	0.03	0.08	0.12	0.05	0.75	1.09	2.33	2.17	2.61
CaO	0.06	0.05	0.04	0.03	21.62	22.78	21.68	13.32	11.46	0.23	0.33	10.68	10.97	11.13
MgO	50.42	49.7	47.9	48,00	15.21	16.96	16.07	21.59	17.10	33.39	34.50	17.76	18.06	16.51
FeO	8.13	8.55	11.45	11.80	2.69	3.26	3.47	4.79	5.42	5.88	5.68	3.43	3.49	4.17
MnO	0.19	0.19	0.20	0.22	0.04	0.10	0.11	0.09	0.07	0.17	0.16	0.07	0.10	0.06
NiO	0.27	0.32	0.24	0.22	<d.l.	0.04	0.06	0.04	0.06	0.08	0.10	0.11	0.10	0.10
K_2O	<d.l.	<d.l.	<d.l.	<d.l.	<d.l.	<d.l.	<d.l.	<d.l.	0.13	<d.l.	<d.l.	0.05	0.04	<d.l.
Na_2O	0.05	<d.l.	0.01	<d.l.	1.47	0.41	0.60	0.03	2.95	<d.l.	0.01	3.13	3.08	4.19
Total	101.06	100.44	100.7	101.56	99.22	100.1	98.69	98.53	96.65	100.01	100.16	97.44	96.92	98.09

<d.l., below detection limit; Aug, augite; Chr, chromitite; Di, diopside; Du, dunite; En, enstatite; incl, inclusion; int, interstitial; Mtr, melatroctolite; Ol, olivine; Prg, pargasite

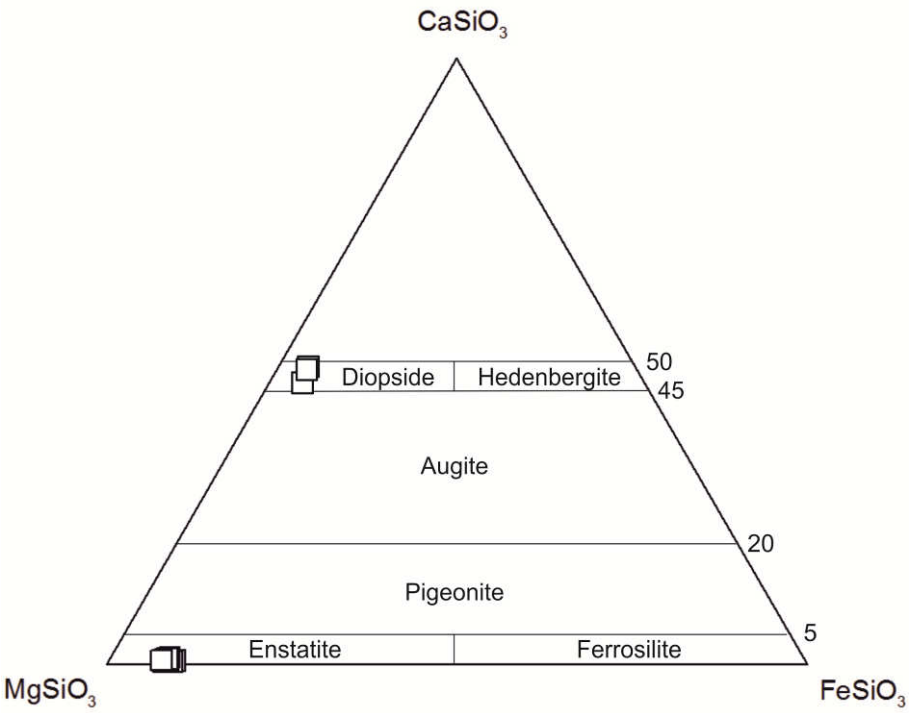

Fig. 28 Chemical composition of pyroxene inclusions in chromite.

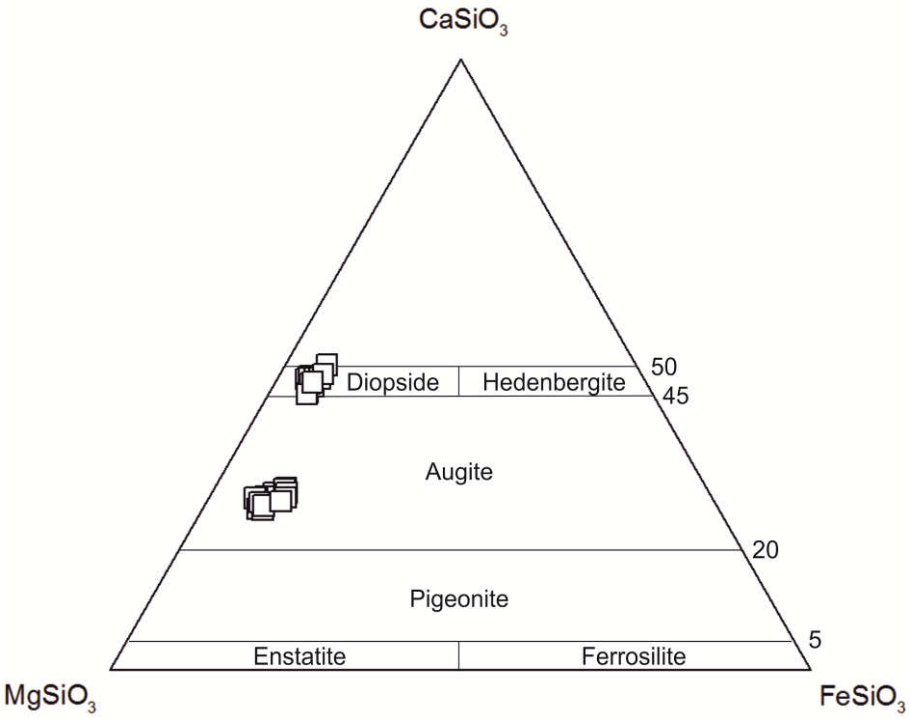

Fig. 29 Chemical ompositions of poikilitic pyroxene associated with melatroctolite.

13.3. Platinum-group element geochemistry

Results of bulk-rock PGE, Au, and S analyses indicate very low PGE contents between 12 and 69 ppb in the chromitites, as well as 22 and 83 ppb in the melatroctolites (Tab. 8). Total sulphur concentrations in the chromitites and melatroctolites vary between 200-5600 ppm and 200-8350 ppm, respectively. The melatroctolites have substantially higher Au-concentrations compared to chromitites with values up to 59 ppb. One sample of serpentinized dunite was found to contain 14 ppb total PGE, 2.5 ppb Au and 1600 ppm S. Chondrite-normalized PGE spidergrams (Fig. 30a, Fig. 30b) are very similar in all types of analyzed rocks, having a deep negative anomaly in Ir, and a sharp positive slope, with remarkable enrichment of the PPGE (Pt, Pd, Rh) over the IPGE (Os, Ir, Ru). These patterns differ from those commonly observed in mantle hosted podiform chromitites that display a typical negative slope with the IPGE prevailing over PPGE. The PGE trends of the Bracco chromitites exhibit some similarities with typical trends of stratiform chromitites, except for the absence of the Rh positive anomaly and for the lower total PGE concentrations.

Total PGE concentrations do not correlate with S contents (Fig. 31a). However, there is a positive correlation between the PPGE/IPGE ratio and the S concentration ($R = 0.61$), suggesting that the PPGE contents, in both chromitites and melatroctolites, are mainly controlled by the sulphide phases (Fig. 31b). Accordingly, low PGE concentrations of Pt, Pd and Rh (Tab. 9) were detected in the sulphides associated to the chromitites from Cima Stronzi. Pt was the most abundant PGE with concentrations up to 600 ppm in pentlandite and millerite, as well as 400 ppm in pyrrhotite. Maximum Pd and Rh concentrations were detected in pyrrhotite with 120 ppm and 100 ppm, respectively. The IPGE (Os, Ir, Ru) were systematically absent.

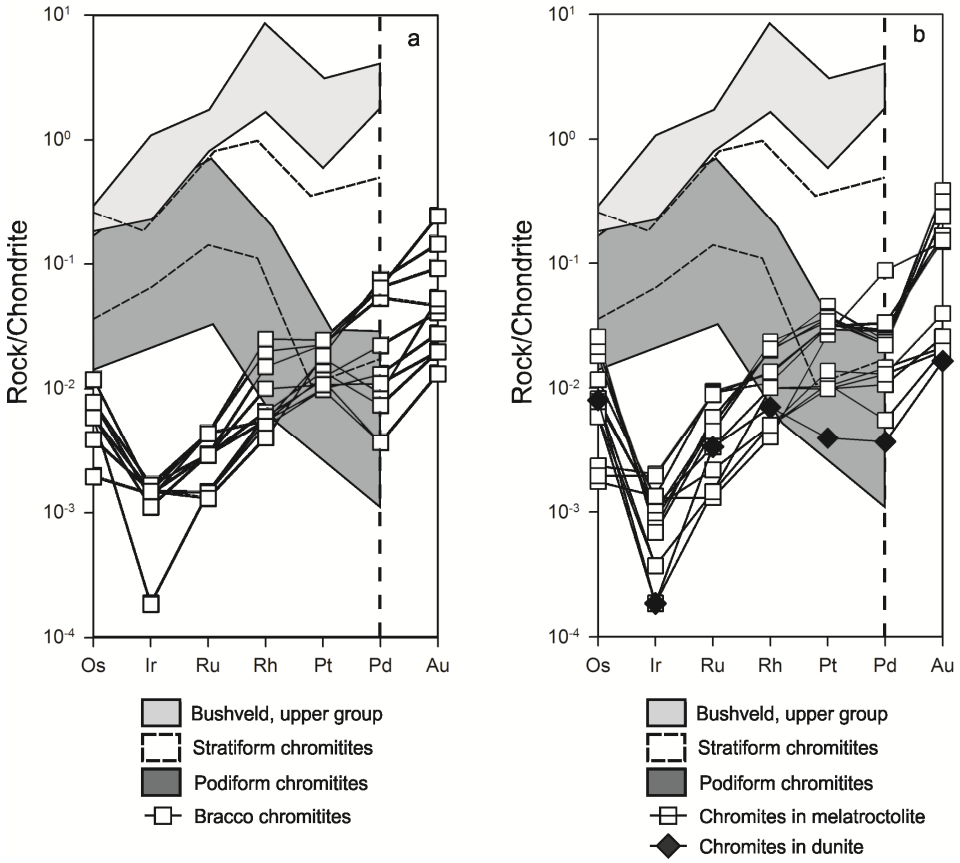

Fig. 30 a,b Chondrite normalized PGE patterns for chromitites (a) as well as for dunites and melatroctolites (b). Normalized values were calculated after Naldrett & Duke (1980). The fields for stratiform and podiform chromitites are from Cawthorn (1999) and Zaccarini et al. (2011).

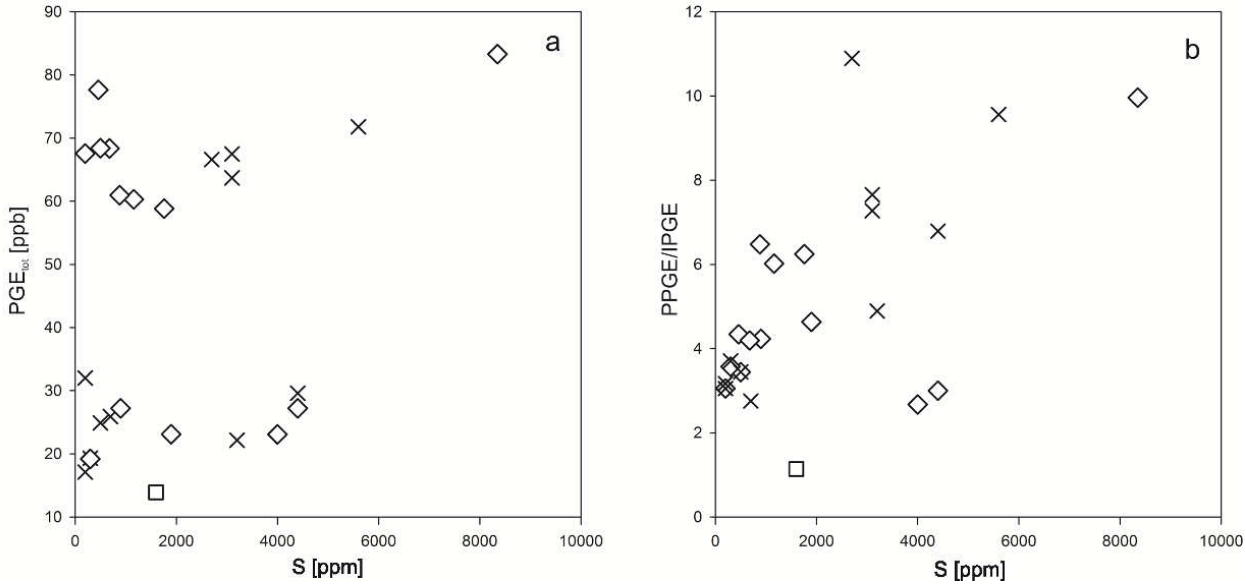

Fig. 31 a,b Whole rock PGE vs. S (a) and PPGE/IPGE vs. S (b) for chromitites, dunites and melatroctolites. Symbols: cross = chromitite; diamond = melatroctolite; square = dunite

Tab. 8 Whole rock PGE, Au and S concentrations. Results are given in ppb, except sulphur (ppm).

Locality	Rock type	Os	Ir	Ru	Rh	Pt	Pd	PGE_{tot}	Au	S
SR	Du	4.1	0.1	2.3	1.4	4.0	2.0	13.9	2.5	1600
SR	Chr	<d.l.	0.8	<d.l.	1.1	12.6	12.1	26.6	6.2	4400
SR	Chr	<d.l.	0.8	2.0	1.1	10.2	7.1	21.2	4.2	3200
SR	Chr	4.0	0.7	3.0	4.0	23.0	29.0	63.7	7.0	3100
SR	Chr	<d.l.	0.6	2.0	3.0	23.0	35.0	63.6	14.0	2700
ZN	Chr	4.0	0.9	3.0	1.1	18.0	5.0	32.0	8.0	200
ZN	Chr	<d.l.	0.6	2.0	1.3	14.0	4.0	21.9	3.0	500
ZN	Chr	<d.l.	0.1	<d.l.	1.2	12.0	2.0	15.3	2.0	300
ZN	Chr	<d.l.	0.1	<d.l.	<d.l.	10.0	2.0	12.1	2.0	200
PM	Chr	<d.l.	0.2	<d.l.	<d.l.	11.0	3.0	14.2	3.0	300
PM	Chr	6.1	0.8	<d.l.	<d.l.	18.7	40.2	65.8	21.9	3100
PM	Chr	4.0	0.9	2.0	2.0	11.0	6.0	25.9	3.0	700
CN	Chr	<d.l.	0.8	3.0	5.0	25.0	35.0	68.8	37.0	5600
SR	Mtr	3.9	0.6	2.3	2.0	10.5	7.9	27.2	3.2	4400
SR	Mtr	4.2	0.6	1.5	<d.l.	10.0	5.8	22.1	3.9	4000
ZN	Mtr	6.0	0.7	0.9	<d.l.	27.3	47.6	82.5	22.5	8350
CN	Mtr	<d.l.	0.7	6.5	2.6	32.1	16.0	57.9	23.8	1760
CN	Mtr	<d.l.	1.1	6.3	2.2	31.6	17.9	59.1	25.1	1160
CN	Mtr	<d.l.	1.1	6.1	2.7	32.0	18.1	60.0	23.1	880
MT	Mtr	<d.l.	0.1	<d.l.	2.0	10.0	7.0	19.1	6.0	1900
MT	Mtr	4.0	0.2	<d.l.	<d.l.	14.0	7.0	25.2	3.0	900
MT	Mtr	10.5	0.5	3.5	4.1	45.9	13.1	77.6	58.3	460
MT	Mtr	9.3	0.5	3.4	4.7	37.9	12.6	68.4	58.9	680
MT	Mtr	11.0	0.4	4.0	4.0	37.0	12.0	68.4	36.0	500
MT	Mtr	13.2	0.4	3.1	4.1	34.8	12.0	67.6	47.9	200

Chr, chromitite; CN, Canegreca; Du, dunite; MT, Mattarana; Mtr, melatroctolite; PM, Pian della Madonna; SR, Cima Stronzi; ZN, Ziona

Tab. 9 PPGE concentrations in selected sulphides associated with the Cima Stronzi chromitites.

Mineral	Pn	Pn	Pn	Pn	Pn	Pn	Po	Po	Po	Po	Po	Ml	Ml	Ml
Pt	<d.l.	<d.l.	0.049	0.060	0.035	0.031	0.017	0.023	0.025	0.040	0.031	0.015	0.018	0.048
Pd	0.008	0.007	0.004	<d.l.	<d.l.	0.012	0.007	<d.l.	<d.l.	0.009	0.012	<d.l.	<d.l.	0.005
Rh	<d.l.	0.004	<d.l.	<d.l.	0.004	<d.l.	<d.l.	0.003	<d.l.	0.008	<d.l.	<d.l.	<d.l.	<d.l.
$PPGE_{tot}$	0.008	0.012	0.053	0.060	0.039	0.043	0.024	0.026	0.025	0.057	0.043	0.015	0.018	0.053

Ml, millerite; Pn, pentlandite; Po, pyrrhotite

14. GEOTHERMOBAROMETRICAL CALCULATIONS

Temperatures for chromitites were calculated on the basis of orthopyroxene inclusions in the chromites using the orthopyroxene-spinel Fe-Mg thermometry proposed by Liermann and Ganguly (2003, 2007). Calculations on almost 20 orthopyroxene-spinel pairs from the Cima Stronzi and Ziona occurrences, at an assumed pressure of 0.8 GPa, yield temperatures of 970-890 °C and 890-820 °C, respectively (Tab. 8).

Some olivine inclusions were observed in disseminated chromites within the serpentinized dunites from Cima Stronzi. Temperatures were calculated based on the olivine-spinel Fe-Mg geothermometer of Jianping et al. (1995), which is an adapted version of the thermometer developed by Fabries (1979). Five olivine-spinel pairs revealed temperatures between 900 and 820 °C. The olivine-spinel Fe-Mg geothermometer proposed by Ballhaus et al. (1991) represents a revised version of the thermometer of O'Neill and Wall (1987). Calculated temperatures, at an assumed pressure of 0.8 GPa, are in the range of 930-860 °C (Tab. 9). However, possible subsolidus re-equilibration down to temperatures of 500 °C influences the Fe-Mg distribution between chromite and olivine (Lehmann 1983). Therefore, calculated temperatures may not reflect primary magmatic conditions, representing the possible closure of the Fe-Mg exchange reaction between olivine and chromite. Ballhaus et al. (1991) developed an olivine-spinel oxygen barometer which offers the possibility to study the oxidation state of the upper mantle based on the redox ratio Fe3+/ΣFe. Oxygen fugacities, obtained on disseminated chromites from the serpentinized dunites, fall between the QFM- and the MH-buffer with $\Delta \log fO_2$ at +2.0-2.4 units above QFM. The samples investigated in this study are characterized by an oxidation state between that of chromitites from ophiolites and Ural-Alaskan type complexes at a relatively low temperature (Fig. 32).

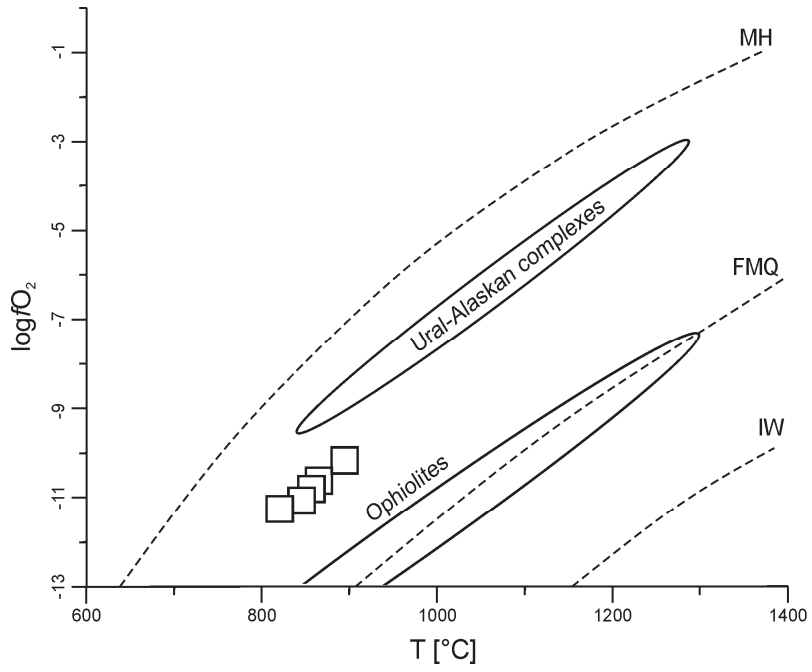

Fig. 32 Results of the olivine-spinel oxygen barometry in the plot T-$\Delta \log fO_2$ (redrawn after Garuti et al. 2003).

Tab. 10 Geothermometrical calculations on orthopyroxene inclusions in chromite.

Enstatite	SR39-1	SR39-2	SR39-3	SR39-4	SR39-5	SR39-6	SR40-1	SR40-2	SR40-3	ZN15-1	ZN15-2	ZN15-3	ZN15-4	ZN15-5	ZN15-6	ZN15-7
Chromite	SR39-1	SR39-15	SR39-14	SR39-17	SR39-20	SR39-24	SR40A-2	SR40A-4	SR40A-8	ZN15-1	ZN15-3	ZN15-5	ZN15-6	ZN15-8	ZN15-13	ZN15-12
X_{Al}^{Opx}	0,02	0,02	0,02	0,02	0,01	0,02	0,02	0,02	0,02	0,01	0,01	0,01	0,01	0,01	0,01	0,01
X_{cr}^{Sp}	0,46	0,42	0,43	0,49	0,45	0,45	0,42	0,43	0,42	0,45	0,46	0,46	0,46	0,47	0,45	0,44
$K_D^{[Fe/Mg]}$	4,82	4,65	4,95	5,34	4,73	4,67	4,30	4,52	4,42	5,89	5,84	5,50	5,57	5,86	5,17	5,47
Orthopyroxene-spinel thermometry (Liermann and Ganguly 2003, 2007)																
T [K]	1212,77	1187,28	1164,13	1184,60	1208,68	1216,35	1239,12	1210,39	1212,67	1097,60	1103,24	1141,55	1125,64	1111,52	1158,85	1124,52
T [°C]	939,62	914,13	890,98	911,45	935,53	943,20	965,97	937,24	939,52	824,45	830,09	868,40	852,49	838,37	885,70	851,37

SR, Cima Stronzi; ZN, Ziona

Tab. 11 Geothermobarometrical calculations on olivine inclusions in chromite.

Olivine	SR32-1	SR32-2	SR32-3	SR32-4	SR33-1
Chromite	SR32-8	SR32-9	SR32-10	SR32-12	SR33-3
Ti	0,03	0,03	0,02	0,03	0,03
Mg^{Ol}	0,92	0,92	0,92	0,91	0,93
Fe^{Ol}	0,08	0,08	0,08	0,09	0,07
Mg^{Sp}	0,67	0,66	0,65	0,65	0,64
$Fe^{2+\ Sp}$	0,33	0,34	0,35	0,35	0,36
Cr^{Sp}	0,43	0,43	0,43	0,41	0,45
$K_{D\ [Fe/Mg]}$	5,40	5,72	6,08	5,68	6,86
Olivine-spinel thermometry (Jianping et al. 1995)					
T [K]	1168,66	1139,16	1119,12	1130,54	1094,04
T [°C]	895,51	866,01	845,97	857,39	820,89
Olivine-spinel thermometry (O'Neill and Wall 1987)					
T [K]	1169,61	1140,13	1105,82	1140,79	1100,82
T [°C]	896,46	866,98	832,67	867,64	827,67
Olivine-spinel thermometry (Ballhaus et al. 1991)					
T [K]	1202,66	1173,37	1137,35	1174,56	1129,93
T [°C]	929,51	900,22	864,20	901,41	856,78
Oxygen barometry (Ballhaus et al. 1991)					
$\Delta \log f O_2$	2,04	2,13	2,06	2,11	2,37

SR, Cima Stronzi

15. PARENTAL MELT COMPOSITIONS

The chemical composition of chromite is sensitive to the bulk chemistry of the melt from which it crystallizes. Therefore, Al_2O_3 and TiO_2 contents in the parental melt, as well as the FeO/MgO ratio were calculated based on the equations of Maurel and Maurel (1982) in (8) and Rollinson (2008) in (9-10). The chromitites and the disseminated chromites in the dunite appear to have been in equilibrium with melts characterized by 14.4-16.7 w% Al_2O_3 and TiO_2 in the range of 0.84-1.41 wt% (Fig. 33). Calculated melt values are consistent with compositions of MORB-type magmas, in agreement with the Al_2O_3-TiO_2 relationships of the Bracco chromites presented in Fig. 4c.

The calculated FeO/MgO ratios, calculated after Maurel (1984, cited in Augé 1987) in (11), are in the ranges 0.66-1.73 (av. = 1.19) and 0.8-0.9 (av. = 0.86) for the chromitites and accessory chromites in dunites, respectively. Some post-magmatic adjustment of the Fe/Mg ratio might have occurred in the dunites because of the high olivine/chromite volume ratio. However, this is not expected to have occurred in the massive chromitite, in which chromite Fe/Mg ratio should still reflect the composition of the parental melt.

(8) $$Al_2O_3^{melt} = \frac{0.035}{Al_2O_3^{spinel}}$$

(9.1) $$Al_2O_3^{melt} = 5.2181 \cdot \ln(Al_2O_3^{spinel}) - 1{,}0505 \quad (ARC)$$

(9.2) $$Al_2O_3^{melt} = 7.1518 \cdot \ln(Al_2O_3^{spinel})^{0{,}2387} \quad (MORB)$$

(10.1) $$TiO_2^{melt} = 1.0963 \cdot (TiO_2^{spinel})^{0{,}7863} \quad (ARC)$$

(10.2) $$TiO_2^{melt} = 1.5907 \cdot (TiO_2^{spinel})^{0{,}6322} \quad (MORB)$$

(11) $$\ln\left(\frac{FeO}{MgO}\right)_{melt} = \ln\left(\frac{FeO}{MgO}\right)_{spinel} - 0.47 + 1.07 \cdot X_{Al} - 0.64 \cdot X_{Fe^{3+}}$$

$$X_{Al} = \frac{Cr}{Cr + Al + Fe^{3+}} \qquad X_{Fe^{3+}} = \frac{Cr}{Cr + Al + Fe^{3+}}$$

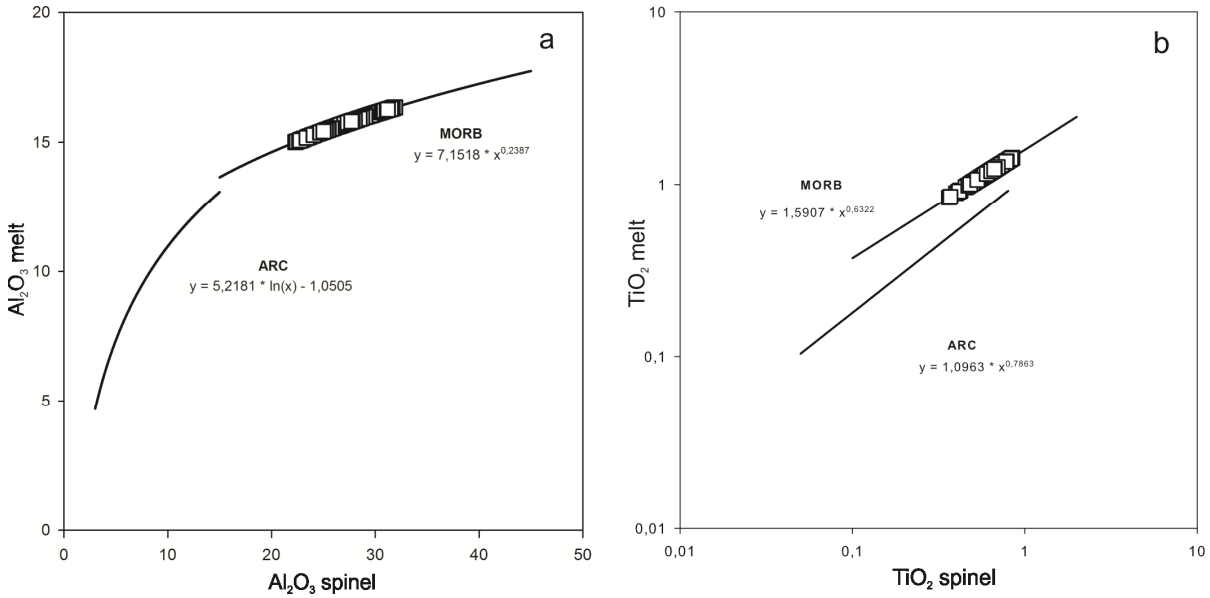

Fig. 33 a,b Calculated Al_2O_3 (a) and TiO_2 (b) contents in chromite parental melts. Regression lines for MORB and ARC lavas are derived from Rollinson (2008).

16. DISCUSSION AND CONCLUSIONS

The Bracco Gabbro Complex, as part of the Ligurian ophiolites (Northern Apennine, Italy) has undergone extensive low-grade metamorphic alteration under sub-oceanic conditions that has transformed the igneous rocks (gabbros, troctolite, melatroctolite and peridotite) into prehnite-pumpellyite facies assemblages. Apart of rare relics of the primary silicate assemblage (mainly olivine pyroxenes), small partially altered chromitite bodies and rare primary inclusions in fresh chromite appear to be the only preserved phases. Geothermobarometrical data, based on chromite-orthopyroxene and chromite-olivine phase relations, indicate equilibration at temperatures between 970 and 820°C, under relatively high oxygen fugacity above the FMQ buffer.

16.1. Constraints to the origin of the Bracco chromitites

The Bracco chromitites distinguish from podiform chromitite hosted in the mantle-tectonite of ophiolite complexes because of their different lithological association and chromite mineral chemistry (Leblanc and Nicolas 1992). Actually, they associate with predominant gabbroic rocks and shear some structural and chemical features (stratiform morphology, high Al_2O_3, TiO_2 and Fe_2O_3) with stratiform chromitites in supra-Moho cumulate sequences of ophiolites and continental layered intrusions of the Bushveld types. However, the geological setting of the Bracco complex does not compare with either supra-Moho cumulates in ophiolites or layered intrusions in continental cratons. According to old and recent genetic models, it represents a layered gabbroic body intruding subcontinental mantle lherzolites in an ascent spreading centre, before opening of the Piedmont-Ligurian Ocean (Lemoine et al. 1987; Piccardo et al. 2002; Piccardo and Guarneri 2011). Field relationships and textures of the Bracco chromitites observed in this study are consistent with the interpretation given by previous authors that the chromitites resulted from rhythmic accumulation of small amounts of chromite, during formation of the mafic-ultramafic layered zone at the base of the Bracco magma chamber (Bezzi and Piccardo 1970 1971; Cortesogno et al. 1987). It has been proposed that stratiform chromitites set concordant with their igneous layered host-rocks, may formed by mixing of newly injected primitive melt with a more evolved residual liquid resident in the magma chamber (Irvine 1977). The objection raised that precipitation of extensive chromitite layers (e.g. Bushveld-type deposits) would require mixing of unrealistically large volumes of magma (Cawthorn and Walraven 1998). However, that does not apply to the case of the Bracco intrusion, where the volume of produced chromitite is negligible compared with the volume of the intrusion. Thus, it can be assumed that a magma mixing genetic model is not unrealistic for the Bracco chromitites. Fresh mafic magma, having olivine, orthopyroxene and chromite on the liquidus, was repeatedly injected in the magma chamber and reacted with the resident, more evolved residual melt. The composition of the hybrid melt was thereby shifted in the stability field of chromite as the only crystallizing phase.

As modelled by Ferreira Filho et al. (1995) and Naldrett et al. (2009), magma mixing would also account for the appearance of an immiscible sulphide liquid during chromite precipitation that is testified by the

numerous blebby inclusions of sulphide observed in almost all of the studied samples (chromitite, melatroctolite, troctolite). The predominant Fe-Ni-Cu assemblage of the blebs is consistent with on-cooling equilibration of a magmatic sulphide liquid, although, the blebs might have loose some Fe by diffusion towards the enclosing chromite (Naldrett and Lehmann 1988). The large sulphide aggregates, occurring interstitial to chromitite and in their host rocks, indicate that the melt continued to segregate an immiscible sulphide liquid after the chromitite precipitiation.

16.2. Significance of the PGE distribution

Podiform and stratiform chromitites are usually enriched in PGE compared to their host rocks. In particular, the podiform chromitite, with few exceptions, are enriched in IPGE. Therefore, their chondrite normalized PGE spidergrams show a negative slope (e.g. Economou-Eliopoulos 1996; Melcher et al. 1999; Ahmed and Arai 2002). However, few examples of podiform chromitites hosted in the ophiolitic mantle (e.g. Çina et al. 2002; Escayola et al. 2011) and a number of stratiform chromitites, including the Upper Group of the Bushveld Complex (e.g. Von Gruenewaldt and Merkle 1995) display PGE positive patterns due to the predominance of PPGE over IPGE. Consistently with these two different PGE patterns, the dominant PGM in the podiform chromitite are IPGE phases, such as sulphides of the laurite-erlichmanite series, alloys in the Ru-Os-Ir system and less abundant sulpharsenides, such as irarsite (e.g. Melcher et al. 1997; Garuti et al. 1999; Malitch et al. 2003; Kapsiotis et al. 2011). These PGM generally occur as small inclusions (< 10 μm) in chromite or may partition into chromite as solid solution (Righter 2001). In the chromitites, characterized by the positive PGE patterns, two different groups of PGM have been described. The first group consists of IPGE minerals that mostly occur included in chromite. The second group is composed of PPGE minerals that generally are related to the presence of abundant sulphides in the silicate matrix of the chromitite, indicating the importance of sulphur as a collector for PPGE (Peck and Keays 1990).

The case of Bracco is rather unique because chromitites are not significantly enriched in PGE compared to their host dunite and melatroctolite. All rocks are characterized by similar concentrations and positive distribution patterns of PGE (Fig. 30). Detailed mineralogical investigation failed to locate any discrete PGM inclusion in chromite. However, the low PPGE contents detected in sulphides suggest that the PPGE are most likely hosted in the sulphides as solid solution. The broad positive correlation between bulk-rock S and the PPGE/IPGE (Fig. 31b) ratio supports the contention that the PGE distribution is a function of the original sulphide content of the igneous rocks (Naldrett and Von Gruenewaldt 1989). This fact implies that the immiscible sulphide liquid preferentially concentrated PPGE with respect to the refractory IPGE. The fact that the IPGE, and in particular Ir, are strongly depleted in the Bracco ultramafic rocks may indicate that Os, Ru and mostly Ir were left behind in the mantle source during partial melting, or were winnowed out of the magma before its emplacement. The first hypothesis is preferred because it would be consistent with generation of the Bracco parental magma by low degrees of

partial melting. According to MacLean (1969), Barnes (1985) and Keays (1995) a relatively large degree of partial melting, up to 30%, is required to extract the PGE from the mantle source. Piccardo and Guarnieri (2010) demonstrated that the melts responsible for the formation of gabbroic intrusions of the Bracco type formed by relatively low degrees (4-7%) of partial melting of an asthenospheric mantle source. This low degree of partial melting was obviously not high enough to remove all the PGE from the mantle, especially the IPGE. Only the most incompatible elements, such as sulphur and parts of the PPGE, were partially removed from the mantle and concentrated in the melt. Therefore, it is concluded that low degree of partial melting of the mantle source was the main factor to control the unusual PGE distribution in the Bracco chromitites.

16.3. Nature of the parental magma of the Bracco-Gabbro Complex

According to Piccardo and Guarnieri (2011), gabbro-norite cumulates intruding ophiolitic peridotite in the Jurassic Piedmont-Ligurian basin derived from MORB-type melts whose original composition was modified by reaction with a lithospheric mantle protoliths, during ascent towards shallow upper mantle levels. Calculated melt compositions in equilibrium with the Bracco chromitites and associated dunite are characterized by 14.4-16.7 wt% Al_2O_3, TiO_2 contents in the range from 0.84-1.41 wt%, and average FeO/MgO ratios evolving from 1.19 (i.e. crystallisation of chromite). These values roughly correspond to those calculated for supra-Moho cumulus chromitites in the Ural ophiolites which are believed to have crystallized in equilibrium with MORB-type melts (Garuti et al. 2012). Consistently, the S-saturation and the PGE-depleted state of the melt parental to the Bracco chromitites are features commonly observed in high-Al_2O_3 chromitites derived from MORB-type magmas (Zhou et al. 1998).

The suite of solid inclusions reported from the Bracco chromitite indicates that one of the mixing magmas had relatively high water activity and carried some incompatible elements such as Na, K, Zr, Ti. In particular, Zr-bearing and REE-poor loveringite and baddeleyite have been described as “exotic” minerals in ophiolitic chromitites (Cabella et al. 1997; Renna and Tribuzio 2011). As a matter of fact, the presence of fluids enriched in Na and other incompatible elements has been reported as a common feature during formation of ophiolitic chromitites (Johan et al. 1983), and the occurrence of Zr-bearing phases (baddeleyite, zirconolite) has been reported from gabbro-hosted high-Al_2O_3 chromitites in ophiolites of Cuba (Zaccarini and Proenza 2005). Although, the possibility of fluid metasomatism during formation of the Bracco chromitites cannot be excluded in principle (Cabella et al. 1997), we suggest that enrichment in Zr could have occurred in the residual melt resident in the Bracco magma chamber as a result of extreme fractional differentiation.

Considering the Al_2O_3, TiO_2, FeO/MgO and Fe_2O_3 composition of the Bracco chromitites, a certain similarity with supra-Moho stratiform chromitites from subduction-unrelated Continental-margin type ophiolites of the Urals can be noted (Garuti et al. 2012).

16.4. Chromite alteration

The analyzed ferrian chromite rims of the Bracco chromitites, corresponding to the first stage alteration (Fig. 12a), have Mg# values between 0.22 and 0.41, as typical for high grade metamorphic conditions, i.e. amphibolite facies conditions. The second stage alteration of the chromite and the presence of abundant prehnite, intercumulus phases in the chromitites and the troctolites, are indicative of low-grade metamorphism. It is concluded that the metamorphic overprints registered by the investigated rocks are consistent with the retrograde tectono-metamorphic evolution of the Internal Ligurides, as proposed by several authors (Cortesogno et al. 1975 1987). In particular, the metamorphic evolution of the Bracco chromitites, dunites and melatroctolites started during the uplift of the subcontinental asthenospheric mantle (upper amphibolite to greenschist facies metamorphic conditions) in an extensional regime and ended with its final exposure to the seafloor and concomitant serpentinization (low-grade metamorphism).

17. REFERENCES

Ahmed AH, Arai AS (2002) Unexpectedly high PGE chromitite from the deeper mantle section of the northern Oman ophiolite and its tectonic implications. Contrib Mineral Petrol 143:263-278

Apopei, A.I., Buzgar N., 2010: The Raman study of amphiboles. Anal Şt Univ "Al. I. Cuza" Iaşi, Geologie, LVI/1 (available online).

Arai S (1992) Chemistry of chromian spinel in volcanic rocks as a potential guide to magma chemistry. Mineral Mag 56:173-184

Arai S (1997) Control of wall-rock composition on the formation of podiform chromitites as a result of magma/peridotite interaction. Resour Geol 47:177-187

Arai S, Uesugi J, Ahmed AH (2004) Upper crustal podiform chromitite from the northern Oman ophiolite as the stratigraphically shallowest chromitite in ophiolite and its implication for Cr concentration. Contrib Mineral Petrol 147:145-154

Augé T (1987) Chromite deposits in the northwestern Oman ophiolite: mineralogical constraints. Miner Depos 22:1-10

Bach W, Früh-Green GL (2010) Alteration of the Oceanic Lithosphere and Implications for Seafloor Processes. Elements 6:173-178

Ballhaus C, Berry RF, Green DH (1991) High pressure experimental calibration of the olivine – orthopyroxene–spinel oxygen geobarometer: implications for the oxidation of the mantle. Contrib Mineral Petrol 107:27-40

Barnes SJ (2000) Chromite in Komatiites, II. Modification during greenschist to mid-amphibolite facies metamorphism. J Petrol 41:387–409

Barnes SJ, Naldrett AJ, Gorton MP (1985) The origin of the fractionation of the platinum-group elements in terrestrial magmas. Chem Geol 53:303-323

Barnes SJ, Roeder PL (2001) The range of spinel composition in terrestrial Mafic and Ultramafic Rocks. Contrib Mineral Petrol 42:2279-2302

Barrett JJ, Spooner EFC (1977) Ophiolitic breccias associated with allochthonous oceanic crustal rocks in the East Ligurian Apennines, Italy - A comparison with observations from rifted oceanic ridges. Earth Planet Sci Lett 35:79-91

Beeson MH, Jackson EJ (1969) Chemical composition of altered chromites from the Stillwater Complex, Montana. Am Mineral 54:1084-1100.

Bezzi A, Piccardo GB (1970) Studi petrografici sulle formazioni ofiolitiche della Liguria. Riflessioni sulla genesi dei complessi ofiolitici in ambiente appenninico e alpino. Rend Soc It Mineral Petrol 26:1-42

Bezzi A, Piccardo GB (1971) Structural features of the Ligurian ophiolites: petrologic evidence for the "oceanic" floor of northern Apennines geosyncline. Mem Soc Geol It 10:53-63

Bowles JFW, Howie RA, Vaughan DJ, Zussmann J (2011) Rock-forming Minerals, Volume 5A, Non-silicates: Oxides, Hydroxides and Sulphides, 2nd edition. Geol Soc, London.

Brigo L, Ferrario A (1974) Le mineralizzazioni nelle ofioliti della Liguria Orientale. Rend Soc It Mineral Petrol 30:305-316

Buchanan DL, Noland J (1979) Solubility of sulphur and sulphide immiscibility in synthetic tholeitic melts and their relevance to Bushveld Coplex Rocks. Can Min 17:483-494

Bucher K, Grapes R (2011) Petrogenesis of metamorphic rocks, 8th edition. Springer, Berlin.

Buzatu A, Buzgar N (2010) The Raman study of single-chain silicates. Anal Şt Univ "Al. I. Cuza" Iaşi, Geologie, LVI/1:107-125

Cabella R, Garuti G, Oddone M, Zaccarini F (2002) Platinum-Group Element geochemistry in chromitite and related rocks of the Bracco gabbro complex (Ligurian Ophiolites, Italy). 9th Intern Platinum Symp, Abstract with Program, Billings, Montana, pp 69-72

Cabella R, Gazzotti M, Lucchetti G (1997). Loveringite and baddeleyite in layers of chromian spinel from the Bracco ophiolitic unit, Northern Apennines, Italy. Can Mineral 35:899-908

Cawthorn RG (1999) Geological models for platinum group metal mineralization in the Bushveld Complex. S Afr J Sci 95:490-498

Cawthorn RG, Walraven F (1998) Emplacement and crystallization time for the Bushveld Complex. J Petrol 39: 1669-1687

Çina A, Neziraj A, Karaj N, Johan Z, Ohnenstetter M (2002) PGE mineralization related to Albanian ophiolitic complex. Geol Carpat 53 (available online)

Cortesogno L, Galbiati B, Principi G (1981) Descrizione dettagliata di alcuni caratteristici affi oramenti di brecce serpentinitiche della Liguria orientale ed interpretazione in chiave geodinamica. Ofioliti 6:47-76

Cortesogno L, Galbiati B, Principi G (1987) Note alla "Carta geologica delle ofioliti del Bracco" e ricostruzione della paleogeografia Giurassico, Cretacica. Ofioliti 12:261-342

Cortesogno L, Lucchetti G, Penco AM (1975) Preorogenic metamorphic and tectonic evolution of the ophiolite mafic rocks (Northern Appenine and Tuscany). Rend Soc Ital Mineral Petrol 94:291-327

Decandia FA, Elter P (1972) La zona ofiolitifera del Bracco nel settore compreso fra Levanto e la Val Graveglia (Appennino Ligure). Mem Soc Geol It 11:503-530

Dewey JF, Pittman WC, Ryan WBF, Bonin J (1973) Plate-tectonics and the evolution of the alpine system. Bull Geol Soc Am 84:3137-3180

Dick HJB, Bullen T (1984) Chromian spinel as a petrogenetic indicator in abyssal and alpine-type peridotites and spatially associated lavas. Contrib Mineral Petrol 85:54-76

Dilek Y (2003) Ophiolite concept and its evolution. In: Dilek Y, Newcomb S (eds) Ophiolite concept and the evolution of geological thought. Spec Pap Geol Soc Am 373:1–16

Dilek Y, Furnes H (2011) Ophiolite genesis and global tectonics: Geochemical and tectonic fingerprinting of ancient oceanic lithosphere. Bull Geol Soc Am 123:387-411

Droop GTR (1987) A general equation for estimating Fe^{3+} in ferromagnesian silicates and oxides from microprobe analysis, using stoichiometric criteria. Mineral Mag 51:431-437

Economou Eliopoulos M (1996): Platinum group element distribution in chromite ores from ophiolite complexes: implications for their exploration. Ore Geol Rev 11:363 381

Escayola M, Garuti G, Zaccarini F, Proenza JA, Bedard J, Van Staal C (2011) Chromitite and platinum-group element mineralization at Middle Arm Brook, central Advocate ophiolite complex (Baie Verte peninsula, Newfoundland, Canada). Can Mineral 49:1523-1547

Fabries J (1979) Spinel-olivine geothermometry in peridotites from ultramafic complexes. Contrib Mineral Petrol 69:329-336

Ferrario A, Garuti G (1988) Platinum-Group Minerals in chromite-rich horizons of the Niquelândia Complex (Central Goiás, Brazil). In: Prichard HM, Potts PJ, Bowels JFW, Cribb SJ (eds) Proc Geo-Platinum 87 Symposium, Milton Keyes, Elsevier, pp 261-272

Naldrett AJ, Duke JM (1980) Platinum metals in magmatic sulphide ores. Science 208:1417-1424

Ferreira Filho CF, Naldrett AJ, Asif M (1995) Distribution of Platinum-Group Elements in the Niquelândia layered mafic-ultramafic intrusion, Brazil: Implications with respect to exploration. Can Mineral 33:165-184

Garuti G, Meloni S, Oddone M (2000) NAA of Platinum Group Elements and Gold in Reference Materials: A Comparison of Two Methods. J Radioanal Nucl Chem 245:17-23

Garuti G, Pushkarev EV, Thalhammer OAR, Zaccarini F (2012) Chromitites of the Urals (Part 1): Overview of chromite mineral chemistry and geo-tectonic setting. Ofioliti 37:27-53

Garuti G, Pushkarev EV, Zaccarini F, Cabella R, Anikina E (2003) Chromite composition and platinum-group mineral assemblage in the Uktus Uralian-Alaskan-type complex (Central Urals, Russia). Miner Depos 38:312-326

Garuti G, Zaccarini F, Moloshag V, Alimov V (1999) Platinum-Group Minerals as indicators of sulfur fugacity in ophiolitic upper mantle: an example from chromitites of the Ray-Iz ultramafic complex (Polar Urals, Russia). Can Mineral 37:1099-1116

Hill R, Roeder PL (1974) The crystallization of spinel from basaltic liquid as a function of oxygen fugacity. J Geol 82:709-729

Holwell DA (2010) A review of the behaviour of platinum group elements within natural magmatic sulfide ore systems. Plat Met Rev 54:26–36

Horninger G (1941) Beobachtungen am Erzinhalt von Gesteinen und an Chromerz aus Tampadel in Schlesien. Schweiz Mineral Petr Mitt 52:316-346

Huang E, Chen C, Huang T, Lin EH, Xu JA (2000) Raman spectroscopic characteristics of Mg-Fe-Ca pyroxenes. Am Mineral 85:473–479

Irvine TN (1965) Chromian spinel as a petrogenetic indicator. Part I. Theory. Can J Earth Sci 2:648-672

Irvine TN (1967) Chromian spinel as a petrogenetic indicator. Part II. Petrological applications. Can J Earth Sci 4:71-103

Irvine TN (1977) Origin of chromite layers in the Muskox intrusion and other stratiform intrusions: a new interpretation. Geol 5:273-277

Jianping L, Kornprobst J, Vielzeuf D, Fabriès J (1995) An improved experimental calibration of the olivine-spinel geothermometer. Chin J Geochem 14:68-77

Johan Z, Dunlop H, Le Bel L, Robert JL, Volfinger M (1983) Origin of chromite deposits in ophiolitic complexes: evidence for a volatile and sodium-rich reducing fluid phase. Fortschr Miner 61:105-107

Kakkala M, Sharma SK (1993) A Raman spectral study of forsterite-monticellite solid solutions. Am Mineral 78:42-48

Kamenetsky VS, Crawford AJ, Meffre S (2001) Factors controlling chemistry of magmatic spinel: an empirical study of associated olivine, Cr-spinel, and melt inclusions from primitive rocks. J Petrol 42:655-671

Kapsiotis A, Grammatikopoulos TA, Tsikouras B, Hatzipanagiotou K, Zaccarini F, Garuti G (2011) Mineralogy, composition and PGM of chromitites from Pefki, Pindos ophiolite complex (NW Greece): Evidence for progressively elevated fAs conditions in the upper mantle sequence. Mineral Petrol 101:129-150

Keays RR (1995) The role of komatiitic and picritic magmatism and S saturation in the formation of ore deposits. Lithos 34:1-18

Kolesov BA, Geiger CA (2003) A Raman spectroscopic study of Fe–Mg olivines. Phys Chem Min 31:142-154

Lagabrielle Y, Lemoine M (1997) Alpine, Corsican and Apennine ophiolites: The slow-spreading ridge model. C R Acad Sci (Ser IIa Sci) Terre Planétes 325:909-920

Leblanc M, Nicolas A (1992) Les chromitites ophiolitiques. Chron Rech Min 507:3-25

Lehmann J (1983) Diffusion between olivine and spinel: application to geothermometry. Earth Planet Sci Lett 64:123-138

Lemoine M, Tricart P, Boillot G (1987) Ultramafic and gabbroic ocean floor of the Ligurian Tethys (Alps, Corsica, Apennines): in search of a genetic model. Geol 15:622-625

Li C, Naldrett AJ (1993) Sulfide capacity of magma: a quantitative model and its application to the formation of sulphide ores at Sudbury. Econ Geol 88:1253-1260

Liermann HP, Ganguly J (2003) Fe^{2+}-Mg fractionation between orthopyroxene and spinel: experimental calibration in the system FeO–MgO–Al_2O_3–Cr_2O_3–SiO_2, and applications. Contrib Mineral Petrol 145:217-227

Liermann HP, Ganguly J (2007) Fe^{2+}-Mg fractionation between orthopyroxene and spinel: experimental calibration in the system FeO–MgO–Al_2O_3–Cr_2O_3–SiO_2, and applications. Contrib Mineral Petrol 154:491

MacLean WH (1969) Liquidus phase relations in the FeS-FeO-Fe_3O_4-SiO_2 system, and their application in geology. Econ Geol 64:865-884

Maier WD (2005) Platinum-group element (PGE) deposits and occurrences: Mineralization styles, genetic concepts, and exploration criteria. J Afr Earth Sci 41:165-191

Malitch KN, Junk SA, Thalhammer OAR, Melcher F, Knauf VV, Pernicka E, Stumpfl EF (2003) Laurite and ruarsite from podiform chromitites at Kraubath and Hochgrössen, Austria: new insights from osmium isotopes. Can Mineral 41:331-352

Maurel C, Maurel P (1982) Etude experimentale de la distribbution de L'aluminium entre bain silicate basique et spinelle chromifere: implications petrogenetiques, teneur en chrome des spinelles. Bull Minéral 105:197-202

Mavrogenes JA, O'Neill HSC (1999): The relative effects of pressure, temperature and oxygen fugacity on the solubility of sulfide melts in mafic magmas. Geochim Cosmochim Acta 63:1173–1180.

Melcher F, Grum W, Simon G, Talhammer TV, Stumpfl EF (1997) Petrogenesis of the ophiolitic giant chromite deposits of Kempirsai, Kazakhstan: a study of solid and fluid inclusions in chromite. J Petrol 38:1419-1458

Melcher F, Grum W, Thalhammer TV, Thalhammer OAR (1999) The giant chromite deposits at Kempirsai, Urals: constraints from trace element (PGE, REE) and isotope data. Miner Depos 34:250-272

Misra KC (1999) Understanding mineral deposits. Kluwer Acad Publ, Boston

Naldrett AJ, Kinnard JA, Wilson A, Yudovskaya M, McQuade S, Chunnett G, Stanley C (2009) Chromite composition and PGE content of Bushveld chromitites: Part I – The Lower and Middle Groups. Trans Inst Min Metall (Sect B: Appl Earthsci) 118:131-161

Naldrett AJ, Lehmann J (1988) Spinel non-stoichiometry as the explanation for Ni-, Cu- and PGE-enriched sulfides in chromitites. In: Prichard HM, Potts PJ, Bowels JFW, Cribb SJ (eds) Proc Geo-Platinum 87 Symposium, Milton Keynes, Elsevier, pp 93-110

Naldrett AJ, Von Gruenewaldt G (1989) Association of Platinum-group elements with chromitites in layered intrusions and ophiolite complexes. Econ Geol 84:180-187

O'Neill HSC, Wall VJ (1987) The olivine-orthopyroxene-spinel oxygen geobarometer, the nickel precipitation curve, and the oxygen fugacity of the Earth's upper mantle. J Petrol 28:1169-l l91

Peck DC, Keays RR (1990) Insights into the behaviour of precious metals in primitive S-undersaturated magmas: evidence from the Heazlewood River complex, Tasmania. Can Mineral 28:553-577

Piccardo GB (2007) Evolution of the ultra-slow spreading Jurassic Ligurian Tethys: view from the mantle. Per Mineral 76:67-80

Piccardo GB (2008) The Jurassic Ligurian Tethys, a fossil ultra-slow spreading ocean: the mantle perspective. In: Coltorti M, Grogoire M (eds) Metasomatism in Oceanic and Continental Lithospheric Mantle. Geol Soc London Spec Publ 294:11-33

Piccardo GB, Guarnieri L (2010) Alpine peridotites from the Ligurian Tethys: an updated critical review. Intern Geol Rev 52:1138–1159.

Piccardo GB, Guarnieri L (2011) Gabbro-norite cumulates from strongly depleted MORB melts in the Alpine–Apennine ophiolites. Lithos 124:200-214

Piccardo GB, Rampone E, Romairone A (2002) Formation and composition of the oceanic lithosphere of the Ligurian Tethys: inferences from the Ligurian ophiolites. Ofioliti 27:145-161

Pohl WL (2011) Economic Geology, Principles and Practice: Metals, Minerals, Coal and Hydrocarbons - an Introduction to Formation and Sustainable Exploitation of Mineral Deposits. Wiley-Blackwell, Oxford.

Rampone E, Hoffmann AW, Raczek I (1998) Isotopic contrasts within the Internal Liguride ophiolite (N. Italy): the lack of a genetic peridotite - crust link. Earth Planet Sci Lett 163:175-189

Renna MR, Tribuzio R (2011) Olivine-rich troctolites from Ligurian ophiolites (Italy): Evidence for impregnation of replacive mantle conduits by MORB-type melts. J Petrol 52:1763-1790

Righter K (2001) Rhenium and iridium partitioning in silicate magmatic spinels: implications for planetary magmatism and mantles. Lun Planet Sci 32:1759

Robb LJ (2005) Introduction to ore-forming processes. Wiley-Blackwell, Oxford.

Roberts S (1988) Ophiolitic chromite formation: A marginal basin phenomenon? Econ Geol 83:1034-1036

Robertson AHF (2002) Overview of the genesis and emplacement of mesozoic ophiolites in the Eastern Mediterranean Tethyan region. Lithos 65:1-67

Roeder PL (1994) Chromite: from their fiery rain of chondrules to the Kilauea Iki lava lake. Can Mineral 32:729-746

Rollinson H (2008) The geochemistry of mantle chromitites from the northern part of the Oman ophiolite: inferred parental melt compositions. Contrib Mineral Petrol 156:273-288

Rruff project database, http://rruff.info [accessed 02.05.2012]

Spangeberg K (1943) Die Chromitlagerstadtte von Tampadel am Zobten. Z prakt Geol 5:13-35

Stampfli G (1993) Le Briançonnais: Terrain exotique dans les Alpes? Ecl Geol Helv 86:1–45

Stella A (1924) Sopra un giacimento di cromite nel Vallone Argentiera presso Ziona (Alta Valle Vara). Boll Soc Geol It 43:183-188

Stowe CW (1994) Compositions and tectonic settings of chromite deposits through time. Econ Geol 89:528-546

Thayer TP (1970) Chromite segregations as petrogenetic indicators. Geol Soc S Africa Spec Publ 1:380-90

Tribuzio R, Thirlwall MF, Vannucci R (2004) Origin of the Gabbro-Peridotite Association from the Northern Apennine Ophiolites (Italy). J Petrol 45:1109-1124

Von Gruenewaldt G, Merkle RKW (1995) Platinum group element proportions in chromitites of the Bushveld complex: implications for fractionation and magma mixing models. J Afr Earth Sci 21:615-632

Wang A, Freeman J, Kuebler KE (2002) Raman Spectroscopic Characterization of Phyllosilicates. Lun Plan Sc Conf 33, abstr 1374

Wang A, Kuebler KE, Jolliff BL, Haskin LA (2004) Raman spectroscopy of Fe-Ti-Cr-oxides, case study: Martian meteorite EETA79001. Am Mineral 89:665-680

Wilson M (1989) Igneous Petrogenesis: A global tectonic approach. Unwin Hyman, Boston

Zaccarini F, Garuti G, Proenza JA, Campos L, Thalhammer OAR, Aiglsperger T, Lewis J (2011) Chromite and platinum-group-elements mineralization in the Santa Elena ophiolitic ultramafic nape (Costa Rica): geodynamic implications. Geol Acta 9:407-423

Zaccarini F, Proenza JA (2005) Zirconolite from upper mantle chromitite: a key to understanding mantle metasomatic processes. Actas XVI Congr Geol Argentino, Resumenes, La Plata, pp 346

Zhou MF, Robinson PT (1994) High-Cr and high-Al podiform chromitites, Western China: Relationship to partial melting and melt/rock reaction in the upper mantle. Intern Geol Rev 36:678-686

Zhou MF, Robinson PT, Bai WJ (1994) Formation of podiform chromitites by melt/rock interaction in the upper mantle. Miner Dep 29:98-101

Zhou MF, Sun M., Keays RR, Kerrich RW (1998) Controls on platinum-group elemental distributions of podiform chromitites: A case study of high-Cr and high-Al chromitites from Chinese orogenic belts. Geochim Cosmochim Acta 62:677-688

18. APPENDIX

18.1. Electron probe microanalyses (EPMA)

18.1.1. Chromites

Tab. 12 (part 1) Electron probe microanalyses on chromites from chromitite layers of the Cima Stronzi occurrence (wt%).

	SiO_2	TiO_2	Al_2O_3	Cr_2O_3	V_2O_3	MgO	FeO	MnO	NiO	ZnO	Total
SR38-1	0.06	0.60	30.53	32.28	0.15	11.24	22.96	0.16	0.57	-	98.55
SR38-2	<d.l.	0.61	30.55	31.79	0.15	11.33	22.97	0.22	0.88	-	98.50
SR38-3	0.05	0.70	31.25	31.65	0.17	11.73	22.73	0.18	0.67	-	99.13
SR38-4	<d.l.	0.62	30.38	32.47	0.15	11.30	23.09	0.22	0.59	-	98.82
SR38-5	<d.l.	0.59	29.74	33.02	0.16	11.11	23.26	0.21	0.64	-	98.73
SR38-6	0.04	0.57	29.42	32.80	0.17	11.17	23.96	0.19	0.75	-	99.07
SR38-7	<d.l.	0.67	31.27	31.56	0.17	11.54	23.13	0.18	0.60	-	99.12
SR38-8	<d.l.	0.68	31.15	32.04	0.15	11.55	22.81	0.19	0.94	-	99.51
SR38-9	0.03	0.58	31.31	31.11	0.14	11.73	23.02	0.17	0.37	-	98.46
SR38-10	<d.l.	0.52	31.05	31.89	0.15	11.33	24.04	0.23	0.48	-	99.69
SR38-11	0.07	0.64	31.29	30.97	0.15	11.82	22.97	0.23	1.00	-	99.14
SR38-12	0.02	0.57	30.86	31.60	0.15	11.95	22.27	0.21	0.75	-	98.38
SR38-13	0.04	0.62	31.79	31.39	0.16	11.96	22.29	0.20	0.61	-	99.06
SR38-14*	3.92	0.74	1.97	32.86	0.13	3.46	54.23	5.56	<d.l.	-	102.87
SR38-15*	3.75	0.64	1.88	33.02	0.15	3.54	51.67	5.60	0.06	-	100.31
SR38-16*	3.92	0.74	1.87	32.51	0.08	3.63	53.47	5.38	0.39	-	101.99
SR38-17*	3.49	0.76	1.90	33.05	0.11	3.40	52.36	5.59	0.28	-	100.94
SR38-18*	4.24	0.66	1.93	32.17	0.13	4.10	52.54	5.58	0.13	-	101.48
SR38-19*	3.47	0.70	1.79	33.26	0.12	3.48	51.58	5.69	0.29	-	100.38
SR38-20*	3.08	0.82	1.90	33.61	0.12	3.17	52.98	5.76	0.05	-	101.49
SR38-21*	3.49	0.78	1.98	33.24	0.08	3.51	51.05	5.60	0.23	-	99.96
SR38-22*	3.72	0.76	2.16	33.41	0.13	3.65	51.85	5.66	<d.l.	-	101.34
SR38-25*	3.57	0.81	1.86	32.73	0.10	3.53	51.45	5.48	0.21	-	99.74
SR38-26*	5.29	0.98	2.58	32.43	0.07	5.33	48.80	5.35	0.08	-	100.91
SR38-27	<d.l.	0.60	30.36	32.40	0.15	11.32	24.13	0.19	0.16	-	99.31

<d.l., below detection limit; *, ferrian chromite; SR, Cima Stronzi

Tab. 12 (part 2) Electron probe microanalyses on chromites from chromitite layers of the Cima Stronzi occurrence (wt%).

	SiO_2	TiO_2	Al_2O_3	Cr_2O_3	V_2O_3	MgO	FeO	MnO	NiO	ZnO	Total
SR38-28	0.05	0.59	31.44	31.38	0.14	11.68	23.41	0.18	0.81	<d.l.	99.68
SR39-1	<d.l.	0.65	24.51	37.85	0.18	14.33	19.79	0.27	0.08	-	97.66
SR39-2	<d.l.	0.58	26.61	35.43	0.23	14.15	21.02	0.28	0.19	-	98.49
SR39-3	<d.l.	0.63	26.04	35.38	0.23	13.96	21.12	0.31	0.11	-	97.78
SR39-4	<d.l.	0.70	26.52	35.83	0.15	14.32	20.82	0.27	0.18	-	98.79
SR39-5	<d.l.	0.63	25.38	36.38	0.17	13.98	21.50	0.35	0.11	-	98.50
SR39-6	<d.l.	0.56	25.10	36.59	0.18	15.01	18.70	0.30	0.14	-	96.58
SR39-7	<d.l.	0.66	25.38	36.45	0.22	15.06	18.18	0.29	0.23	-	96.47
SR39-8	<d.l.	0.58	24.75	36.64	0.21	14.90	18.44	0.27	0.17	-	95.96
SR39-9	<d.l.	0.73	24.54	36.58	0.20	14.07	20.60	0.31	0.22	-	97.25
SR39-10	<d.l.	0.71	26.97	36.52	0.15	14.58	19.50	0.18	0.21	-	98.82
SR39-11	<d.l.	0.63	26.83	35.80	0.17	15.12	19.21	0.29	0.18	-	98.23
SR39-12	<d.l.	0.68	26.45	35.39	0.19	14.44	20.40	0.26	0.21	-	98.02
SR39-13	<d.l.	0.59	26.70	35.18	0.21	14.55	20.27	0.26	0.20	-	97.96
SR39-14	<d.l.	0.55	25.74	35.61	0.17	14.09	20.51	0.29	0.18	-	97.14
SR39-15	<d.l.	0.67	25.91	34.61	0.24	14.03	20.26	0.33	0.15	-	96.20
SR39-16	<d.l.	0.70	25.75	35.23	0.14	14.09	20.58	0.28	0.11	-	96.88
SR39-17	<d.l.	0.82	22.31	39.97	0.18	14.04	20.05	0.28	0.20	-	97.85
SR39-18	<d.l.	0.66	23.67	38.61	0.16	14.59	19.35	0.34	0.18	-	97.56
SR39-19	<d.l.	0.79	22.44	40.19	0.22	14.17	19.63	0.38	0.13	-	97.95
SR39-20	<d.l.	0.66	25.95	37.23	0.16	15.16	18.40	0.28	0.21	-	98.05
SR39-21	<d.l.	0.51	26.25	36.78	0.22	15.48	18.06	0.27	0.20	-	97.77
SR39-22	<d.l.	0.59	25.89	37.10	0.22	15.39	18.24	0.26	0.18	-	97.87
SR39-23	<d.l.	0.56	26.55	36.56	0.18	15.67	17.77	0.19	0.22	-	97.70
SR39-24	<d.l.	0.68	25.65	37.33	0.14	15.09	18.62	0.25	0.18	-	97.94
SR40A-1	-	0.66	27.66	35.04	0.16	15.47	18.90	0.29	0.23	0.05	98.46
SR40A-2	-	0.66	27.38	35.98	0.21	15.57	19.16	0.24	0.15	0.05	99.40
SR40A-3	-	0.72	26.33	37.05	0.24	14.82	18.91	0.21	0.17	0.05	98.50
SR40A-4	-	0.64	27.15	36.31	0.20	15.39	19.07	0.22	0.19	0.06	99.23
SR40A-5	-	0.69	24.03	39.24	0.15	14.50	20.04	0.27	0.17	0.12	99.21
SR40A-6	-	0.42	28.43	34.59	0.16	15.81	18.75	0.28	0.21	<d.l.	98.65

<d.l., below detection limit; SR, Cima Stronzi

Tab. 12 (part 3) Electron probe microanalyses on chromites from chromitite layers of the Cima Stronzi occurrence (wt%).

	SiO_2	TiO_2	Al_2O_3	Cr_2O_3	V_2O_3	MgO	FeO	MnO	NiO	ZnO	Total
SR40A-7	-	0.73	27.78	34.78	0.15	15.47	18.82	0.25	0.21	0.18	98.37
SR40A-8	-	0.69	27.72	35.86	0.20	15.52	18.95	0.26	0.18	0.11	99.49
SR40A-9	-	0.72	27.34	35.83	0.24	15.33	19.34	0.30	0.25	0.12	99.47
SR40A-10	-	0.61	27.69	35.81	0.15	15.27	19.00	0.28	0.20	0.10	99.11
SR40A-11	-	0.65	28.26	34.91	0.18	15.53	18.53	0.27	0.23	0.03	98.59
SR45C-1	<d.l.	0.50	30.10	33.91	0.16	12.42	20.67	0.23	0.39	-	98.38
SR45C-2	0.02	0.36	30.07	32.65	0.16	12.27	21.51	0.20	0.39	-	97.63
SR45C-3	0.04	0.53	30.09	34.11	0.15	12.34	20.36	0.17	0.57	-	98.36
SR45C-4	0.08	0.40	29.22	34.18	0.15	12.26	20.59	0.20	0.40	-	97.48
SR45C-5	0.06	0.42	30.10	34.11	0.17	12.38	20.60	0.23	0.62	-	98.69
SR45C-6	<d.l.	0.42	30.89	32.43	0.16	12.65	21.20	0.16	0.52	-	98.43
SR45C-7	0.08	0.47	30.44	33.10	0.16	12.48	20.05	0.21	0.28	-	97.27
SR45C-8	<d.l.	0.46	29.91	34.20	0.17	12.37	20.76	0.20	0.42	-	98.49
SR45C-9	0.06	0.61	29.08	34.45	0.15	12.27	20.78	0.17	0.50	-	98.07
SR45C-10	0.04	0.70	29.36	33.85	0.16	12.20	21.11	0.22	0.15	-	97.79
SR45C-11	<d.l.	0.46	29.77	34.42	0.16	12.44	20.34	0.18	0.65	-	98.42
SR45C-12	<d.l.	0.70	29.33	34.07	0.19	12.41	21.06	0.22	0.39	-	98.37
SR45C-13	0.05	0.57	29.81	33.80	0.16	12.45	20.05	0.18	0.49	-	97.56
SR45C-14	<d.l.	0.49	29.71	33.93	0.16	12.27	20.39	0.21	0.75	-	97.91
SR45C-15	0.04	0.59	29.68	34.31	0.13	12.32	19.90	0.16	0.46	-	97.59
SR45C-16	0.09	0.61	29.57	33.64	0.16	12.42	20.18	0.18	0.64	-	97.49
SR45C-17	<d.l.	0.73	28.61	34.58	0.16	11.94	20.77	0.19	0.71	-	97.69
SR45C-18	0.08	0.63	28.98	34.18	0.18	12.42	20.95	0.20	0.82	-	98.44
SR45C-19	<d.l.	0.50	30.11	33.88	0.14	12.61	20.35	0.19	0.25	-	98.03
SR45C-20	0.04	0.63	29.48	33.84	0.16	12.62	20.10	0.17	0.72	-	97.76
SR45C-21	<d.l.	0.64	29.60	34.18	0.16	12.26	20.27	0.17	0.59	-	97.87
SR45C-22	<d.l.	0.67	29.73	33.87	0.16	12.41	20.06	0.21	0.65	-	97.76
SR45C-23	0.02	0.58	30.53	33.61	0.16	12.86	20.31	0.19	0.36	-	98.62
SR45C-24	<d.l.	0.55	30.13	33.26	0.17	12.60	20.65	0.16	0.80	-	98.32

<d.l., below detection limit; SR, Cima Stronzi

Tab. 13 (part 1) Electron probe microanalyses on chromites from chromitite layers of the Ziona occurrence (wt%).

	SiO_2	TiO_2	Al_2O_3	Cr_2O_3	V_2O_3	MgO	FeO	MnO	NiO	ZnO	Total
ZN15-1	-	0.55	26.92	38.44	0.20	14.49	18.66	0.26	0.21	<d.l.	99.73
ZN15-2	-	0.50	27.66	37.46	0.17	14.66	18.85	0.26	0.14	<d.l.	99.70
ZN15-3	-	0.54	26.53	38.88	0.18	14.34	19.26	0.19	0.21	<d.l.	100.13
ZN15-4	-	0.59	26.38	38.70	0.18	14.40	19.18	0.30	0.11	<d.l.	99.84
ZN15-5	-	0.50	26.64	39.75	0.18	14.59	19.06	0.25	0.15	<d.l.	101.12
ZN15-6	-	0.53	26.72	38.91	0.17	14.58	18.86	0.25	0.14	<d.l.	100.16
ZN15-7	-	0.78	27.26	39.40	0.18	14.65	19.07	0.24	0.16	<d.l.	101.74
ZN15-8	-	0.60	26.33	39.62	0.21	14.31	19.11	0.30	0.16	<d.l.	100.64
ZN15-9	-	0.68	26.06	38.65	0.15	14.61	18.79	0.30	0.16	<d.l.	99.40
ZN15-10	-	0.64	27.98	38.95	0.18	14.90	18.46	0.24	0.22	<d.l.	101.57
ZN15-11	-	0.79	26.69	39.41	0.18	14.77	19.04	0.22	0.13	<d.l.	101.23
ZN15-12	-	0.66	27.43	38.07	0.18	15.14	18.46	0.29	0.06	<d.l.	100.29
ZN15-13	-	0.79	27.54	38.79	0.17	15.02	18.96	0.28	0.08	<d.l.	101.63
ZN22-1	<d.l.	0.74	27.41	35.81	0.23	12.17	19.87	0.22	0.32	-	96.77
ZN22-2	<d.l.	0.68	26.96	35.62	0.22	11.80	21.91	0.17	0.36	-	97.72
ZN22-3	0.08	0.63	27.23	35.40	0.16	12.23	21.07	0.16	0.20	-	97.16
ZN22-4	0.04	0.78	26.55	35.82	0.21	12.37	21.78	0.19	0.37	-	98.11
ZN22-5	<d.l.	0.66	27.37	35.90	0.21	12.47	20.18	0.16	0.25	-	97.20
ZN22-6	<d.l.	0.57	27.30	35.67	0.19	12.71	20.98	0.19	0.46	-	98.07
ZN22-7	0.02	0.63	27.60	35.37	0.21	12.27	20.91	0.19	0.71	-	97.91
ZN22-8	<d.l.	0.77	27.24	35.94	0.18	12.32	20.95	0.19	0.52	-	98.11
ZN22-9	0.03	0.72	26.69	36.33	0.16	12.16	20.66	0.18	0.41	-	97.34
ZN22-10	0.04	0.68	26.73	35.91	0.19	11.94	21.75	0.20	0.41	-	97.85
ZN22-11	0.07	0.79	27.33	35.69	0.20	12.31	20.25	0.15	0.58	-	97.37
ZN22-12	0.04	0.67	27.80	35.53	0.17	12.48	19.81	0.21	0.67	-	97.38
ZN22-13	<d.l.	0.78	26.64	35.86	0.14	11.29	22.80	0.21	0.30	-	98.02
ZN22-14	<d.l.	0.69	27.68	35.42	0.19	12.33	20.21	0.18	0.54	-	97.24
ZN22-15	0.02	0.74	27.46	36.54	0.21	12.47	19.69	0.23	0.53	-	97.89
ZN22-16	0.03	0.59	27.19	36.39	0.14	12.26	19.64	0.19	0.40	-	96.83
ZN22-17	<d.l.	0.64	26.75	36.18	0.16	12.23	20.47	0.19	0.57	-	97.19
ZN22-18	<d.l.	0.57	26.77	36.09	0.15	12.24	20.34	0.16	0.55	-	96.87

<d.l., below detection limit; ZN, Ziona

Tab. 13 (part 2) Electron probe microanalyses on chromites from chromitite layers of the Ziona occurrence (wt%).

	SiO_2	TiO_2	Al_2O_3	Cr_2O_3	V_2O_3	MgO	FeO	MnO	NiO	ZnO	Total
ZN22-19	0.04	0.71	26.86	36.32	0.26	12.35	19.99	0.17	0.35	-	97.05
ZN22-20	0.06	0.63	26.71	36.44	0.19	11.65	22.21	0.20	0.08	-	98.17
ZN22-21	0.06	0.82	26.60	36.72	0.21	12.10	20.55	0.18	0.38	-	97.62
ZN22-22	0.07	0.72	27.08	36.07	0.23	12.34	19.99	0.16	0.56	-	97.22
ZN22-23	<d.l.	0.64	27.07	36.30	0.19	12.14	20.93	0.17	0.50	-	97.94

<d.l., below detection limit; ZN, Ziona

Tab. 14 (part 1) Electron probe microanalyses on chromites from chromitite layers of the Pian della Madonna occurrence (wt%).

	SiO_2	TiO_2	Al_2O_3	Cr_2O_3	V_2O_3	MgO	FeO	MnO	NiO	ZnO	Total
PM23B-1	-	0.51	29.87	36.33	0.16	11.92	21.67	0.30	0.11	<d.l.	100.87
PM23B-2	-	0.65	29.48	35.98	0.21	11.84	22.18	0.28	0.13	<d.l.	100.75
PM23B-3	-	0.64	30.26	35.80	0.18	12.00	21.51	0.28	0.12	<d.l.	100.79
PM23B-4	-	0.68	29.55	35.78	0.15	12.13	21.72	0.28	0.13	<d.l.	100.42
PM23B-5	-	0.52	30.40	35.38	0.20	12.07	21.46	0.27	0.13	<d.l.	100.43
PM23B-6	-	0.68	30.75	35.28	0.16	12.25	20.86	0.30	0.09	<d.l.	100.37
PM23B-7	-	0.76	29.04	36.54	0.17	11.92	21.81	0.29	0.13	<d.l.	100.66
PM23B-8	-	0.70	28.74	35.89	0.21	11.71	22.59	0.27	0.20	<d.l.	100.31
PM25-1	<d.l.	0.55	27.73	36.32	0.18	13.14	19.59	0.17	0.47	-	98.15
PM25-2	0.04	0.66	27.75	35.39	0.17	12.94	20.17	0.15	0.60	-	97.87
PM25-3	0.04	0.67	28.13	35.63	0.20	12.91	20.44	0.25	0.45	-	98.72
PM25-4	0.08	0.60	27.53	35.77	0.18	12.78	21.12	0.22	0.53	-	98.81
PM25-5	<d.l.	0.67	27.50	35.81	0.17	12.81	21.24	0.20	0.56	-	98.96
PM25-6	<d.l.	0.66	27.48	35.76	0.15	12.75	21.04	0.18	0.22	-	98.24
PM25-7	<d.l.	0.58	28.06	35.46	0.21	12.76	20.65	0.21	0.28	-	98.21
PM25-8	<d.l.	0.63	27.88	35.99	0.18	12.75	20.78	0.18	0.42	-	98.81
PM25-9	<d.l.	0.65	27.45	35.25	0.21	12.71	20.34	0.23	0.22	-	97.06
PM25-10	0.03	0.63	28.21	35.37	0.16	13.03	19.15	0.23	0.09	-	96.90
PM25-11	0.08	0.65	28.40	35.49	0.18	13.07	20.33	0.18	0.58	-	98.96
PM25-12	0.08	0.64	28.02	35.25	0.20	12.85	20.09	0.14	0.71	-	97.98
PM25-13	0.03	0.56	28.50	36.34	0.17	13.10	20.49	0.20	0.27	-	99.66
PM25-14	0.02	0.60	27.90	36.05	0.16	12.90	20.79	0.26	0.57	-	99.25
PM25-15	0.08	0.61	27.27	36.77	0.15	12.56	20.15	0.28	0.48	-	98.35
PM25-16	<d.l.	0.58	28.03	35.65	0.14	13.08	19.65	0.18	0.35	-	97.66
PM25-17	0.02	0.72	27.82	35.78	0.21	12.55	21.06	0.20	0.54	-	98.90
PM25-18	0.04	0.75	26.46	35.11	0.18	11.78	22.12	0.22	0.46	-	97.12
PM25-19	0.05	0.59	24.11	33.82	0.16	11.96	17.52	0.17	0.23	-	88.61
PM25-20	0.03	0.60	27.14	35.68	0.17	12.04	21.96	0.24	0.27	-	98.13
PM25-21	0.08	0.79	27.08	35.76	0.18	12.66	20.72	0.21	0.54	-	98.02
PM25-22	0.02	0.62	26.25	37.21	0.16	12.42	19.74	0.15	0.26	-	96.83
PM25-23	<d.l.	0.57	27.32	36.42	0.16	12.77	20.69	0.22	0.34	-	98.49

<d.l., below detection limit; PM, Pian della Madonna

Tab. 14 (part 2) Electron probe microanalyses on chromites from chromitite layers of the Pian della Madonna occurrence (wt%).

	SiO_2	TiO_2	Al_2O_3	Cr_2O_3	V_2O_3	MgO	FeO	MnO	NiO	ZnO	Total
PM25-24	0.02	0.67	26.64	36.16	0.19	12.37	20.93	0.23	0.32	-	97.53
PM25-25	0.03	0.67	27.27	35.92	0.19	12.44	21.48	0.21	0.55	-	98.76
PM25-26	0.04	0.66	27.02	35.61	0.18	12.55	21.33	0.21	0.33	-	97.93
PM25-27	<d.l.	0.64	27.35	36.02	0.17	12.03	23.21	0.19	0.27	-	99.88
PM25-28	<d.l.	0.63	27.70	36.12	0.21	12.79	21.24	0.29	0.26	-	99.24

<d.l., below detection limit; PM, Pian della Madonna

Tab. 15 Electron probe microanalyses on chromites from chromitite layers of the Pian della Madonna occurrence (wt%).

	SiO_2	TiO_2	Al_2O_3	Cr_2O_3	V_2O_3	MgO	FeO	MnO	NiO	ZnO	Total
CN53-1	<d.l.	0.65	30.61	32.44	0.18	12.13	20.29	0.16	0.64	<d.l.	97.10
CN53-2	0.02	0.37	31.61	32.30	0.14	12.50	18.72	0.18	0.54	<d.l.	96.38
CN53-3	<d.l.	0.56	30.78	32.37	0.18	12.18	20.46	0.18	0.33	<d.l.	97.04
CN53-4	0.09	0.50	31.68	32.74	0.12	12.46	19.53	0.17	0.89	<d.l.	98.18
CN53-5	0.03	0.54	31.12	32.26	0.12	12.18	20.00	0.16	0.60	<d.l.	97.01
CN53-6	0.03	0.59	31.31	32.19	0.16	12.39	20.55	0.15	0.70	<d.l.	98.07
CN53-7	0.09	0.41	30.71	32.49	0.16	12.13	20.28	0.21	0.76	<d.l.	97.24
CN53-8	<d.l.	0.60	30.98	32.42	0.15	12.37	20.96	0.15	0.50	<d.l.	98.13
CN53-9	0.02	0.57	31.12	33.03	0.16	12.24	19.29	0.13	0.50	<d.l.	97.06
CN53-10	0.02	0.56	30.86	32.50	0.17	12.27	20.35	0.20	0.60	<d.l.	97.53
CN53-11	0.04	0.52	31.29	32.65	0.13	12.40	18.92	0.17	0.77	<d.l.	96.89
CN53-12	<d.l.	0.62	31.50	32.50	0.20	12.43	19.44	0.16	0.77	<d.l.	97.62
CN53-13	<d.l.	0.37	31.59	32.92	0.16	12.65	18.75	0.15	0.32	<d.l.	96.91
CN53-14	0.02	0.47	31.69	32.57	0.17	12.62	19.25	0.12	0.46	<d.l.	97.37
CN53-15	0.05	0.45	31.57	32.81	0.18	12.84	18.42	0.21	0.44	<d.l.	96.97
CN53-16	<d.l.	0.42	31.33	32.70	0.17	12.85	18.32	0.15	0.36	<d.l.	96.30
CN53-17	<d.l.	0.47	31.74	32.49	0.18	12.77	18.48	0.16	0.69	<d.l.	96.98
CN53-18	<d.l.	0.62	31.47	32.74	0.17	12.61	19.10	0.15	0.52	<d.l.	97.38
CN53-19	0.04	0.55	31.36	32.75	0.08	12.79	19.12	0.14	0.91	<d.l.	97.74
CN53-20	0.03	0.54	31.22	32.64	0.12	12.71	19.03	0.19	0.49	<d.l.	96.97
CN53-21	<d.l.	0.48	31.51	32.44	0.17	12.68	19.03	0.21	0.47	<d.l.	96.99
CN53-22	<d.l.	0.56	31.91	32.44	0.11	13.15	18.75	0.14	0.43	<d.l.	97.49
CN53-23	0.06	0.37	31.39	32.63	0.09	12.80	19.48	0.20	0.48	<d.l.	97.50
CN53-24	0.05	0.51	31.45	32.57	0.18	12.82	18.83	0.16	0.86	<d.l.	97.43
CN53-25	<d.l.	0.50	31.23	32.62	0.19	12.95	19.63	0.14	0.25	<d.l.	97.51
CN53-26	<d.l.	0.50	31.67	32.89	0.12	12.96	18.26	0.14	0.40	<d.l.	96.94
CN53-27	0.07	0.62	31.14	32.22	0.22	12.90	19.38	0.18	0.42	<d.l.	97.15
CN53-28	<d.l.	0.50	31.35	32.63	0.16	12.82	18.90	0.17	0.34	<d.l.	96.87
CN53-29	<d.l.	0.58	31.49	32.60	0.15	12.96	18.96	0.15	0.34	<d.l.	97.23
CN53-30	0.05	0.48	31.20	32.63	0.16	12.51	19.10	0.14	0.61	<d.l.	96.88

<d.l., below detection limit; CN, Canegreca

Tab. 16 (part 1) Electron probe microanalyses on disseminated chromites from the serpentinized dunites of Cima Stronzi (wt%).

	SiO_2	TiO_2	Al_2O_3	Cr_2O_3	V_2O_3	MgO	FeO	MnO	NiO	ZnO	Total
SR32-1	-	0.48	25.30	35.68	0.19	14.02	22.97	0.28	0.17	0.13	99.22
SR32-2	-	0.66	23.88	35.27	0.16	13.64	23.14	0.31	0.21	0.21	97.48
SR32-3	-	0.56	24.52	35.06	0.23	13.73	22.62	0.30	0.12	0.28	97.42
SR32-4	-	0.59	23.09	34.73	0.16	13.64	22.50	0.22	0.15	0.19	95.27
SR32-5	-	0.59	23.46	34.54	0.18	13.74	22.23	0.34	0.17	0.12	95.37
SR32-6	-	0.54	23.59	34.65	0.13	13.91	22.18	0.28	0.06	0.14	95.48
SR32-7	-	0.65	23.12	34.64	0.15	13.90	22.27	0.29	0.24	0.29	95.55
SR32-8	-	0.57	25.23	35.95	0.20	14.32	21.96	0.26	0.14	0.27	98.90
SR32-9	-	0.58	25.23	35.16	0.18	14.09	22.20	0.32	<d.l.	0.08	97.84
SR32-10	-	0.53	25.67	36.06	0.13	13.87	22.30	0.33	0.17	0.26	99.32
SR32-11	-	0.63	25.82	34.14	0.24	13.92	23.17	0.34	0.12	0.19	98.57
SR32-12	-	0.65	25.77	34.33	0.16	13.78	23.01	0.29	0.12	0.12	98.23
SR32-13	-	0.67	24.86	35.97	0.17	13.84	23.60	0.27	0.15	0.18	99.71
SR32-14	-	0.61	25.49	36.08	0.23	14.10	22.17	0.32	0.17	0.14	99.31
SR33-1	-	0.85	22.69	36.55	0.19	13.64	22.86	0.32	0.10	0.20	97.40
SR33-2	-	0.82	22.89	36.70	0.15	13.48	22.67	0.28	0.20	0.19	97.38
SR33-3	-	0.73	23.07	36.87	0.19	13.37	22.45	0.27	0.13	0.14	97.22
SR33-4	-	0.81	22.96	36.89	0.28	13.76	22.49	0.26	0.11	0.17	97.73
SR33-5	-	0.79	23.69	36.67	0.25	13.50	23.11	0.30	0.20	0.14	98.65
SR33-6	-	0.77	23.71	37.12	0.23	13.55	23.04	0.30	0.18	0.24	99.14
SR33-7	-	0.84	24.08	35.94	0.21	14.14	22.39	0.25	0.22	0.07	98.14
SR33-8	-	0.85	23.94	36.83	0.16	13.80	22.51	0.30	0.16	0.20	98.75
SR33-9	-	0.70	23.00	36.34	0.23	13.74	21.91	0.26	0.08	<d.l.	96.26
SR33-10	-	0.68	22.70	36.95	0.19	13.91	22.14	0.27	0.13	<d.l.	96.97
SR33-11	-	0.73	22.83	36.70	0.23	13.78	22.03	0.27	0.19	0.14	96.90
SR33-12	-	0.65	23.38	36.63	0.17	13.97	21.22	0.30	0.16	0.14	96.62
SR33-13	-	0.83	22.75	36.74	0.19	13.41	22.88	0.37	0.18	0.10	97.45
SR33-14	-	0.79	23.39	36.55	0.27	13.75	22.23	0.30	0.11	0.13	97.52
SR34-1	-	0.78	24.32	36.81	0.23	13.49	22.78	0.31	0.11	0.15	98.98
SR34-2	-	0.68	24.07	36.29	0.26	13.43	22.99	0.31	0.17	0.15	98.35
SR34-3	-	0.70	24.68	36.51	0.16	13.89	21.46	0.32	0.09	0.04	97.85

SR, Cima Stronzi

Tab. 16 (part 2) Electron probe microanalyses on disseminated chromites from the serpentinized dunites of Cima Stronzi (wt%).

	SiO_2	TiO_2	Al_2O_3	Cr_2O_3	V_2O_3	MgO	FeO	MnO	NiO	ZnO	Total
SR34-4	-	0.67	24.72	36.26	0.19	14.18	21.36	0.26	0.12	0.15	97.91
SR34-5	-	0.60	25.45	36.80	0.20	14.50	20.44	0.24	0.10	0.15	98.48
SR34-6	-	0.64	25.23	36.95	0.27	14.25	20.64	0.25	0.14	0.20	98.57
SR34-7	-	0.67	25.01	37.05	0.21	14.44	20.71	0.28	0.10	0.16	98.63

SR, Cima Stronzi

Tab. 17 (part 1) Electron probe microanalyses on disseminated chromites from the melatroctolites of Mattarana (wt%).

	SiO_2	TiO_2	Al_2O_3	Cr_2O_3	V_2O_3	MgO	FeO	MnO	NiO	ZnO	Total
MT28B-1	0.04	1.24	26.42	32.52	0.19	11.58	27.09	0.30	0.48	-	99.86
MT28B-2	0.05	1.13	22.69	36.00	0.25	9.77	30.35	0.29	0.09	-	100.62
MT28B-3	0.04	0.95	22.68	35.35	0.23	9.99	31.11	0.30	0.60	-	101.25
MT28B-4	<d.l.	1.37	21.94	36.00	0.26	9.91	31.44	0.28	0.13	-	101.33
MT28B-5	0.08	1.35	22.38	34.91	0.26	9.81	30.95	0.31	0.59	-	100.64
MT28B-6	<d.l.	1.43	23.12	34.32	0.26	9.77	31.87	0.25	0.36	-	101.38
MT28B-7	<d.l.	1.39	21.25	36.40	0.28	8.93	33.17	0.30	<d.l.	-	101.72
MT28B-8	0.07	1.53	22.18	35.47	0.28	10.22	29.86	0.30	0.27	-	100.18
MT28B-9	0.03	1.33	21.19	35.64	0.30	8.87	32.82	0.29	0.59	-	101.06
MT28B-10	<d.l.	1.24	22.13	36.31	0.26	9.07	32.32	0.30	0.52	-	102.15
MT28B-11	0.11	0.99	21.48	36.37	0.28	8.69	33.07	0.30	0.45	-	101.74
MT28B-12	0.05	1.41	17.57	38.00	0.35	6.53	38.39	0.38	0.42	-	103.10
MT28B-13	0.05	0.91	26.22	32.89	0.19	11.20	27.25	0.23	0.36	-	99.30
MT28B-14	<d.l.	1.01	26.80	32.70	0.20	11.53	27.81	0.22	0.48	-	100.75
MT28B-15	0.03	1.23	23.75	34.57	0.21	10.84	29.90	0.25	0.26	-	101.04
MT28B-16	<d.l.	1.09	25.08	32.76	0.20	11.09	27.93	0.23	0.63	-	99.01
MT28B-17	0.04	1.06	24.42	35.16	0.24	10.89	27.87	0.29	0.45	-	100.42
MT28B-18	-	1.03	25.36	34.13	0.27	10.02	29.39	0.30	0.24	<d.l.	100.74
MT28B-19	-	0.73	26.53	35.93	0.22	11.32	25.49	0.28	0.15	<d.l.	100.65
MT28B-20	-	0.95	25.73	35.19	0.26	10.49	28.02	0.44	0.23	<d.l.	101.31
MT28B-21	-	0.96	24.23	35.59	0.28	9.21	30.96	0.37	0.09	<d.l.	101.69
MT28B-22	-	0.98	23.47	35.54	0.28	8.54	31.66	0.46	0.21	<d.l.	101.14
MT28B-23	-	0.94	26.26	35.26	0.26	11.25	26.73	0.28	0.36	<d.l.	101.34
MT28B-24	-	1.10	23.94	36.68	0.28	10.08	28.67	0.39	0.09	<d.l.	101.23
MT28B-25	<d.l.	1.13	21.12	37.50	0.26	9.53	29.98	0.29	0.37	-	100.18
MT28B-26	0.03	1.16	19.41	39.60	0.25	9.30	29.68	0.30	0.47	-	100.20
MT28B-27	<d.l.	1.27	20.46	37.74	0.24	9.35	30.94	0.25	0.35	-	100.60
MT28B-28	0.02	1.25	20.66	37.83	0.26	9.32	30.71	0.34	0.31	-	100.70
MT28B-29	<d.l.	1.24	19.99	38.43	0.29	9.07	30.85	0.31	0.19	-	100.37
MT28B-30	0.05	1.01	20.38	37.89	0.26	8.19	32.08	0.35	0.13	-	100.34
MT28B-31	<d.l.	1.09	22.21	37.18	0.22	10.03	28.25	0.27	0.37	-	99.62
MT28B-32	0.03	1.00	21.92	37.35	0.25	9.89	28.32	0.25	0.36	-	99.37

<d.l., below detection limit; MT, Mattarana

Tab. 17 (part 2) Electron probe microanalyses on disseminated chromites from the melatroctolites of Mattarana (wt%).

	SiO_2	TiO_2	Al_2O_3	Cr_2O_3	V_2O_3	MgO	FeO	MnO	NiO	ZnO	Total
MT28B-33	<d.l.	1.13	21.12	37.50	0.26	9.53	29.98	0.29	0.37	-	100.18
MT28B-34	0.03	1.16	19.41	39.60	0.25	9.30	29.68	0.30	0.47	-	100.20
MT28B-35	<d.l.	1.27	20.46	37.74	0.24	9.35	30.94	0.25	0.35	-	100.60
MT28B-36	0.02	1.25	20.66	37.83	0.26	9.32	30.71	0.34	0.31	-	100.70
MT28C-37	<d.l.	1.24	19.99	38.43	0.29	9.07	30.85	0.31	0.19	-	100.37
MT28C-38	0.05	1.01	20.38	37.89	0.26	8.19	32.08	0.35	0.13	-	100.34
MT28C-39	<d.l.	1.09	22.21	37.18	0.22	10.03	28.25	0.27	0.37	-	99.62
MT28C-40	0.03	1.00	21.92	37.35	0.25	9.89	28.32	0.25	0.36	-	99.37
MT28C-41	<d.l.	1.31	21.13	36.75	0.24	9.26	30.87	0.25	0.16	-	99.97

<d.l., below detection limit; MT, Mattarana

18.1.2. Sulphides

Tab. 18 Electron probe microanalyses (base metal analyses) on pentlandite (wt%).

	As	Fe	S	Co	Ni	Zn	Cu	Total
SR45C-1	<d.l.	31.92	33.30	0.85	35.73	<d.l.	0.10	101.90
SR45C-2	<d.l.	31.89	33.12	1.05	35.88	<d.l.	<d.l.	101.94
SR45C-3	<d.l.	27.38	36.20	0.89	36.49	<d.l.	<d.l.	100.96
SR45C-4	<d.l.	32.32	33.28	0.80	35.78	<d.l.	0.10	102.28
SR45C-5	0.12	31.49	33.45	0.75	35.73	<d.l.	<d.l.	101.54
SR45C-6	0.05	27.77	34.66	0.68	37.72	<d.l.	0.13	101.01
SR45C-7	<d.l.	32.06	33.20	0.82	35.32	<d.l.	0.05	101.45
SR45C-8	<d.l.	29.89	33.22	0.90	37.81	<d.l.	<d.l.	101.82
SR45C-9	<d.l.	31.82	33.12	0.93	35.84	<d.l.	<d.l.	101.71
SR50-1	0.04	30.13	38.97	0.82	25.15	<d.l.	0.64	95.75
SR50-2	<d.l.	32.83	33.77	1.01	35.56	<d.l.	<d.l.	103.17
SR50-3	<d.l.	32.60	33.47	1.04	35.38	<d.l.	0.28	102.77
SR50-4	<d.l.	32.78	33.67	0.86	35.70	<d.l.	0.07	103.08
SR50-5	<d.l.	32.83	33.58	0.76	36.00	<d.l.	<d.l.	103.17
SR50-6	<d.l.	32.92	33.47	0.81	35.95	<d.l.	<d.l.	103.15
SR50-7	0.04	32.99	33.56	0.75	35.67	<d.l.	<d.l.	103.01
SR50-8	0.04	32.70	33.76	0.77	36.27	<d.l.	0.06	103.60
SR50-9	0.04	29.35	34.99	0.98	36.02	<d.l.	0.13	101.51
SR50-10	<d.l.	32.68	33.51	0.86	35.86	<d.l.	<d.l.	102.91
SR50-11	<d.l.	31.94	32.25	0.89	35.04	<d.l.	0.15	100.27
SR50-12	0.04	32.78	33.50	0.91	35.89	<d.l.	<d.l.	103.12
SR50-13	<d.l.	32.61	33.59	0.76	35.74	<d.l.	0.07	102.77
SR50-14	0.04	32.48	33.49	0.77	35.72	<d.l.	<d.l.	102.50
SR50-15	<d.l.	32.73	33.61	0.76	35.91	<d.l.	<d.l.	103.01
SR50-16	<d.l.	23.06	38.11	0.68	39.72	<d.l.	0.26	101.83
SR50-17	<d.l.	31.45	32.23	0.79	33.92	<d.l.	0.12	98.51

<d.l., below detection limit; SR, Cima Stronzi

Tab. 19 (part 1) Electron probe microanalyses (trace element analyses) on pentlandite (wt%).

	Pt	Pd	Rh	Re	Fe	Cu	Ni	S	Total
SR43-1	0.021	<d.l.	<d.l.	<d.l.	32.11	0.09	35.27	33.28	100.77
SR43-2	<d.l.	<d.l.	<d.l.	<d.l.	32.30	0.04	35.47	32.79	100.60
SR43-3	<d.l.	<d.l.	<d.l.	<d.l.	31.91	0.03	35.26	32.57	99.77
SR43-4	<d.l.	<d.l.	<d.l.	<d.l.	31.83	0.06	35.21	32.75	99.85
SR43-5	<d.l.	<d.l.	<d.l.	<d.l.	31.93	0.06	35.34	32.89	100.22
SR43-6	0.027	<d.l.	<d.l.	<d.l.	31.96	0.06	35.52	33.00	100.56
SR43-7	0.043	<d.l.	<d.l.	<d.l.	31.53	0.05	35.68	33.15	100.45
SR43-8	<d.l.	0.008	<d.l.	<d.l.	32.00	0.04	35.28	32.91	100.24
SR43-9	<d.l.	0.007	0.004	<d.l.	31.93	0.07	35.38	33.28	100.67
SR43-10	<d.l.	0.004	<d.l.	<d.l.	32.01	0.08	35.83	32.97	100.90
SR43-11	<d.l.	0.005	<d.l.	<d.l.	32.39	0.07	35.52	33.22	101.20
SR45C-1	<d.l.	0.005	<d.l.	<d.l.	31.63	0.06	36.34	32.50	100.54
SR45C-2	<d.l.	<d.l.	<d.l.	<d.l.	31.19	0.04	36.34	32.77	100.34
SR45C-3	<d.l.	<d.l.	<d.l.	<d.l.	31.83	0.05	36.16	32.60	100.64
SR45C-4	<d.l.	<d.l.	<d.l.	<d.l.	31.87	0.05	35.95	32.68	100.55
SR45C-5	<d.l.	<d.l.	<d.l.	<d.l.	31.73	0.06	36.10	32.68	100.57
SR45C-6	<d.l.	<d.l.	<d.l.	<d.l.	31.73	0.10	36.07	32.81	100.71
SR45C-7	<d.l.	<d.l.	<d.l.	<d.l.	31.86	0.11	35.69	32.84	100.50
SR45C-8	<d.l.	<d.l.	<d.l.	<d.l.	31.39	0.07	36.54	32.85	100.85
SR39-1	0.011	<d.l.	<d.l.	<d.l.	30.00	0.07	37.21	33.35	100.64
SR39-2	0.049	0.004	<d.l.	<d.l.	28.47	0.15	38.51	33.00	100.18
SR39-3	0.011	<d.l.	<d.l.	<d.l.	30.69	0.10	36.64	32.94	100.38
SR39-4	<d.l.	<d.l.	<d.l.	<d.l.	30.55	0.10	35.54	32.73	98.92
SR39-5	<d.l.	<d.l.	<d.l.	<d.l.	31.23	0.12	36.80	33.18	101.33
SR39-6	0.010	<d.l.	<d.l.	<d.l.	30.71	0.04	36.86	32.86	100.48
SR50-1	<d.l.	0.004	<d.l.	<d.l.	31.71	0.11	35.63	32.64	100.09
SR50-2	0.025	<d.l.	<d.l.	<d.l.	31.70	0.05	35.46	32.87	100.11
SR50-3	0.026	<d.l.	<d.l.	<d.l.	31.51	0.03	36.21	32.90	100.68
SR50-4	0.060	<d.l.	<d.l.	<d.l.	31.65	0.06	36.13	32.88	100.78
SR50-5	0.024	<d.l.	<d.l.	<d.l.	32.06	0.23	35.85	32.68	100.85

<d.l., below detection limit; SR, Cima Stronzi

Tab. 19 (part 2) Electron probe microanalyses (trace element analyses) on pentlandite (wt%).

	Pt	Pd	Rh	Re	Fe	Cu	Ni	S	Total
SR50-6	0.016	<d.l.	<d.l.	<d.l.	31.77	0.12	36.09	32.69	100.69
SR50-7	0.019	<d.l.	<d.l.	<d.l.	31.94	0.07	35.95	32.83	100.80
SR50-8	<d.l.	<d.l.	<d.l.	<d.l.	30.57	0.11	36.55	32.95	100.18
SR50-9	<d.l.	<d.l.	<d.l.	<d.l.	31.56	0.05	35.96	32.76	100.33
SR50-10	<d.l.	<d.l.	0.005	<d.l.	31.58	0.08	35.94	32.61	100.21
SR50-11	0.030	<d.l.	<d.l.	<d.l.	30.44	0.06	36.79	33.03	100.35
SR50-12	0.047	<d.l.	<d.l.	<d.l.	31.86	0.16	35.98	32.73	100.78
SR50-13	0.047	<d.l.	<d.l.	<d.l.	31.88	0.04	35.85	33.52	101.34
SR50-14	<d.l.	<d.l.	<d.l.	<d.l.	32.05	0.07	35.79	33.17	101.08
SR50-15	0.022	0.005	<d.l.	<d.l.	32.12	0.04	35.89	33.23	101.31
SR50-16	0.013	<d.l.	<d.l.	<d.l.	32.02	0.04	36.06	33.36	101.49
SR50-17	0.023	<d.l.	<d.l.	<d.l.	32.02	0.06	36.03	33.48	101.61
SR50-18	0.032	<d.l.	<d.l.	<d.l.	32.26	0.09	35.80	33.10	101.28
SR50-19	0.040	0.004	<d.l.	<d.l.	31.98	0.05	36.18	33.47	101.72

<d.l., below detection limit; SR, Cima Stronzi

Tab. 20 Electron probe microanalyses (base metal analyses) on pyrrhotite (wt%).

	As	Fe	S	Co	Ni	Zn	Cu	Total
SR45C-10	0.07	61.46	38.88	0.10	0.86	<d.l.	0.05	101.42
SR45C-11	0.05	61.42	39.00	0.19	1.00	<d.l.	0.09	101.75
SR45C-12	<d.l.	61.77	39.00	0.12	0.96	<d.l.	<d.l.	101.85
SR45C-13	<d.l.	61.50	39.34	0.25	0.58	<d.l.	<d.l.	101.67
SR45C-14	0.05	60.69	38.89	0.17	0.48	0.13	0.05	100.46
SR45C-15	<d.l.	59.67	37.89	0.10	0.41	<d.l.	<d.l.	98.07
SR45C-16	0.04	60.94	39.37	0.18	0.52	<d.l.	0.04	101.09
SR45C-17	0.10	62.35	38.86	0.12	0.58	<d.l.	<d.l.	102.01
SR45C-18	0.06	61.15	39.19	0.08	0.49	<d.l.	<d.l.	100.97
SR45C-19	<d.l.	61.73	39.17	0.14	0.62	<d.l.	0.05	101.71
SR45C-20	<d.l.	61.94	39.12	0.08	0.71	<d.l.	0.09	101.94
SR45C-21	0.04	61.43	39.61	0.09	0.40	<d.l.	<d.l.	101.57
SR45C-22	<d.l.	62.04	39.27	0.09	0.59	<d.l.	0.05	102.04
SR45C-23	0.04	62.01	38.84	0.07	0.76	<d.l.	0.08	101.80
SR45C-24	0.04	54.73	37.88	0.20	6.15	<d.l.	0.06	99.06
SR45C-25	<d.l.	61.02	39.31	0.08	0.50	<d.l.	0.07	100.98
SR45C-26	<d.l.	61.65	38.83	0.04	0.86	<d.l.	<d.l.	101.38
SR45C-27	<d.l.	61.58	39.52	0.16	0.40	<d.l.	<d.l.	101.66
SR45C-28	<d.l.	61.00	39.38	0.10	0.41	0.07	<d.l.	100.96
SR45C-29	<d.l.	61.60	38.87	0.11	1.11	<d.l.	0.11	101.80
SR45C-30	<d.l.	61.12	38.91	0.10	0.67	<d.l.	<d.l.	100.80
SR50-18	<d.l.	62.20	40.02	0.12	0.26	<d.l.	0.18	102.78
SR50-19	<d.l.	62.05	39.64	0.12	0.23	<d.l.	0.20	102.24
SR50-20	<d.l.	62.92	39.64	0.07	0.21	<d.l.	0.07	102.91
SR50-21	0.06	62.57	39.95	0.09	0.32	0.10	<d.l.	103.09
SR50-22	<d.l.	62.53	39.63	0.10	0.15	0.10	<d.l.	102.51
SR50-23	<d.l.	62.72	39.73	0.11	0.44	0.08	0.09	103.17

<d.l., below detection limit; SR, Cima Stronzi

Tab. 21 Electron probe microanalyses (trace element analyses) on pyrrhotite (wt%).

	Pt	Pd	Rh	Re	Fe	Cu	Ni	S	Total
SR43-12	<d.l.	<d.l.	<d.l.	<d.l.	61.21	<d.l.	0.68	38.72	100.61
SR43-13	0.017	0.007	<d.l.	<d.l.	61.23	<d.l.	0.75	37.69	99.70
SR43-14	0.015	<d.l.	<d.l.	<d.l.	61.03	<d.l.	0.67	37.78	99.50
SR43-15	<d.l.	<d.l.	<d.l.	<d.l.	61.15	0.04	0.58	38.09	99.86
SR43-16	<d.l.	0.003	0.006	<d.l.	60.88	0.04	0.61	37.81	99.35
SR43-17	<d.l.	<d.l.	<d.l.	0.020	61.86	0.02	0.69	38.15	100.74
SR45C-9	0.010	<d.l.	<d.l.	<d.l.	61.28	<d.l.	0.85	37.91	100.05
SR45C-10	<d.l.	<d.l.	<d.l.	0.020	60.94	0.05	0.53	38.59	100.13
SR45C-11	0.021	<d.l.	<d.l.	<d.l.	61.30	0.04	0.51	37.96	99.83
SR45C-12	0.023	<d.l.	0.003	<d.l.	61.31	0.08	0.46	38.37	100.24
SR50-20	0.024	<d.l.	<d.l.	<d.l.	61.63	0.02	0.55	37.96	100.18
SR50-21	0.025	<d.l.	<d.l.	<d.l.	61.60	0.03	0.39	38.30	100.34
SR50-22	<d.l.	<d.l.	0.010	0.020	61.53	0.05	0.48	37.95	100.04
SR50-23	0.029	<d.l.	0.009	<d.l.	61.14	0.02	0.68	38.34	100.22
SR50-24	0.024	0.006	<d.l.	<d.l.	60.70	0.05	0.71	38.65	100.14
SR50-25	0.023	<d.l.	<d.l.	<d.l.	61.16	0.03	0.51	39.10	100.82
SR50-26	0.040	0.009	0.008	<d.l.	61.35	<d.l.	0.39	39.02	100.82
SR50-27	0.035	<d.l.	0.004	<d.l.	60.98	0.10	0.42	39.37	100.91
SR50-28	0.037	<d.l.	<d.l.	<d.l.	61.19	0.04	0.53	39.52	101.31
SR50-29	0.032	<d.l.	<d.l.	0.010	61.68	0.02	0.38	39.44	101.56
SR50-30	0.031	0.012	<d.l.	<d.l.	61.10	0.05	0.66	39.46	101.32

<d.l., below detection limit; SR, Cima Stronzi

Tab. 22 Electron probe microanalyses (base metal analyses) on chalcopyrite (wt%).

	As	Fe	S	Co	Ni	Zn	Cu	Total
Sr45C-31	<d.l.	31.33	34.77	0.04	<d.l.	0.12	35.06	101.32
Sr45C-32	<d.l.	31.45	34.67	0.08	<d.l.	<d.l.	34.87	101.07
Sr45C-33	<d.l.	31.97	35.12	0.07	0.11	0.17	35.41	102.85
SR50-24	<d.l.	31.97	35.22	0.08	0.12	<d.l.	35.87	103.26
SR50-25	<d.l.	31.83	35.21	0.07	0.31	<d.l.	36.05	103.47
SR50-26	<d.l.	32.06	35.23	0.07	0.18	0.07	35.88	103.49
SR50-27	<d.l.	32.32	35.32	0.06	0.25	0.12	36.46	104.53
SR50-28	<d.l.	32.24	35.23	0.08	0.11	<d.l.	35.77	103.43
SR50-29	<d.l.	32.00	35.38	0.09	0.12	0.11	36.21	103.91
SR50-30	<d.l.	32.08	35.13	<d.l.	<d.l.	<d.l.	35.82	103.03
SR50-31	<d.l.	32.07	35.07	0.07	0.10	0.09	35.97	103.37

<d.l., below detection limit; SR, Cima Stronzi

Tab. 23 Electron probe microanalyses (trace element analyses) on chalcopyrite (wt%).

	Pt	Pd	Rh	Re	Fe	Cu	Ni	S	Total
SR45C-13	<d.l.	<d.l.	<d.l.	<d.l.	30.29	34.91	1.43	33.57	100.20
SR45C-14	<d.l.	<d.l.	<d.l.	<d.l.	30.92	35.82	0.03	34.52	101.29
SR45C-15	<d.l.	0.006	<d.l.	<d.l.	31.02	35.91	0.01	34.39	101.34
SR45C-16	<d.l.	0.005	<d.l.	<d.l.	48.47	16.73	0.37	36.98	102.55
SR45C-17	<d.l.	<d.l.	<d.l.	<d.l.	30.71	35.35	0.20	34.22	100.48
SR45C-18	<d.l.	<d.l.	<d.l.	<d.l.	30.73	35.86	0.07	34.60	101.26
SR39-7	<d.l.	<d.l.	<d.l.	<d.l.	30.90	36.27	0.01	34.67	101.85
SR39-8	<d.l.	0.007	<d.l.	0.010	30.97	35.46	<d.l.	34.77	101.22
SR39-9	<d.l.	<d.l.	<d.l.	<d.l.	31.03	39.18	0.08	34.87	105.16
SR39-10	<d.l.	<d.l.	<d.l.	0.020	30.54	34.99	0.69	34.96	101.20
SR39-11	<d.l.	<d.l.	<d.l.	<d.l.	31.13	34.07	<d.l.	34.83	100.03
SR50-31	<d.l.	0.005	<d.l.	0.010	31.06	35.52	0.03	34.40	101.02
SR50-32	<d.l.	<d.l.	<d.l.	<d.l.	31.16	35.72	0.13	34.49	101.50
SR50-33	<d.l.	<d.l.	<d.l.	<d.l.	31.42	34.39	0.08	35.02	100.91

<d.l., below detection limit; SR, Cima Stronzi

Tab. 24 Electron probe microanalyses (trace element analyses) on millerite (wt%).

	Pt	Pd	Rh	Re	Fe	Cu	Ni	S	Total
SR39-12	<d.l.	<d.l.	<d.l.	<d.l.	1.62	0.32	62.63	34.90	99.47
SR39-13	0.022	<d.l.	<d.l.	<d.l.	1.58	0.29	62.59	35.02	99.50
SR39-14	0.015	<d.l.	<d.l.	<d.l.	2.40	0.54	62.15	34.98	100.09
SR39-15	0.018	<d.l.	<d.l.	<d.l.	1.25	0.19	62.79	34.94	99.19
SR39-16	<d.l.	<d.l.	<d.l.	<d.l.	1.32	0.07	62.74	34.98	99.11
SR39-17	<d.l.	<d.l.	<d.l.	<d.l.	0.84	0.08	63.55	34.82	99.29
SR39-18	0.048	0.005	<d.l.	<d.l.	0.78	0.09	63.74	35.28	99.94
SR39-19	0.042	<d.l.	<d.l.	<d.l.	0.86	0.14	63.45	34.97	99.47
SR39-20	<d.l.	<d.l.	<d.l.	<d.l.	0.88	0.11	62.97	34.06	98.02
SR50-34	0.020	<d.l.	<d.l.	<d.l.	1.05	0.07	63.36	35.50	100.00

<d.l., below detection limit; SR, Cima Stronzi

18.1.3. Silicates

Tab. 25 Electron probe microanalyses on pargasite inclusions in chromites from the chromitites (wt%).

	SiO_2	TiO_2	Al_2O_3	Cr_2O_3	CaO	MgO	FeO	MnO	NiO	K_2O	Na_2O	Total
SR39-1	43.88	3.07	12.73	2.25	11.04	17.81	3.68	0.15	0.07	0.11	2.85	97.64
SR39-2	43.94	3.34	12.04	2.23	10.78	17.25	3.30	0.09	0.10	0.05	3.15	96.27
SR39-3	44.26	3.60	11.86	2.16	10.70	17.06	3.32	0.12	0.11	0.04	3.14	96.37
SR39-4	44.53	3.22	11.86	2.28	11.05	17.46	3.70	0.15	0.09	0.06	2.92	97.32
SR39-5	43.66	3.29	12.85	2.51	11.00	17.71	3.40	0.10	0.10	0.07	3.04	97.73
SR39-6	43.32	3.46	12.64	2.50	11.36	17.49	3.46	0.08	0.07	0.15	2.84	97.37
SR39-7	43.65	3.43	12.28	2.02	11.16	17.23	3.65	0.06	0.11	0.09	2.85	96.53
SR39-8	44.44	3.30	11.68	2.64	11.44	17.41	3.02	0.12	0.10	0.14	2.95	97.24
SR39-9	44.50	3.26	12.35	2.48	11.10	17.58	3.04	0.10	0.05	0.06	3.11	97.63
SR39-10	44.84	3.48	12.03	2.38	10.87	17.58	3.17	0.11	0.09	0.06	3.03	97.64
SR39-11	44.19	3.30	12.39	2.33	10.68	17.76	3.43	0.07	0.11	0.05	3.13	97.44
SR39-12	44.29	3.30	11.90	2.40	11.14	17.13	3.42	0.13	0.12	0.06	2.89	96.78
SR40A-1	43.23	3.09	12.33	2.03	11.18	18.32	3.24	0.09	0.08	0.04	3.19	96.82
SR40A-2	43.51	3.09	12.57	1.49	10.93	18.13	3.42	0.17	0.09	0.06	3.25	96.71
SR40A-3	43.25	3.73	12.43	2.10	11.47	17.85	3.18	0.04	0.07	0.07	2.81	97.00
SR40A-4	43.28	3.06	12.18	2.28	10.73	17.84	3.34	0.12	0.14	0.05	2.97	95.99
SR40A-5	43.81	2.91	12.42	2.05	10.71	17.87	3.40	0.13	0.10	0.03	3.28	96.71
SR40A-6	43.37	1.80	13.36	2.19	11.27	18.14	3.22	0.11	0.14	0.06	2.92	96.58
SR40A-7	43.85	2.70	12.36	2.17	10.97	18.06	3.49	0.10	0.10	0.04	3.08	96.92
ZN15-1	45.86	3.65	10.55	2.42	9.81	16.14	2.72	0.04	0.09	<d.l.	5.17	96.45
ZN15-2	44.69	3.39	11.24	2.57	10.29	16.55	3.17	0.06	0.12	<d.l.	4.31	96.39
ZN15-3	43.81	3.99	11.96	2.53	9.83	15.87	3.67	0.09	0.08	<d.l.	4.59	96.42
ZN15-4	43.95	4.56	11.93	2.39	9.75	15.99	3.78	0.04	0.13	<d.l.	4.62	97.14
ZN15-5	44.13	4.04	11.32	2.42	10.22	16.11	3.69	0.05	0.10	<d.l.	4.53	96.61
ZN15-6	44.99	4.35	11.77	2.41	10.08	16.38	3.08	0.05	0.08	<d.l.	4.80	97.99
ZN15-7	44.46	4.28	12.24	2.34	10.12	16.09	3.55	0.05	0.07	<d.l.	4.82	98.02
ZN15-8	45.12	4.25	12.12	2.43	9.84	16.47	3.53	0.06	0.07	<d.l.	4.16	98.05
PM23B-1	46.28	4.00	12.28	2.39	10.56	16.70	3.74	0.06	0.04	<d.l.	4.40	100.45
PM23B-2	45.43	3.89	12.08	2.60	9.40	16.69	4.24	0.10	0.06	<d.l.	4.80	99.29
PM23B-3	46.30	3.57	11.80	2.27	10.21	16.81	3.72	0.09	0.07	<d.l.	4.46	99.30

<d.l., below detection limit ; PM, Pian dellaMadonna; SR, Cima Stronzi; ZN, Ziona

Tab. 26 Electron probe microanalyses on pargasite inclusions in disseminated chromites from the serpentinized dunites (wt%).

	SiO_2	TiO_2	Al_2O_3	Cr_2O_3	CaO	MgO	FeO	MnO	NiO	K_2O	Na_2O	Total
SR32-1	45.23	2.75	10.86	2.73	10.05	18.30	3.89	0.04	0.08	<d.l.	4.33	98.26
SR32-2	44.19	3.09	11.14	2.34	10.12	18.03	3.88	0.09	0.08	<d.l.	4.11	97.07
SR32-3	45.01	2.69	11.12	2.52	10.60	17.31	3.57	0.04	0.06	<d.l.	4.39	97.31
SR32-4	44.62	3.39	11.84	2.03	10.21	17.28	3.99	0.10	0.05	<d.l.	4.62	98.13
SR32-5	43.56	3.32	12.44	2.61	11.13	16.51	4.17	0.06	0.10	<d.l.	4.19	98.09
SR32-6	44.48	3.23	11.41	2.09	10.99	17.70	3.70	<d.l.	0.04	<d.l.	4.24	97.88
SR32-7	43.77	3.34	11.62	2.30	10.38	17.45	4.03	0.13	0.05	0.04	4.14	97.25
SR32-8	43.70	2.97	11.73	2.58	9.87	17.46	4.16	0.10	<d.l.	<d.l.	4.53	97.10
SR33-1	43.44	3.71	12.33	2.52	11.25	16.21	3.99	0.06	0.07	0.03	3.87	97.48
SR33-2	43.12	3.90	12.57	2.38	10.94	16.19	3.87	0.06	0.06	0.06	3.93	97.08
SR33-3	42.94	3.95	12.67	2.60	11.09	16.19	3.90	0.04	0.05	0.04	4.04	97.51
SR33-4	43.83	3.51	12.07	2.32	10.22	16.91	4.07	0.08	0.09	<d.l.	4.44	97.54
SR33-5	43.64	3.97	12.64	2.44	11.03	16.37	3.85	0.03	0.05	<d.l.	3.95	97.97
SR33-6	43.10	3.30	12.30	2.70	11.35	16.21	3.72	0.08	0.09	0.04	3.79	96.68
SR33-7	43.01	3.41	12.48	2.84	11.34	16.21	3.83	0.04	0.06	0.03	3.87	97.12
SR33-8	43.48	3.12	12.46	2.98	11.42	16.20	3.69	0.06	0.08	0.03	3.79	97.31
SR33-9	42.90	3.64	12.77	2.64	11.11	16.24	4.04	<d.l.	0.06	0.06	4.07	97.53
SR33-10	43.58	3.51	12.38	2.54	11.09	16.59	3.71	0.08	0.04	0.04	3.99	97.55
SR33-11	43.50	4.24	12.15	2.37	10.87	16.29	3.96	0.04	0.06	<d.l.	4.19	97.67
SR34-1	43.37	3.27	12.01	2.30	11.16	16.82	3.65	0.04	0.02	0.03	3.80	96.47
SR34-2	43.56	3.20	12.98	2.40	11.06	17.55	3.50	0.07	0.07	0.04	3.57	98.00

<d.l., below detection limit; SR, Cima Stronzi

Tab. 27 Electron probe microanalyses on pyroxene inclusions in disseminated chromites from the serpentinized dunites (SR32, SR33) and chromites from the chromitites (SR39, SR40, ZN15).

	SiO_2	TiO_2	Al_2O_3	Cr_2O_3	CaO	MgO	FeO	MnO	NiO	K_2O	Na_2O	Total
SR32-1	51.44	0.73	3.99	1.43	21.84	15.05	2.66	0.05	0.02	<d.l.	1.10	98.31
SR32-2	52.84	0.40	2.85	1.25	20.67	15.84	2.97	0.12	<d.l.	<d.l.	1.46	98.40
SR33-1	53.06	0.59	3.12	1.42	21.62	15.21	2.69	0.04	<d.l.	<d.l.	1.47	99.22
SR39-1	57.81	0.24	1.46	0.75	0.23	33.39	5.88	0.17	0.08	<d.l.	<d.l.	100.01
SR39-2	57.23	0.25	2.00	0.85	0.30	32.82	6.19	0.21	0.01	<d.l.	<d.l.	99.86
SR39-3	57.41	0.27	1.46	0.88	0.22	32.83	5.97	0.14	0.03	<d.l.	<d.l.	99.21
SR39-4	57.20	0.12	1.56	1.09	0.36	33.60	5.40	0.23	0.07	<d.l.	0.02	99.65
SR39-5	57.63	0.23	1.45	0.94	0.29	33.65	5.23	0.14	0.09	<d.l.	<d.l.	99.65
SR39-6	57.55	0.24	1.71	0.97	0.24	33.88	5.36	0.17	0.08	<d.l.	0.02	100.22
SR40A-1	56.19	0.29	1.94	1.04	0.36	34.55	5.82	0.15	0.09	<d.l.	0.02	100.45
SR40A-2	56.00	0.18	2.11	1.09	0.33	34.50	5.68	0.16	0.10	<d.l.	0.01	100.16
SR40A-3	55.84	0.36	2.42	1.09	0.29	34.10	5.61	0.17	0.03	<d.l.	<d.l.	99.91
ZN15-1	57.95	0.04	0.70	0.80	0.32	33.45	5.09	0.16	0.04	<d.l.	0.02	98.57
ZN15-2	57.96	0.23	1.12	0.76	0.44	32.97	5.26	0.17	0.02	<d.l.	0.04	98.97
ZN15-3	57.69	0.23	1.28	0.75	0.57	32.62	5.43	0.18	0.09	<d.l.	0.03	98.87
ZN15-4	57.57	0.24	1.39	0.64	0.39	32.88	5.28	0.15	0.08	<d.l.	0.03	98.65
ZN15-5	59.18	0.26	0.95	0.55	0.39	33.81	5.39	0.20	0.10	<d.l.	0.05	100.88
ZN15-6	58.89	0.16	1.15	0.63	0.46	33.98	5.52	0.16	0.08	<d.l.	0.03	101.06
ZN15-7	58.78	0.24	0.91	0.77	0.34	34.15	5.02	0.17	0.08	<d.l.	0.04	100.50

<d.l., below detection limit; SR, Cima Stronzi; ZN, Ziona

Tab. 28 Electron probe microanalyses on olivine inclusions in disseminated chromites from the serpentinized dunites (wt%).

	SiO_2	TiO_2	Al_2O_3	Cr_2O_3	CaO	MgO	FeO	MnO	NiO	K_2O	Na_2O	Total
SR32-1	41.91	0.07	0.04	0.52	0.07	50.09	8.25	0.10	0.30	<d.l.	<d.l.	101.35
SR32-2	41.34	0.02	0.04	0.54	0.06	50.42	8.13	0.19	0.27	<d.l.	0.05	101.06
SR32-3	41.40	0.04	0.05	0.71	0.06	50.24	8.08	0.17	0.28	<d.l.	<d.l.	101.03
SR32-4	41.08	0.04	<d.l.	0.51	0.05	49.70	8.55	0.19	0.32	<d.l.	<d.l.	100.44
SR33-1	41.70	0.08	<d.l.	0.98	0.04	51.09	7.35	0.21	0.30	<d.l.	<d.l.	101.75

<d.l., below detection limit; SR, Cima Stronzi

Tab. 29 Electron probe microanalyses on olivine from the melatroctolites (wt%).

	SiO_2	TiO_2	Al_2O_3	Cr_2O_3	CaO	MgO	FeO	MnO	NiO	K_2O	Na_2O	Total
MT28B-1	40.97	<d.l.	<d.l.	<d.l.	0.06	47.39	12.50	0.22	0.30	<d.l.	<d.l.	101.44
MT28B-2	40.71	0.05	<d.l.	<d.l.	0.03	47.85	12.09	0.19	0.30	<d.l.	0.01	101.23
MT28B-3	41.23	0.05	<d.l.	<d.l.	0.03	48.43	12.09	0.25	0.24	<d.l.	<d.l.	102.32
MT28B-4	41.16	0.11	<d.l.	<d.l.	0.03	47.51	11.85	0.22	0.28	<d.l.	0.02	101.18
MT28B-5	40.82	0.04	<d.l.	<d.l.	0.04	47.90	11.45	0.20	0.24	<d.l.	0.01	100.70
MT28B-6	41.25	0.00	<d.l.	0.06	0.05	47.24	12.22	0.20	0.28	<d.l.	<d.l.	101.30
MT28B-7	41.28	0.14	<d.l.	<d.l.	0.05	47.61	12.21	0.21	0.31	<d.l.	0.01	101.82
MT28B-8	41.14	0.12	<d.l.	0.03	0.07	47.54	12.06	0.19	0.27	<d.l.	<d.l.	101.42
MT28B-9	41.24	0.11	<d.l.	<d.l.	0.05	47.79	12.09	0.21	0.29	<d.l.	<d.l.	101.78
MT28B-10	41.00	0.05	<d.l.	<d.l.	0.05	47.61	12.12	0.25	0.30	<d.l.	<d.l.	101.38
MT28B-11	41.11	<d.l.	<d.l.	0.03	<d.l.	47.46	11.90	0.20	0.29	<d.l.	<d.l.	100.99
MT28B-12	41.05	0.03	<d.l.	<d.l.	0.03	47.94	11.96	0.20	0.29	<d.l.	0.01	101.51
MT28B-13	40.89	0.14	<d.l.	<d.l.	0.04	48.02	12.09	0.21	0.25	<d.l.	<d.l.	101.64
MT28B-14	41.06	0.04	<d.l.	<d.l.	0.04	47.71	12.03	0.16	0.22	<d.l.	<d.l.	101.26
MT28B-15	41.29	<d.l.	<d.l.	<d.l.	0.03	48.02	11.80	0.22	0.22	<d.l.	<d.l.	101.58
MT28B-16	40.77	<d.l.	<d.l.	0.09	0.04	48.00	11.99	0.16	0.33	<d.l.	<d.l.	101.38
MT28B-17	40.89	0.09	<d.l.	<d.l.	0.06	47.76	12.09	0.19	0.31	<d.l.	0.01	101.40
MT28B-18	40.63	<d.l.	<d.l.	0.04	0.04	47.74	12.16	0.19	0.30	<d.l.	<d.l.	101.10
MT28B-19	41.20	<d.l.	<d.l.	0.10	0.04	47.87	12.42	0.20	0.31	<d.l.	<d.l.	102.14
MT28B-20	41.11	0.11	<d.l.	<d.l.	0.04	47.59	11.84	0.15	0.34	<d.l.	0.02	101.20
MT28B-21	41.10	0.15	<d.l.	<d.l.	<d.l.	48.20	11.91	0.18	0.31	<d.l.	<d.l.	101.85

<d.l., below detection limit; MT, Mattarana

Tab. 30 Electron probe microanalyses on poikilitic clinopyroxene from the melatroctolites (wt%).

	SiO_2	TiO_2	Al_2O_3	Cr_2O_3	CaO	MgO	FeO	MnO	NiO	K_2O	Na_2O	Total
MT28B-1	58.245	<d.l.	0.25	<d.l.	13.72	21.21	5.42	0.11	0.07	<d.l.	0.03	99.03
MT28B-2	58.357	<d.l.	0.19	0.12	13.32	21.59	4.79	0.09	0.04	<d.l.	0.03	98.56
MT28B-3	58.752	<d.l.	0.09	<d.l.	13.15	21.69	4.69	0.09	0.04	<d.l.	<d.l.	98.49
MT28B-4	53.771	0.454	2.295	0.025	22.784	16.963	3.261	0.101	0.036	<d.l.	0.412	100.109
MT28B-5	53.016	0.611	2.602	0.095	22.728	16.837	3.319	0.1	0.034	<d.l.	0.489	99.831
MT28B-6	52.24	0.841	3.749	0.116	20.964	16.232	3.261	0.107	0.065	<d.l.	0.647	98.223
MT28B-7	51.98	0.945	3.854	<d.l.	22.199	15.62	3.233	0.139	<d.l.	<d.l.	0.613	98.589
MT28B-8	51.886	0.639	4.094	0.083	21.682	16.065	3.469	0.108	0.056	<d.l.	0.601	98.683
MT28B-9	58.107	<d.l.	0.293	0.025	13.037	21.688	3.948	0.053	0.058	<d.l.	<d.l.	97.211
MT28B-10	57.174	0.147	0.166	<d.l.	12.957	20.272	5.718	0.135	<d.l.	<d.l.	0.027	96.613
MT28B-11	57.696	0.037	0.396	<d.l.	12.613	22.503	4.839	0.08	<d.l.	<d.l.	0.029	98.206
MT28B-12	44.021	2.919	12.408	<d.l.	12.015	17.477	5.284	0.059	0.092	0.153	2.919	97.347
MT28B-13	44.464	2.988	12.301	0.037	11.636	17.066	5.149	0.052	0.107	0.129	3.002	96.931
MT28B-14	43.949	3.152	12.305	0.049	11.463	17.097	5.418	0.074	0.061	0.134	2.95	96.652
MT28B-15	55.345	0.037	0.116	<d.l.	25.512	16.179	3.938	0.149	0.037	<d.l.	0.037	101.371
MT28B-16	54.604	<d.l.	0.237	<d.l.	23.82	16.555	3.924	0.169	0.021	<d.l.	0.03	99.381
MT28B-17	53.684	0.473	2.777	<d.l.	22.471	16.57	3.138	0.128	0.019	<d.l.	0.536	99.796
MT28B-18	58.207	0.092	0.469	0.07	12.326	21.891	5.222	0.118	0.044	<d.l.	0.022	98.475
MT28B-19	59.18	<d.l.	0.081	<d.l.	12.852	21.836	4.582	0.064	<d.l.	<d.l.	0.014	98.614
MT28B-20	58.17	0.046	0.228	<d.l.	12.478	21.551	5.056	0.088	<d.l.	<d.l.	0.093	97.719
MT28B-21	55.114	0.121	0.218	<d.l.	24.512	16.493	4.017	0.185	0.019	<d.l.	0.035	100.714
MT28B-22	58.271	0.046	0.177	0.045	12.997	20.104	6.438	0.123	0.032	<d.l.	0.05	98.289
MT28B-23	53.908	0.732	2.6	0.037	20.923	16.438	3.308	0.112	0.013	<d.l.	0.463	98.538
MT28B-24	55.083	0.093	0.211	<d.l.	23.349	16.913	3.425	0.165	<d.l.	<d.l.	0.028	99.276
MT28B-25	57.8	<d.l.	0.218	<d.l.	12.697	20.438	6.237	0.124	0.01	<d.l.	0.046	97.597

<d.l., below detection limit; MT, Mattarana